Spring 2020

Design of Bio-Inspired Multifrequency Acoustic Sensors and Metamaterial Energy Harvesting Smart Structures

Mohammadsadegh Saadatzi

Design of Bio-inspired Multifrequency Acoustic Sensors and Metamaterial Energy Harvesting Smart Structures

by

Mohammadsadegh Saadatzi

Bachelor of Mechanical Engineering
Multimedia University, Malaysia, 2014

Master of Electrical Engineering
Multimedia University, Malaysia, 2016

Submitted in Partial Fulfillment of the Requirements

For the Degree of Doctor of Philosophy in

Mechanical Engineering

College of Engineering and Computing

University of South Carolina

2020

Accepted by:

Sourav Banerjee, Major Professor

Lingyu Yu, Committee Member

Juan Caicedo, Committee Member

Tanvir Farouk, Committee Member

Austin Downey, Committee Member

Cheryl L. Addy, Vice Provost and Dean of the Graduate School

DEDICATION

This dissertation is dedicated to my family especially to my parents Mr. Mohammadali Saadatzi and Mrs. Zahra Dalaie Esfahani.

Also, I would like to dedicate this work to my bachelor's degree advisor, Prof. Venkataseshaiah Chinthakunta and my master's degree advisor, Prof. Ajay Kumar Singh.

Last but definitely not the least, I would like to dedicate my work to my dear PhD advisor, Dr. Sourav Banerjee for all his enormous supports and guidance in the past five years.

ACKNOWLEDGEMENTS

I would like to thank my honorable advisor Dr. Sourav Banerjee for his cordial support and invaluable guidance and mentorship in my PhD studies. I am one of the blessed students who got this opportunity to work with knowledge person like him. I also would like to thank all the previous and existing iMAPS members for their continuous support. I would like to thank Prof. Juan Caicedo, Prof. Austin Downey, Prof. Lingyu Yu and, Prof. Tanvir Farouk for being part of my Dissertation Committee and for careful review of this work.

Financial support from NASA Langley Research Center, Department of Mechanical Engineering and Graduate School at the University of South Carolina are gratefully acknowledged.

Finally, I am very grateful to my both brothers, Dr. Mohammad Nasser Saadatzi and Dr. Mohammad Hossein Saadatzi with University of Louisville, KY, USA, for all their sacrifice and selfless support throughout their existence in my life.

ABSTRACT

Due to the limited availability and high depletion rates of nonrenewable sources of energy as well as environmental concerns, the scientific community has started to explore many alternative clean sources of energies. It is identified that civil, mechanical and Aerospace structures are always subjected to acoustic noises and vibration which could potentially be used as renewable source of energy. Roads and Industrial noise barriers are used inside industrial facilities alongside the walls, around construction pillars, nearby machinery and other equipment to separate quite work zones, protect walls, deliver extra safety and precautions while diminish sound and vibrational pressure. We hypothesized if these noise barriers/structures could serve dual purposes, while harvest energies from the filtered noises and vibrations, significant energies could be renewed. Such renewable energies could be then used for different purposes, like charging cell phones, wearable devices, powering small electronics and remote sensors etc. Additionally, due to gravity, it is natural that our heavy mechanical equipment runs, operates, walks on the ground which are covered by cosmetic materials. Such materials encounter continuously changing pressure on the surface which is otherwise waisted if not harvested. Keeping these applications in mind for walls/ barriers/ tiles, oin this dissertation, utilizing one unique physics, two different type of renewable energy harvesting technologies are proposed. While proposing the application of harvesting and noise filtering, similar physics/mechanics prevalent in cochlea of human inner ear, further motivated this

dissertation to device bio-inspired acoustic bandpass sensor. The harvesting and sensing devices that are conceptualized, analytically modeled, numerically simulated via COMSOL Multiphysics software, optimized, fabricated and tested to present the proof of concept are presented below. All models are numerically

1) A novel three-dimensional piezoelectric energy harvester based on a metamaterial structure is proposed, which is capable of scavenging energy at very low frequencies (<~1kHz) from multi-axial ambient vibrations. The proposed structure and its unit cell exploit the negative mass at local resonance frequencies and entraps the vibration energy as dynamic strain. The captured kinetic energy is then transformed to electric potential using three Lead Zirconate Titanate wafers, optimally embedded in the cell's soft constituent.
2) In the second design, a multi-frequency vibration-based energy harvester unit cell which is inspired from the design of human inner-ear, i.e. a snail-shaped model to enhance differential shear deformation of a membrane is proposed. Next an array of the proposed cell in the form of metamaterial bricks in a wall or a metamaterial tiles on the ground (Meta-tile) are modeled and fabricated to experimentally validated the concept. A spiral snail shaped PVDF membrane is embedded inside a Polydimethylsiloxane (PDMS) matrix that entraps the kinetic energy of the vibration within its structure. Numerical and experimental studies show that the unit cell and the Meta-tiles can harvest electrical power of up to ~1.8 mW and 11 mW against a 10KΩ resistive load, respectively.
3) Concurrent to the development of electronic processing of frequencies, mechanical sensors capable of selecting, processing, filtering specific single or a distinct band of

frequencies are contributing an essential role in many sciences, technologies and industrial applications. After developing the energy harvester devices, the next objective of this PhD dissertation is to present a scalable numerical model along with a fabricated proof of concept of a bio-inspired acoustic bandpass sensor with a user-defined range of frequencies. In the proposed sensor, the geometric structure of a human's basilar membrane is adopted as the main model to capture the sonic waves with a target frequency ranges. Human's basilar membrane in the inner ear could be investigated in two ways, a) plate type and b) beam type. Both models are numerically and experimentally validated. In the first step, a predictive mathematical model of the proposed bandpass sensor is developed based on a plate type model. Next, the dynamic behavior of beam-type basilar membrane with 100 Zinc-Oxide electrodes is modeled and numerically verified. A sensor array is fabricated with using photolithography techniques with Polyvinylidene Difluoride (PVDF) piezoelectric material as a proof-of-concept. The fabricated plate-type sensor is experimentally tested, and its effective performance is validated in the frequency range of ~3 kHz-8 kHz. Similarly, in beam model the longest electrode is near the Apex region (8 mm x 300 μm x 20 μm thick) and the shortest electrode is near the Base side of the sensor with (3 mm x 300 μm x 110 μm thick) are proposed. Eventually, the effective performances of the proposed acoustic sensors are verified using COMSOL Multiphysics Software and the functionality of the proposed sensor appeared in the frequency range of ~ 0.5 kHz near Apex and to ~ 20 kHz near base side.

To run all the required experiments on the fabricated energy harvesters and acoustic sensors in this dissertation, a novel three-dimensional exciter is developed as a

miscellaneous work. A high percentage of failures in sensors and devices employed in harsh industrial environments and airborne electronics is due to mechanical vibrations and shocks. Therefore, it is important to test the equipment reliability and ensure its survival in long missions in the presence of physical fluctuations. Traditional vibration testbeds employ unidirectional acoustic or mechanical excitations. However, in reality, equipment may encounter uncoupled (unidirectional) and/or coupled (multidirectional) loading conditions during operation. Hence, to systematically characterize and fully understand the proposed energy harvesters' and acoustic sensors' behaviors, a testbed capable of simulating a wide variety of vibration conditions is required which is designed, and fabricated. The developed testbed is an acousto electrodynamic three-dimensional (3-D) vibration exciter (AEVE 3-D), which simulates coupled and decoupled (with unpowered arms) 3-D acoustic and/or 3-D mechanical vibration environments. AEVE 3-D consists of three electromagnetic shakers (for mechanical excitation) and three loudspeakers (for acoustic excitation) as well as a main control unit that accurately calculates and sets the actuators' input signals in order to generate optimal coupled and decoupled vibrations at desired frequencies. In this paper, the system's architecture, its mechanical structure, and electrical components are described. In addition, to verify AEVE 3-D's performance, various experiments are carried out using a 3-D piezoelectric energy harvester and a custom-made piezoelectric beam.

TABLE OF CONTENTS

LIST OF TABLES

LIST OF FIGURES

LIST OF SYMBOLS

E	Stiffness
ρ	Density
ν	Poisson Ratio
L	Length
B_i	Base Width
B_f	Apex Width
h	Thickness

LIST OF ABBREVIATIONS

FEM ..... Finite Element Method

PnC..... Phononic Crystals

CHAPTER 1

INTRODUCTION

1.1 Problem Statement

In the last few decades, the band pass sensors and the single frequency (resonance) sensors are progressively utilized in numerous applications of science engineering and technology. For example, such sensors are used in the micro mechanical devices, manufacturing instrumentation, 3D printing, micro-electronics devices, photonics and phononic devices and overall in many chemical and biological applications. Frequency sensors are highly demanded in the above-mentioned applications with the rapid advancement of the technologies that leads to the complex measurements / operations with the high level of accuracy. Our consumer driven market demands these sophisticated devices with the highest standards of quality but with uncompromised reliability.

The in-process sensors play significant role in assisting the industrial systems producing the near accurate outputs. In-process sensors are used to generate control signals to improve both the control and the productivity of the engineering systems. For example, acoustic emission (AE) sensors are used in many precision metals cutting processes to monitor the degree of tool wear, chip formation, surface features, etc., and in precision grinding, acoustic emission sensors are used to detect both the near approach of the grinding wheel to the work surface, and the initial wheel contact with the work. In particular, in-process sensors are needed in engineering systems, because human oversight

of the industrial process is inadequate to achieve the necessary level of performance. Traditionally, electronic and mechanical sensors are widely employed in industrial applications. Mechanical sensor covers a large area of the sensor technology due to its wide compatibility in many engineering domains. However, mechanical sensors are typically limited for high frequency applications due to its design constraints. Resonance phenomenon is the key in mechanical sensors to select a specific frequency. Because of its operating principle, large geometry is essential to employ the traditional mechanical sensors for low frequency applications. Hence, a novel but universal frequency selection process is necessary which can be adopted for sensing almost any wide range of frequencies with controlled geometric configurations.

1.2 **Background**

Acoustic sensors can be classified into two categories of (i) distinct single frequency sensors, where a unique frequency is of interest and the sensors are devised to only respond to acoustic stimuli with that single frequency, and (ii) bandpass sensors, where a desired frequency band is sensed and the rest of the frequencies are filtered out [1, 2]. A band is defined as the range of frequency where the energy transmission coefficient is very low and almost no energy can pass through the structure [3-5]. Resonance phenomenon is the key point in acoustic sensors to select a specific frequency [6-9]. Due to the resonance principle, large-scale geometries are required for fabrication of acoustic sensors in low-frequency applications. Cantilever beam (CB) model is the most popular approach in designing such sensors. Exploring the resonance frequencies, it is possible to select a unique frequency from a specific beam. These types of sensors monitor and detect the resonance frequency shift in order to facilitate the analysis of the target parameters [2-8].

Battiston et al. [9, 10] presented a chemical sensor based on an array of eight silicon cantilever beams. All cantilevers are glazed on one side with a sensor coat that displays a distinct response to the target analyte molecules. Because of the change in surface stress or the beam mass the cantilevers mechanically respond to the bending of the beams, when the sensor layer is exposed to the analyte. Similar class of bio-chemical sensors are also presented by Moulin et al. [7] that can absorb bio-chemical species on the functionalized surface of a microfabricated cantilever and cause surface stress. Biosensors have attracted substantial attention in the last few years since the monitoring of a specific matter/molecules are crucial aspect in many applications ranging from the clinical analysis to the environmental control and to the monitoring of numerous industrial processes [6, 11-13]. Zhu et al. [14] proposed a piezoelectric microcantilever sensor for detection of humidity through resonance frequency shift due to the change in the young's modulus of the cantilever beams. Hodnett et al. [15] describes a broadband acoustic sensor to evaluate the acoustic emissions from the cavitation produced by a typical commercial 20 kHz sonochemical horn processor.

Traditionally, researchers utilize conventional materials for detecting acoustic waves. However, these materials do not possess the ability to respond to acoustic vibrations across a wide range of frequencies. Thus, to address this incapability, application of metamaterials has been proposed. Metamaterials are artificial materials engineered to have properties that have not yet been found in nature [10]. They are assemblies of multiple individual elements produced from conventional materials, such as metals or plastics, which are typically constructed into repeating patterns [10-12]. It is well-established that in any acoustic metamaterial structure, frequency band gaps are the results of either local resonance or

Bragg scattering [13, 14]. Low-frequency sonic waves can be controlled by introducing locally resonant components into a unit metamaterial (known as sonic crystal) [15, 16], whereas conventionally high frequency stop bands can be formed by multiple scattering (Bragg) of the periodic inclusion of the sonic crystals [14, 17, 18]. Acoustic metamaterials offer a number of exceptional properties (e.g., negative bulk modulus, negative effective mass density) that are not achievable using natural materials.

Nature is the best source of ultimate scientific references. Hence, to advance the existing state-of-the-art knowledge, researchers are not only digging hard in their associated areas, but also taking inspiration from natural phenomena. A recent seminal study demonstrated that the human cochlea performs a bandpass filtration functionality where it senses only a specific frequency band (20 Hz to 20 KHz) and mechanically filters out all other frequencies. Cochlea implants and hearing aids substantially improve quality of life and wellbeing of individuals with hearing impairments. Currently, more than 10% of the general population and 35% of people over 65 find it difficult to work and perform activities of daily living (ADL) without some sort of a hearing aid [19, 20]. Hearing impairment, if untreated, negatively influences one's quality of life and income immensely. The human ear picks up sound waves and converts them into information interpretable by the brain. Sound waves first enter the ear and are directed through the ear canal where they first reach the ear drum. As the ear drum begins to vibrate, it sets the ossicular chain in an oscillating motion, which is received in the inner ear. Within the inner ear, the cochlea receives the mechanical vibrations and converts them into electrical signals, which are then passed onto the brain. Within the cochlea is the basilar membrane (BM), which is a stiff structural element that separates two liquid-filled tubes that run along the cochlear coil.

When unrolled, the BM has a trapezoidal geometry, which is the narrowest and stiffest toward the basal end (close to the oval window) and grows widest and least stiff close to the apical end. Hence, the BM features a high eigenfrequency near the basal end, and a low eigenfrequency in the vicinity of the apical end. Upon receiving an acoustic signal with a given frequency, the fluid in the cochlea is set in motion, causing a vibration along the BM at a particular location matching that acoustic frequency. This local vibration causes tension differences in the ear sensory cells (i.e., hair cells) which produce bioelectrical signals that are passed along the auditory nerves to the brain. This unique structure with gradually varying stiffness furnishes a frequency separation mechanism of acoustic input signals as the local resonance dominates at different places of the BM [21]. In other words, each acoustic signal frequency matches the eigenfrequency of a certain spot along the BM and generates a large biosignal due to the local resonance. Therefore, the brain perceives audible signals after they are decomposed into many narrow sub-bands of gradually shifting frequencies. Artificial cochlea is an implantable neural prosthesis that can restore hearing perception in individuals with severe damage in their inner ear (particularly, hair cells) by directly transmitting sound stimuli to the auditory nerves via their electrical stimulation [22]. Artificial cochleae include artificial basilar membranes (ABM) that are typically arrays of microcantilevers fabricated via application of MEMS technology on high Young's modulus materials [23, 24]. These microcantilever arrays are comb-shaped digitated structures with an ensemble of "fingers" with gradually varied length, arranged at uniform intervals and hanging from a rigid support. Due to their varied length, each of these fingers has a unique eigenfrequency (i.e., resonance) and, hence, is tuned to a particular audible tone. These fingers have a common support, but are otherwise

mechanically isolated, with air- or fluid-filled gaps. For instance, Tanaka and colleagues [25] developed an ABM via a resonator array of thin silicon digitated fingers fashioned as a fishbone structure. In their proposed structure, the spatial frequency selection was realized by gradual variation of the fingers' length along the resonator array. Xu and colleagues [26] proposed an auditory front-end processing unit that realized the spatial frequency selectivity of a BM using a polymeric microcantilever resonance array. Their proposed structure employed an array of transparent microcantilevers with variable stiffness, which functioned as optical waveguides to direct a light beam emitted from an LED to a photo diode. Battiston and colleagues [27] microfabricated a BM-inspired chemical sensor using a resonator array of eight thin silicon microcantilever beams. They glazed the individual microcantilevers with a chemo-marker that responded when exposed to an analyte molecule layer upon bending and vibration. Similarly, Moulin and colleagues [28] microfabricated a class of bio-chemical sensors using microcantilever arrays. Finally, imitating a BM structure, Shahruz [29, 30] developed an energy harvester based on an array of varied-length piezoelectric microcantilevers with a small mass at their tip, to scavenge energy from ambient vibrations with a wide range of oscillation frequencies.

Although microcantilever-based ABMs with such a disjoint comb-shaped structure are popular and can realize frequency separation, an acceptable frequency selectivity and decomposition in the entire audible frequency range necessitates a large number of microcantilevers to be arranged in a constrained space (i.e., 35-40 mm human cochlea size). This not only complicates the fabrication process considerably, but also brings about a rather fragile array structure with insufficient mechanical strength and, hence, less-than-ideal lifetime (typically less than 20 years), requiring explanation and re-implantation in

many recipients of cochlea implants. Furthermore, the discrete nature of this comb-like structure tends to overlook the frequencies in between two adjacent microcantilevers tuned for specific tones. Microcantilever-based ABMs neglect the longitudinal coupling and continuous nature of the biological BM. To address the aforementioned drawbacks, in this dissertation, we propose an ABM structure with a piezoelectric continuum, inspired by the tapered geometry of the human BM, along with a special electrode design and integration that mimic the functionality of sensory cells in human cochlea. The continuous geometry of the proposed structure enables the proposed ABM to function as a linear transmission line with a traveling-wave behavior, as opposed to a disjoint array of discrete microcantilevers. This ABM continuum which is made out of a piezoelectric material vibrates due to acoustic excitations and generates electric potential. The proposed ABM furnishes a graded stiffness along its longitudinal structure via a tapered geometry and varying mechanical boundary conditions, but continuously homogenous mechanical properties. Such graded stiffness of this piezoelectric continuum along with the special electrode distribution enable superior spatial frequency selectivity of acoustic waves along a wide frequency range across the ABM structure based on the physics of local resonance. As the resonating spot on the piezoelectric continuum vibrates with a relatively large magnitude, the generated voltage corresponding to that location is much larger than neighboring locations, thereby realizing a spatial frequency separation and mapping.

1.3 **Objectives**

Cantilever beam-based frequency sensors use the resonance phenomenon to select a target frequency. Operating principle of cantilever beam limits these sensors to only high frequency applications due to their humungous size to achieve the resonance behavior at

the lower frequencies. Hence a universal approach is essential to select the low frequencies, mechanically. In this work, we intend to introduce an innovative frequency selection mechanism that can be employed at the both low and high frequency applications. After rigorous study, it has been found that, in nature, the human cochlea performs similar operation where it senses only a specific range of frequency (20 Hz to 20 KHz) and filters all the other frequencies, mechanically. Basilar membrane is the key component in the cochlea in selecting and filtering acoustic frequencies using the varying stiffness of the membrane from base to apex end [16]. The basilar membrane is stiff and narrow (about 100 μm) near the base, and flexible and wide (about 500 μm) near the apex, with a smooth logarithmic transition along its length. During operation as a broadband / band pass sensor, human cochlea performs four major operations (a) it create local resonances; (b) it captures only the chosen frequencies and remain unresponsive to the other frequencies; (c) it senses the input frequencies with a sensory medium (called hair cells); and in turn (d) it spatially selects the frequencies. Note that, human cochlea uses the local resonance phenomenon, which allows the ~35 mm long cochlea to select very low frequencies (< ~3 KHz) which is impossible using the cantilever beam design. In this research, we aimed to propose a universal bio-inspired mechanical band pass sensing technique, mimicking the functionalities of the human cochlea that can be employed for selecting both the low and the high frequencies.

1.4 **Outline**

Main goal of this dissertation is to present the multi-scale computational, numerical and experimental model for the bio-inspired acousto-ultrasonic band pass sensor that are capable of mechanically sense and/or filter wide range user defined frequencies. The

proposed method not only overwhelms the inabilities of the respective state-of-the-art, but also suggests its few novel applications. This dissertation is organized in such a way that it can deliver both the importance and the capabilities of the proposed band pass mechanism. The organization of the study is given below:

Chapter 1: Describes the target and the necessities of this work.

Chapter 2: This chapter describes the corresponding background and the state-of-the-art technologies. Acoustic sensors and their application in energy harvesting technologies.

Chapter 3: This chapter describes a novel piezoelectric energy harvester based on a metamaterial structure, which is capable of scavenging energy from low-frequency, multi-axial ambient vibrations.

Chapter 4: This chapter describes a novel High voltage piezoelectric energy harvester based on a metamaterial structure, which is capable of scavenging energy from multiple low-frequency ambient vibrations.

Chapter 5: This chapter proposes a piezoelectric continuum features an isosceles trapezoidal geometry which is situated atop an elastomer matrix with embedded electrode grooves and a duct. At first, a detailed analytical model is presented, which formulates the continuum's planar deflection equation, governing its elastodynamic behavior.

Chapter 6: This chapter describes the design, fabrication, and testing of an acousto electrodynamic three-dimensional (3-D) vibration exciter (AEVE 3-D), which simulates coupled and decoupled (with unpowered arms) 3-D acoustic and/or 3-D mechanical vibration environments.

CHAPTER 2:

LITERATURE REVIEW

2.1 Abstract

This chapter is to categorically review and compare the state-of-the-art vibration-based energy harvesting approaches. To evaluate the contemporary methodologies with respect to their physics, average power output and operational frequencies, systematically divided and easily readable tables are presented followed by the description of the energy harvesting methods. Energy harvesting is the process of obtaining electrical energy from the surrounding vibratory mechanical systems through an energy conversion method using smart structures, like, piezoelectric, electrostatic materials. Recent advancements in low power electronic gadgets, micro electromechanical systems, and wireless sensors have significantly increased local power demand. In order to circumvent the energy demand; to allow limitless power supply, and to avoid chemical waste from conventional batteries, low power local energy harvesters are proposed for harvesting energy from different ambient energy sources. Piezoelectric materials have received tremendous interest in energy harvesting technology due to its unique ability to capitalize the ambient vibrations to generate electric potential. Their crystalline configuration allows the material to convert mechanical strain energy into electrical potential, and vice versa. This chapter discusses the various approaches in vibration-based energy scavenging where piezoelectric materials are employed as the energy conversion medium.

2.2 Introduction

Rapid growth in low power electronic devices, micro electromechanical systems, and wireless sensors have significantly increased the power demand in our present digital economy. The increased use of cell phones, iPods, tablets, and iPads throughout the world have resulted in a surprisingly large energy footprint. According to the 'International Energy Agency', household energy demand has increased by 3.4% since 1990 [31]. It is calculated that in the US alone, the usage of the smart phones alone demands 1269 000 Million Watthour of energy per year [32]. If these power demands could be satisfied by local powering devices (for instance through harvesting the energy from abundant ambient vibrations), power demands could be significantly relieved. Energy harvesters utilize the ability of smart materials (e.g. piezoelectric, electrostatic) to generate electric potential in response to the external mechanical deformation [33-36]. Additionally, the lifespans of the embedded batteries are limited and shorter compared to the operational life of the host electronic devices. In many occasions, there placements or recharging of the batteries are unproductive and at times impossible. Battery replacements or recharging the portable electronics can be tedious, since the batteries can die without any indication. In this digital world, the wireless sensors are employed in very remote and complex territories; for example, sensors on the civil structures (e.g. bridge/building/aircraft) for structural health monitoring, or the use of global positioning system tracking devices in the forests. At instances where the battery is fully dead, it can be very expensive to replace the battery. In certain cases, sensors are integrated within a device or embedded inside the structures, e.g. civil infrastructure, making it almost impossible to replace the batteries. An energy harvesting device can be a utilitarian alternative to the batteries. There are many areas

where the harvester can generate continuous power from the ambient or the structural vibration. Overall, the key motivation of the energy harvesting research is to introduce the self-powered wireless electronic systems in order to alleviate the extended power demand and eliminate the maintenance, replacement, and the chemical waste from the old batteries [37]. Energy harvesting technology is principally driven by the deformation of the host structure due to the mechanical or the acoustic vibrations. Typically, smart structures are embedded in the host structure to convert the strain energy of the host structure, due to the deformation, into the electrical potential. The converted electrical energy can either be used to power the electronic devices directly or to store the energy into a battery/capacitor for later use on demand. Various types of smart materials, like, piezoelectrics, piezoresistives, and magnetostrictives are often used in the vibration-based energy harvesting devices. However, this chapter focuses on piezoelectric energy harvesting approaches. Piezoelectric materials can be of three forms: ceramic type, polymeric type or composite type [38, 39]. The piezoelectric material exhibits two types of piezoelectric effect: direct and converse. The direct piezoelectric effect defines the piezoelectric material's capacity to transform the mechanical strain into the electrical energy while the converse effect describes the capacity to transform the applied electrical potential into the mechanical strain energy. The direct piezoelectric effect is responsible for the material's ability to function as a sensor and the converse piezoelectric effect is accountable for its ability to function as an actuator. Thus, the piezoelectric material can be employed both as a sensor (using direct piezoelectric effect) and an actuator (using converse piezoelectric effect). The coupled electromechanical behavior of the piezoelectric materials can be represented by two constitutive equations, as follows.

Direct piezoelectric effect:

$$D_i = e_{ij}^{\sigma} E_j + d_{im}^{d} \sigma_m$$

Converse piezoelectric effect:

$$\varepsilon_k = d_{jk}^{c} E_j + S_{km}^{E} \sigma_m$$

where D_i represents the dielectric displacement in N mV^{-1} or Cm^{-2}, ε_k is the strain vector, E_j is the applied electric field vector in Vm^{-1}, and σ_m is the stress vector in m^{-2}. d_{im}^{d} and d_{jk}^{c} are the piezoelectric coefficients in m V^{-1} or CN^{-1}, e_{ij}^{σ} is the dielectric permittivity in NV^{-2} or Fm^{-1}, and S_{km}^{E} is the elastic compliance matrix in m^2N^{-1}.

In recent years, numerous papers have reviewed the vibration-based energy harvesting technology with different means. Kim et al [40] discussed various vibrational energy harvesting devices, discussing the energy conversion mediums and the respective mathematical models. Sodano et al [34] reviewed various aspects (e.g. source vibration, device efficiency, power storage, circuitry and the damping effects) of conventional energy harvesting models and also discussed the future goals of the piezoelectric energy scavenging. Anton et al [34] discussed the advancement in piezoelectric energy harvesting within the time frame of 2003–2006. Bi-stable energy harvesting systems were briefly discussed in several papers [41, 42]. Traditional unit cell scavengers harvest power at a distinct frequency however, the bi-stable systems can allow multi-frequency harvesting. A detailed review of multi-frequency and broadband energy scavenging was presented by Zhu et al [43]. Saadon et al [44] specifically discussed the studies focused on powering the microelectromechanical system (MEMS) devices using piezoelectric materials. Cook-Chennault et al [36] briefly reviewed portable MEMS energy harvesters and discussed both the vibration and the electromagnetic based energy harvesting possibilities, including the

transduction medium and power supply systems (non-regenerative and regenerative). Calio et al [45] made a comprehensive review of piezoelectric cantilever beam-based energy harvesters. Harvester models based on piezoelectric coupling, differential materials, and geometries were discussed in detail. In addition, frequency tuning approaches, non-resonant models, rotational excitations, and energy harvesting circuitry were also reviewed by Calio et al [45]. Low power energy harvesting technologies have received notable interests from the biomedical technologies to power implantable medical devices. Energy harvesting studies related to this biomedical technology were discussed by Paulo et al [46]. Mateu et al [47] presented the available energy sources for low power energy scavenging and their possible applications. Power harvesting possibilities from the various operations in a building were also reviewed by Matiko et al [48]. Wireless sensor network (WSN) is an emerging application for low power energy scavenging. Studies performed to power WSN's were acknowledged by Wan et al [49]. Only recently, the acoustic metamaterials have been brought into the domain of energy harvesting because of their exceptional ability to create local resonance in a structure. Acoustic metamaterials are traditionally used for filtering acoustic/electromagnetic waves by introducing negative effective material properties [3]. Chen et al [50] tried to discuss the acoustic metamaterial-based energy harvesting approaches presented in various studies. Although the advancements in energy harvesting technologies have occurred in various approaches, a comprehensive discussion on available energy harvesting methods from various sources of dynamic energy, specifically using piezoelectric material, was not found in a comprehensive form. This chapter addresses this problem by discussing the state-of-the-art piezoelectric vibration-based energy harvesting approaches. Based on the vibration sources, energy harvesting

approaches can be classified into two major categories: intermittent and continuous. Continuous sources represent the models where the host structure vibrates at a specific frequency or band of frequencies, such as with machine vibration. Conversely, intermittent sources do not rely on a set of input frequencies, but instead, depends on the availability of the host structure deformation [51, 52]. The resulting power generation is created as a result of these deformations, as in the case of a device harvesting from irregular footsteps of a pedestrian. One major difference between a continuous and an intermittent source, is in their operating principal. While resonance phenomenon is the key to generate maximum power using the continuous source, intermittent source uses pure bending mode to harvest energy. Intermittent vibration usually comes from living and environmental sources. The motion of the human body parts has been the most commonly investigated living source of energy for harvesting; however, a few attempts were made to transform the animal motions into the electrical power. For environmental sources, wind and water flow are the most common forms. Continuous vibration operates using resonance phenomena. At resonance frequency, maximum power output can be recorded due to amplified deflection in the host structure. At an off-resonance frequency, power output is significantly lower compared to the resonance frequency. However, some nonlinear systems have recently been proposed for broadband energy harvesting, where the system exhibits resonance response at wider band of frequencies. Another popular approach for broadband energy harvesting is the use of linear generator arrays represents the response of a linear system). Two types of resonance behaviors are adopted in the domain of vibration-based energy harvesting: structural resonance and local resonance. While in the structural resonance, the whole host structure experiences resonance behavior, in local resonance, only a part/location of the

host structure exhibits resonance behavior. Typically, the models adopting the structural resonance are designed for high frequency energy harvesting since a smaller geometrical configuration can be allowed. However, large geometrical configuration is essential for low frequency applications. Low frequency energy scavenging with sub-wavelength scale geometry is possible by utilizing the local resonance phenomenon. The cantilever beam is the most popular and widely used model for the power harvesting that uses the structural resonance to harvest the energy. Additionally, a few papers have presented the energy scavenging possibilities using the plate type harvesters. Phononic and sonic crystals are traditionally used for filtering acoustic waves. However, very recently, both phononic and sonic crystals have been introduced to the domain of energy harvesting for low frequency power generation while maintaining the sub-wavelength scale geometry, employing their unique ability to exhibit local resonance phenomena. In this chapter, piezoelectric vibration-based energy harvesting approaches are reviewed. In addition, while discussing the state-of-the-art energy harvesting approaches, a comprehensive summary based on the essential energy harvesting parameters (such as power output and frequency range) have been made available for each category of the harvesters, for comparison. Finally, the future directions and the goals to improve the energy scavenging technologies are recommended.

2.3 **Future Possibilities for Energy Harvesting**

With the rapid development of low power electronics and technological advancement, the necessity and the use of batteries has increased tremendously. Conventional batteries possess several limitations/disadvantages and became crucial issues in the present technological era. Such limitations include chemical waste disposal, uncertain life, difficult or almost impossible replacement, and cost. Researchers have looked for alternative

sources of electrical energy to overcome these difficulties. Thus, vibration-based energy harvesting technology has become a prominent thread of investigation. Although this technology may currently provide insufficient power output for many electronics, the research discussed in this chapter provides sufficient promise of overcoming this shortcoming. The current major limitation of energy harvesting technologies is the low wattage, produced by the harvesters. Often the power output is not large to operate the target electronic device. Thus, either a major improvement in available or proposed in the energy harvesting models or novel harvesting methodologies that are needed to significantly bolster the power output. A few key factors must be considered to improve the power output are including power storage, device efficiency, and geometrical limitations. Two types of power storage methods are typically used in the energy harvesting domain: (i) rechargeable batteries and (ii) capacitors. Rechargeable batteries are recommended over capacitors because of the quick discharging behavior of the capacitor. Moreover, the battery possesses more power storage capacity than a capacitor. Since it is expected that the harvester will continuously generate electrical power from ambient vibration, a high-power storage system is required to supply the power when needed. Improving the power storage circuitry between the piezoelectric material and rechargeable battery may significantly increase the overall power output of the system. There is a need to optimize the power supply from the piezoelectric material to the storage system and minimize the circuit loss. Device efficiency is another important issue that needs to be addressed. The efficiency of a vibration-based energy harvester is mainly dependent on its conversion medium. Vibration energy harvesters convert mechanical energy into electrical energy with some sort of conversion medium, say, piezoelectric material. The amount of

mechanical energy generated, and the amount of energy converted into power is primarily dependent on the choice of the conversion medium and its arrangement and setting in the host structure. Additionally, the setting of the conversion medium in the device often influences the dynamic motion of the host structure and could decrease the input mechanical energy. These factors need to be optimized to obtain the highest possible power from the device. The geometry of the energy harvesting device is another major concern when optimizing its applicability and efficiency. Considering the operating frequency and application domains, energy harvesting technologies will eventually need to have a wider range of implant ability [12, 53, 54]. The geometrical configuration of an energy harvesting device will need to be managed depending on its operation site. However, power output and operating frequency of the conventional energy harvesting devices are greatly dependent on its geometry. Hence, future research needs to concentrate on these issues to optimize the related parameters before the devices can be used in many commercial operations. Finally, a complete guideline needs to be made on how the developed energy harvester can be implemented in various practical applications, such as wireless sensors or portable devices.

2.4 **Chapter Conclusion**

A background study on the vibration based piezoelectric energy harvesting is presented in this paper. The principal aim of this chapter is to discuss the various approaches that have been utilized to harvest electrical energy from different sources of mechanical energy using piezoelectric material. There have been many different approaches in harvesting energy from mechanical and acoustic vibration. Based on the vibration type of the host structure, energy harvesting approaches can be classified into two major categories:

intermittent source and continuous source. Both categories are then classified into smaller groups based on their operation.

CHAPTER 3:

MULTI-AXIAL ENERGY HARVESTING

3.1 Abstract

Due to the limited availability and high depletion rates of nonrenewable energy sources as well as environmental concerns, the scientific community is urged to explore and harness alternative, clean energy sources. In this study, a novel piezoelectric energy harvester based on a metamaterial structure is proposed which is capable of scavenging energy from low-frequency, multi-axial ambient vibrations. The proposed energy harvester is based on a mass-in-mass Phononic Crystal structure and is comprised of a spherical heavy core resonator and piezoelectric wafers, encapsulated in a cylindrical rubber matrix, and encased in a rigid cubic frame. The proposed cell behaves effectively like a negative mass in the vicinity of its resonance frequencies and entraps the vibration energy as dynamic strain. The captured kinetic energy is then transformed to electric potential using three Lead-Zentrale-Teichmann wafers, optimally embedded in the cell's soft constituent. In this paper, the proposed energy harvester cell is analytically modeled, numerically simulated via COMSOL Multiphysics software, and experimentally validated using a variety of uni- and multi-axial vibration excitations.

3.2 Introduction

Estimations show that energy consumption will rise by more than 50 percent globally

from 2008 through 2035 [55]. For instance, in the United States alone, it is estimated that smart phones and other mobile gadgets alike consume more than one million Watt-hour of electricity each year [56]. Considering the limited availability and depletion rates of nonrenewable energy sources as well as the environmental side effects, the scientific community is urged to explore and harness alternative, clean energy sources. To address such a demand for electric power, researchers have proposed numerous solutions such as scavenging energy from ambient acoustic and vibrational energy sources [34-36], among many other approaches [57, 58].

A recent review paper [59] shows that the increased use of low-power devices, such as smart phones and micro-electromechanical systems/sensors, has raised substantial interest in the field of piezoelectric energy harvesting technology [59]. Piezoelectric energy harvesters utilize active materials that produce an electric charge when mechanically stressed [33]. The majority of such harvesters are fashioned as cantilever beams integrated with piezoelectric materials [60-62], and function based on the resonance phenomenon as the operating principle. For instance, millimeter cantilever (4 to 10 mm) energy scavengers have been designed targeted for frequencies in the range of 20 kHz to 3 MHz [6, 51, 62, 63]. Energy capture from low-frequency vibrations using cantilever-based harvesters, however, is challenging as the output power quickly decays with the decrease in frequency [6, 7, 64]. The physical principles of such beams do not easily translate to low-frequency vibration domain as they would require large geometrical beam/structure dimensions for low frequencies [65-69].

Energy harvesting from low-frequency ambient vibrations is attractive due to the

abundance of such vibrations sources [70] such as in [71-75]. To alleviate challenges associated with low-frequency vibration-based energy harvesters, application of piezoelectric metamaterials has been proposed. Metamaterials are artificial assemblies of typical elements with engineered compositional geometries and structural patterns, and possess properties not easily found in natural elements [76]. Acoustic metamaterials are conventionally used for controlling and guiding acoustic waves and vibrations [77] and obey the laws of negative refractive index materials, obtained via the modification of the mass density and bulk modulus [76]. A negative modulus may cause an element to expand while under compression, whereas a medium with negative density may accelerate in the opposite direction of applied force at particular frequencies [77]. Such metamaterials act like stop-band filters for vibrational waves by trapping them inside their constituents as strain energy. Therefore, it has been suggested to capture and transform this kinetic energy to electric potential with the introduction of active materials capable of electromechanical transduction (e.g., piezoelectric wafers) [78-84].

In a recent attempt to use acoustic metamaterials for energy scavenging [85], a Phononic Crystal (PC) cell was proposed. PCs are characterized by their internal compositional cavities capable of entrapping vibrational energy at resonance frequencies due to the low transmissibility of the cells at those frequencies. Extant literature supports harvesting energy using these cells from high frequency content of ambient vibrations [86]. However, as it is theoretically possible to shift the resonance frequencies by altering the material properties of the cell's constituents and its configuration, in this study, a PC cell is proposed for the purpose of harvesting

energy from low-frequency vibrations (i.e., <1 KHz). The proposed cell is based on a mass-in-mass structure and is comprised of a lead core resonator and three piezoelectric wafers (i.e., Lead-Zentrale-Teichmann [PZT-5H]), optimally encapsulated in a soft rubber matrix and encased in an aluminum frame.

Based on a recent review paper on energy harvesting devices [59], many ambient sources of vibration bear high energy content in the multi-axial frequency range of 400 Hz to 1 KHz. Examples of such sources include railway tracks' vibration when trains pass, vibration of highways' sound wall panels due to passing cars, and vibration of airplanes' wings and cabin's internal structure during flight [59], to name a few. Thus, as a proof of concept, the proposed PC cell in this study is designed such that it filters vibrations at ~530 Hz and converts the captured energy into electric potential in order to power small electronic devices. The proposed structure is capable of transducing mechanical vibrations, freely occurring in three-dimensional (3-D) space, to electric potential.

The current paper is structured as the following. Next section outlines the structure of proposed cell and models its acousto-dynamic behavior from an analytical and numerical point of view. Section III describes the fabrication process of the cell as well as the experimental setup and electronic circuitry developed. In section IV, numerical and experimental results are provided and discussed. Finally, section V concludes the paper and provides insight into future direction [4, 6, 7, 87-90].

3.3 Structural Design and Modeling

In this section, the proposed PC cell's structure and components are described, and its acousto-dynamic behavior is modeled analytically as well as numerically.

3.3.1 Structural Design of Phononic Crystal Cell

To create frequency band gaps for the purpose of acoustic filtration, PC cells are usually comprised of a mass-in-mass structure with constituents of different material characteristics. In such a unit, with an accurately designed geometric configuration, a negative effective dynamic mass may be obtained [91, 92]. At the resonance frequency, the wave energy is trapped inside soft material constituents as dynamic strain energy. In our initial analyses, it was realized that in a PC cell, upon embedding a piezoelectric wafer, two major local resonances typically emerge including the core mass resonance along the excitation direction and the core mass resonance perpendicular to the surface of piezoelectric wafer unless the excitation direction coincides with its thickness axis. Furthermore, a less-dominant resonance may occur in the gravitational direction of the core mass. Therefore, it is hypothesized that, if these vibration modes are strategically combined, energy harvesting from ambient vibrations is maximized.

Following this hypothesis, in this study, it is suggested to embed three PZT-5H wafers (manufactured by Steiner and Martins, Inc., dimensions: 12mm x 0.6mm) in the PC cell such that their thickness axes coincide with the axes of three-dimensional excitation. The PC cell proposed in this study consists of a spherical heavy core resonator (made of lead) and three smart material pieces, which are all strategically embedded in a rubber cylindrical encapsulant, and collectively encased by an

aluminum cubic housing. The cell's structure and the placement of the PZT-5H wafers, as well as the overall dimensions are illustrated in Figure 3.1. For the material characteristics of the cell's individual elements refer to Table 3.1.

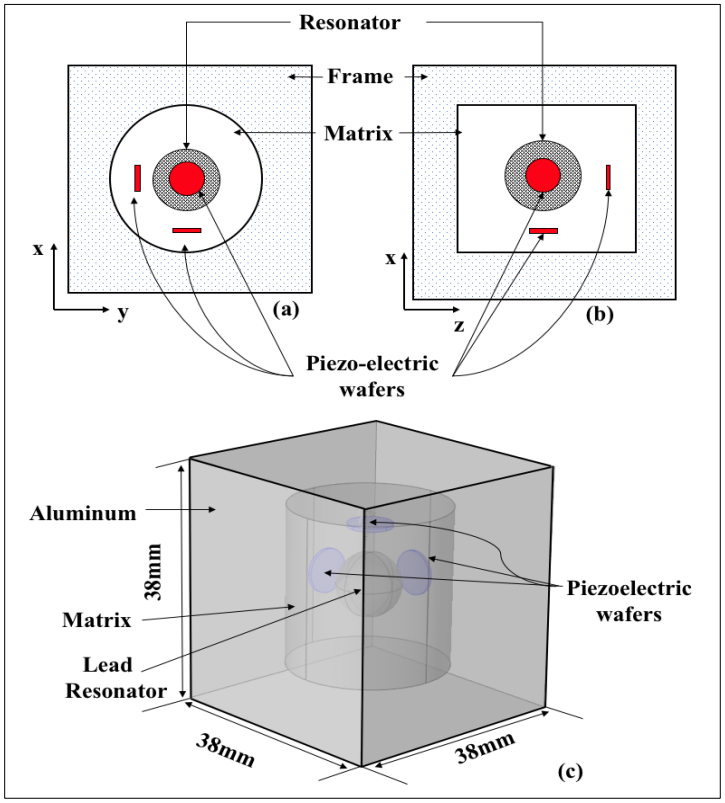

Figure 3.1: Proposed structure and dimension of the PC cell and placement of piezoelectric wafers.

Table 3.1: Material properties of cell constituents

Material	Density (kg/m^3)	Young's Modulus (Pa)	Poisson's Ratio
Rubber	1600	9.94E+05	0.47
Aluminum	2700	6.89E+10	0.33
Lead	11340	1.35E+10	0.43

At frequencies in the vicinity of resonance, the unit cell behaves like a medium with a negative effective dynamic mass due to special decay of wave amplitude [93].

Also, frequency band gaps are formed due to the lead core's resonance. Those resonance frequencies and, hence, the corresponding band gaps, may be altered via the adjustment in the core's size [17]. Similarly, weakly-dispersed band gaps are created due to local resonance in the soft rubber matrix. One can establish extra band gaps in a unit cell by embedding extra resonators [93, 94]. As aforementioned, since vibration energy is entrapped in the unit cell's soft constituent at the resonance frequencies, it is hypothesized that by placing piezoelectric wafers inside the rubber, between the core mass and the frame, the strain energy can be captured and converted to electric potential. In the rest of this section, an analytical modeling and finite-element analysis are conducted to investigate this hypothesis.

3.3.2 Analytical Modeling

As the cell practically functions as a mechanical stop-band filter, in this sub-section, it is attempted to obtain a predictive analytical model of the PC cell proposed.

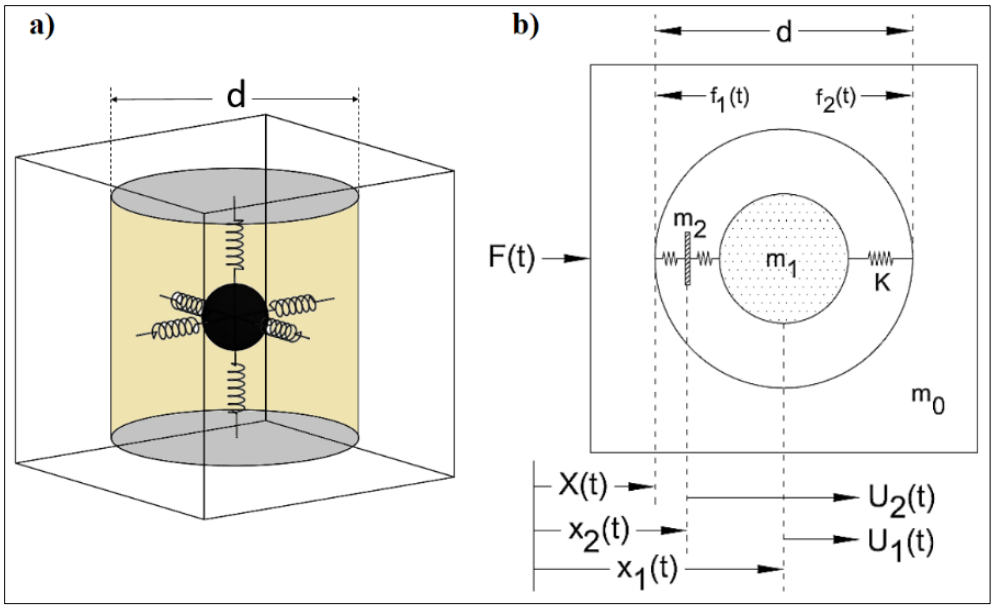

Figure 3.2: Spring-mass representation of PC cell (a) 3-D lumped model and (b) simplified 1-D model.

Figure 3.2a illustrates the lumped model of the PC cell proposed in this study as a 3-D mass-spring system. Although the cell vibrates freely in a three-dimensional space, for the sake of computational simplicity and due to the symmetry/similarity of the structure in x, y, and z axes, the cell's model is first considered in a single direction as depicted in Figure 3.2b.

Table 3.2: Model Parameters and Notations

Symbol	Quantity
K	Stiffness of rubber
ω	Excitation frequency
m_0	Aluminum frame's mass
m_1	Lead core's mass
m_2	PZT wafer's mass
P	Linear momentum
F(t)	External force acting on aluminum frame
$f_1(t)$	Internal force acting on PZT wafer
$f_2(t)$	Internal force acting on Lead core
X(t)	Displacement
$X_{0,\,init}$	Initial position
U_0	Displacement of aluminum frame
U_1	Displacement of lead core
U_2	Displacement of PZT wafer
V_0	Velocity of aluminum frame
v_1	Velocity of lead core
v_2	Velocity of PZT wafer
x_1	Position of lead core
x_2	Position of PZT wafer
u_1	Complex-valued displacement of lead core
u_2	Complex-valued displacement of PZT

In Figure 3.2b, m_0, m_1, m_2, and k denote mass of the aluminum frame, mass of the lead core, mass of the PZT wafer, and its stiffness, respectively. Model parameters are defined in Table 3.2. According to this simplification, the effective mass of the

cell's structure and, hence, a rough estimate of the resonance frequency can be obtained. This simplified model can be used to design the desired resonance frequency. Subsequently, finite element analysis (FEA) will be performed, in the following sub-section, in order to numerically verify the design parameters and fine-tune resonance frequency.

According to Figure 3.2b, the total linear momentum of the system can be defined as:

$$P_{tot} = P_{frame} + P_{core} + P_{PZT} \quad (3\text{-}1)$$

If we consider

$$F(t) = \mathrm{Re}\,(\hat{F}e^{-i\omega t}) \quad (3\text{-}2))$$

$$f_1(t) = \mathrm{Re}\,(\hat{f}_1 e^{-i\omega t}) \quad (3\text{-}3))$$

$$f_2(t) = \mathrm{Re}\,(\hat{f}_2 e^{-i\omega t}) \quad (3\text{-}4))$$

Position and velocity of the left side of frame are:

$$X(t) = X_{0,\,init} + U_0(t) = X_0 + \mathrm{Re}\,(\hat{U}_0\, e^{-i\omega t}) \quad (3\text{-}5))$$

$$v_0(t) = dX/dt = \mathrm{Re}\,(-i\omega\hat{U}_0\, e^{-i\omega t}) = \mathrm{Re}\,(\hat{v}_0\, e^{-i\omega t}) \quad (3\text{-}6))$$

Therefore, the frame linear momentum is:

$$P_{frame} = m_0\, v_0(t) = m_0\, \mathrm{Re}\,(\hat{v}_0\, e^{-i\omega t}) \quad (3\text{-}7))$$

If $U_1(t)$ and $U_2(t)$ are the relative displacement of the core and the PZT wafer, respectively, the positions of the core and the PZT wafer for harmonic motions are:

$$x_1(t) = X_0 + d/2 + \mathrm{Re}\,(\hat{u}_1\, e^{-i\omega t}) \quad (3\text{-}8))$$

$$x_2(t) = X_0 + d/4 + \mathrm{Re}\,(\hat{u}_2\, e^{-i\omega t}) \quad (3\text{-}9))$$

where $u_1(t) = U_0(t) + U_1(t)$ and $u_2(t) = U_0(t) + U_2(t)$. One can write the velocities as:

$$v_1(t) = dx_1/dt = \mathrm{Re}\,(-i\omega\,\hat{u}_1 e^{-i\omega t}) = \mathrm{Re}\,(\hat{v}_1\, e^{-i\omega t}) \quad (3\text{-}10))$$

$$v_2(t) = dx_2/dt = \mathrm{Re}\,(-i\omega\,\hat{u}_2 e^{-i\omega t}) = \mathrm{Re}\,(\hat{v}_2\, e^{-i\omega t}) \quad (3\text{-}11))$$

where $\hat{v}_1 = -i\omega\hat{u}_1$ and $\hat{v}_2 = -i\omega\hat{u}_2$. Therefore, linear momentum of the core and PZT are:

$$P_{core}(t) = m_1\, v_1(t) = m_1\, \mathrm{Re}\,(\hat{v}_1\, e^{-i\omega t}) \quad (3\text{-}12))$$

$$P_{PZT}(t) = m_2\, v_2(t) = m_2\, \mathrm{Re}\,(\hat{v}_2\, e^{-i\omega t}) \quad (3\text{-}13))$$

According to eqn. (3-1), (3-7), (3-12), and (3-13), the total linear momentum can be written as:

$$P_{tot} = m_0\, \mathrm{Re}\,(\hat{v}_0\, e^{-i\omega t}) + m_1\, \mathrm{Re}\,(\hat{v}_1\, e^{-i\omega t}) + m_2\, \mathrm{Re}\,(\hat{v}_2\, e^{-i\omega t}) \quad (3\text{-}14))$$

$$P_{tot} = \mathrm{Re}\,(\hat{P}\, e^{-i\omega t}) \quad (3\text{-}15))$$

According to Newton's second law of motion:

$$F(t) = dP(t)/dt \quad (3\text{-}16))$$

Therefore

$$\hat{F} = -i\omega\,(m_0\hat{v}_0 + m_1\hat{v}_1 + m_2\hat{v}_2) \quad (3\text{-}17))$$

Figure 3.3 demonstrates free-body diagrams of the lead core and the PZT wafer. Using Hooke's law:

$$-f_1(t) = 2KU_2(t) = f_{i1}(t) \quad (3\text{-}18))$$

$$-f_{i2}(t) = KU_1(t) = f_2(t) \quad (3\text{-}19))$$

Displacements are as:

$$U_1(t) = u_1(t) - U_0(t) = \mathrm{Re}\,(\hat{u}_1\, e^{-i\omega t}) - \mathrm{Re}\,(\hat{U}_0\, e^{-i\omega t}) \quad (3\text{-}20))$$

$$U_2(t) = u_2(t) - U_0(t) = \mathrm{Re}\,(\hat{u}_2\, e^{-i\omega t}) - \mathrm{Re}\,(\hat{U}_0\, e^{-i\omega t}) \qquad (3\text{-}21))$$

Therefore:

$$\hat{f}_1 - \hat{f}_{i1} = 4K\,(\hat{U}_0 - \hat{u}_2) \qquad (3\text{-}22))$$

$$\hat{f}_{i2} - \hat{f}_2 = 2K\,(\hat{U}_0 - \hat{u}_1) \qquad (3\text{-}23))$$

$$f_1(t) - f_{i1}(t) = -\,m_2 \frac{d^2x_2}{dt^2} = m_2\,\mathrm{Re}\,(-\omega^2\,\hat{u}_2\, e^{-i\omega t}) \qquad (3\text{-}24))$$

$$\hat{f}_1 - \hat{f}_{i1} = -m_2\,\omega^2\,\hat{u}_2 \qquad (3\text{-}25))$$

$$f_{i2}(t) - f_2(t) = m_1 \frac{d^2x_1}{dt^2} = m_1\,\mathrm{Re}\,(-\omega^2\,\hat{u}_1\, e^{-i\omega t}) \qquad (3\text{-}26))$$

$$\hat{f}_{i2} - \hat{f}_2 = -m_1\,\omega^2\,\hat{u}_1 \qquad (3\text{-}27))$$

Therefore:

$$\hat{u}_2 = \frac{4K}{4k - m_1\omega^2}\,\hat{U}_0 \qquad (3\text{-}28))$$

$$\hat{u}_1 = \frac{2K}{2k - m_1\omega^2}\,\hat{U}_0 \qquad (3\text{-}29))$$

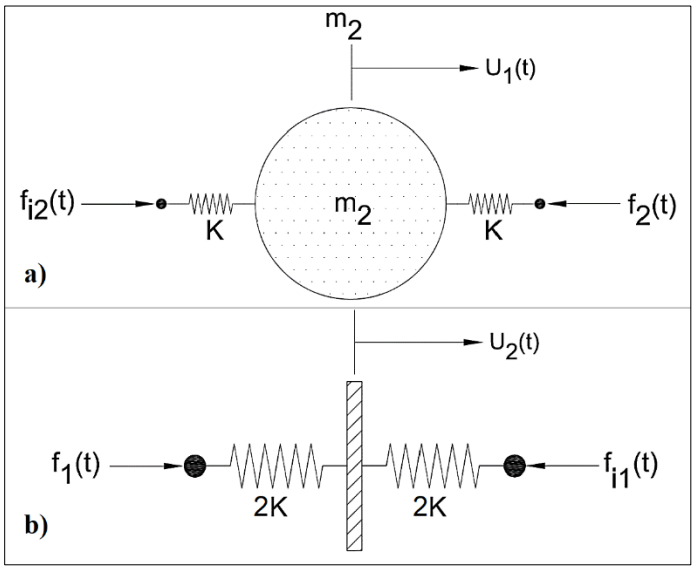

Figure 3.3: (a) Free-body diagram for the spring-mass system those are connected to the core. (b) Free-body diagram for the spring-mass system those are connected to the piezoelectric material.

Since $v_0 = -i\omega\hat{U}_0$, $v_1 = -i\omega\hat{u}_1$, and $v_2 = -i\omega\hat{u}_2$:

$$\hat{v}_2 = \frac{4K}{4k - m_1\omega^2}\hat{V}_0 \qquad (3\text{-}30))$$

$$\hat{v}_1 = \frac{2K}{2k - m_1\omega^2}\hat{V}_0 \qquad (3\text{-}31))$$

Hence, the linear momentum is

$$\hat{P} = m_0\,\hat{v}_0 + m_1\frac{2K}{2k - m_1\omega^2}\hat{v}_0 + m_2\frac{4K}{4k - m_2\omega^2}\hat{v}_0 = M_{eff}\hat{v}_0 \qquad (3\text{-}32))$$

Therefore, the effective mass is obtained as:

$$M_{eff} = m_0 + \frac{2Km_1}{2K - m_1\omega^2} + \frac{4Km_2}{4K - m_2\omega^2} \qquad (3\text{-}33))$$

In this equation, based on the properties and dimensions of the materials used, m_0, m_1, m_2, and k are calculated to be 148.15 g, 7.41 g, 0.22 g, and1000 N/m, respectively.

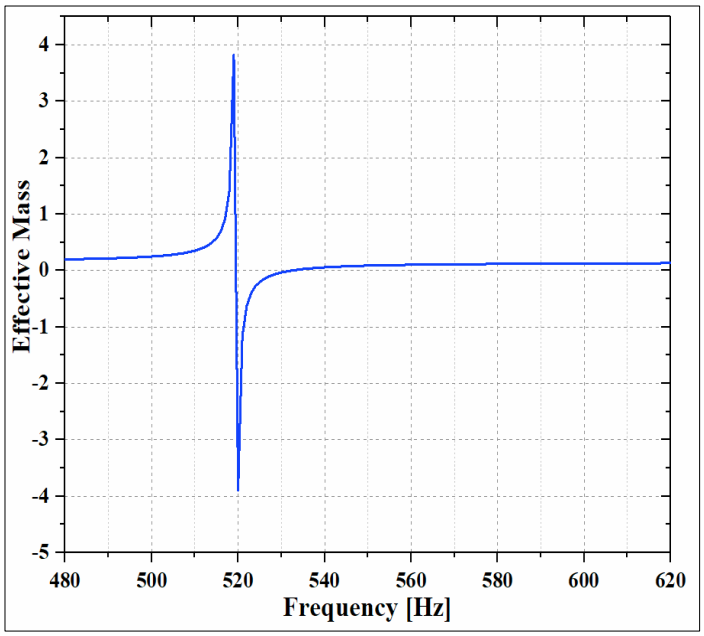

Figure 3.4: Effective mass of the proposed Phononic Crystal cell.

As shown in Figure 3.4, according to equation of M_{eff}, the cell theoretically

experiences a negative effective mass at ~519 Hz, and it constitutes a resonance frequency. At this frequency, the kinetic energy is entrapped within the soft rubber and, providing the PZT-5H wafer is solely polarized in its thickness direction, it experiences a maximum harmonic compressive strain perpendicular to its surface.

3.3.3 Numerical Analysis

To further investigate the cell's acoustic behavior and to validate the analytical outcomes, a numerical modeling, i.e., finite-element analysis, is performed using the COMSOL Multiphysics software. In this analysis, we investigate the PC cell's modal displacement to understand its oscillation pattern at resonance. To this end, displacement and pressure signals are used as loading inputs to the PC cell.

Unlike the analytical modeling, the FEA is performed considering all three PZT-5H wafers, one perpendicular to each x, y, and z axes. Boundary condition for displacement is applied along the axis perpendicular to the wafers in all three axes such that excitation axis coincides with the PZT-5H wafers.

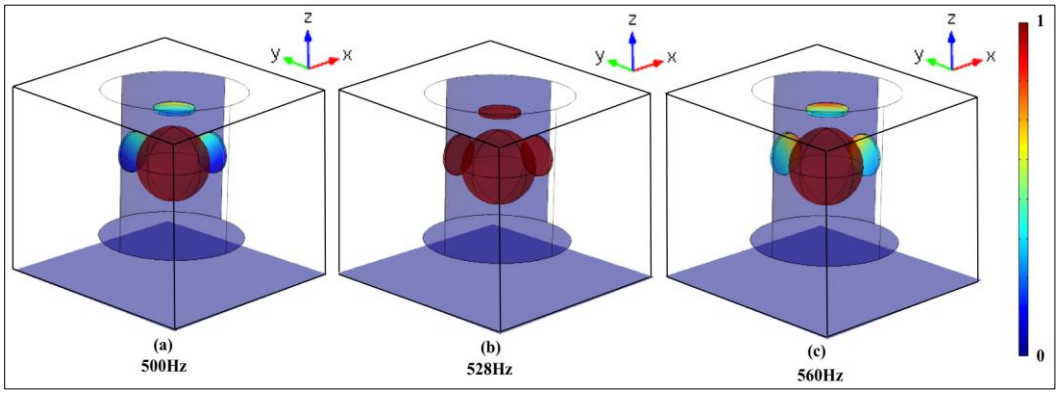

Figure 3.5: Displacement plot to harmonic unit displacement input load at (a) 500 Hz, (b) 528 Hz, and (c) 560 Hz.

Interestingly, both loading conditions result in very similar frequency responses of the PC cell. For the sake of brevity, Figure 3.4 demonstrates the dynamic response

of the cell's constituents only to unit harmonic displacement (i.e., 1 mm) at the resonance frequency. The results indicate that the resonance frequency occurs at ~528 Hz, which is in close agreement with the analytical outcomes. The negligible deviation may be explained by the fact that the analytical modeling was simplified by considering a unidirectional structure. For the sake of comparison, Figures 3.5a and 3.5c show the frequency response to displacement input at two other frequencies further away from resonance, i.e., 500 Hz and 560 Hz. According to Figure 3.5, the three piezoelectric wafers experience the maximum strain at the resonance and, hence, can generate the maximum electric potential at this frequency. To further illustrate the displacement pattern of the core mass, the displacement plot is depicted from a top and side view at the resonance frequency in Figure 3.6.

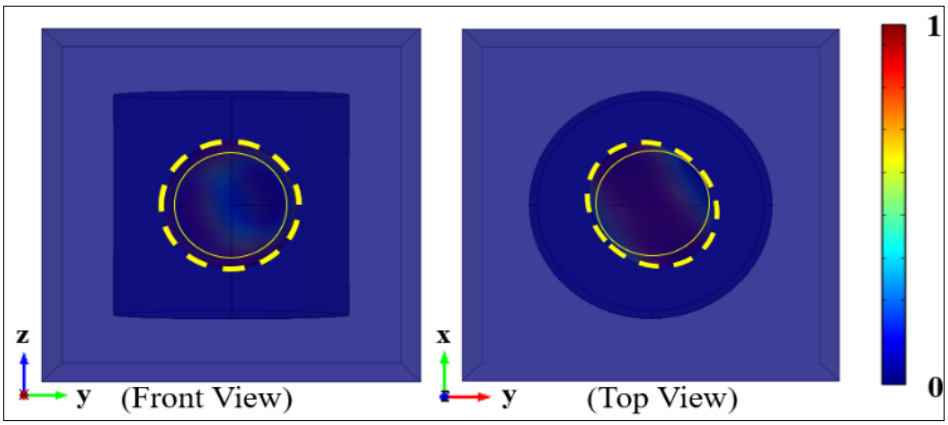

Figure 3.6: Displacement of the PC cell's constituents at resonance from (left) front view and (b) top view.

From an acoustic point of view, the PC cell's dispersion trajectory also is studied in the vicinity of resonance frequency. To that end, the PC cell was arranged periodically, modeled as an infinite beam in the x and y axes, and boundary conditions were considered at the cell's edges in accordance with the Bloch–Floquet theorem [17].

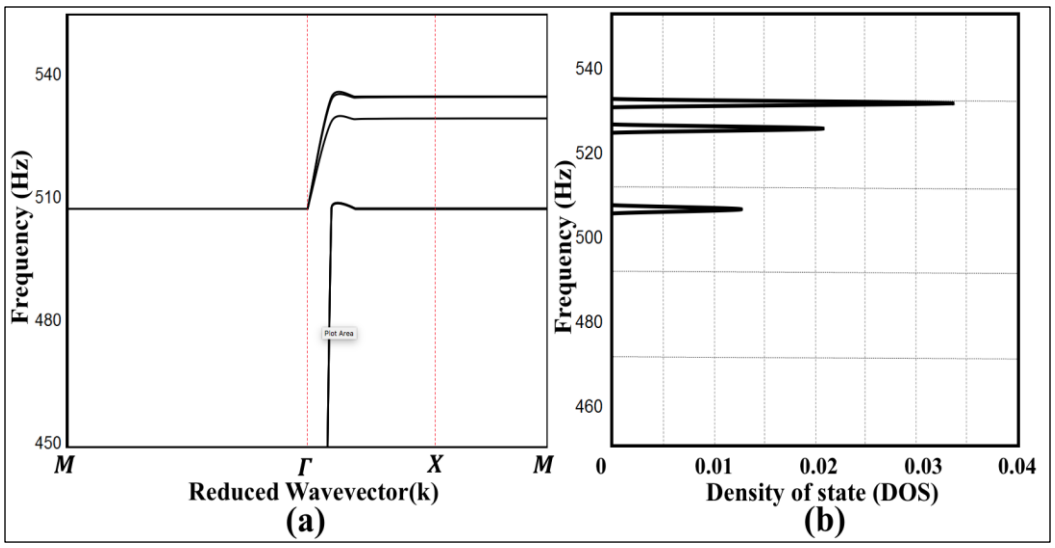

Figure 3.7: The proposed cell's (a) dispersion curve and (b) state density.

Such boundary conditions are appropriate for this problem due to the small-signal nature of the fluctuations occurring in periodic structures. Figure 3.7a depicts the cell's dispersion trajectory containing five flat bands denoting local resonances. As can be seen, a pair of the bands collide near 507 Hz, and another pair co-occur around 530 Hz, whereas the last band occurs at ~522 Hz.

Alternatively, we numerically computed the states' density (i.e., the system's number of shape modes at a single frequency) in the interval of 450-560 Hz, as depicted in Figure 3.7b. A highly dense level indicates that several shape modes exist in that vicinity. If the frequency band is flat in an interval in the DC, maximum states' density can be achieved in that interval. This, in turn, implies the group velocity is approximately non-existent and the structure traps the wave energy. According to Figure 3.7 and based on the peaks in the density of state corresponding to the straight bands in the dispersion curve, one can conclude that there is a local resonance in the frequency range of 507-530 Hz. For more information regarding density of state and dispersion curves refer to [95].

3.4 Sensor Development and Experimental Validation

In this section, the fabrication process, electronic circuitry, and experimental setup are explained.

3.4.1 Phononic Crystal Cell Fabrication

In order to experimentally validate the analytical and numerical modeling performed in the previous section, the proposed PC cell is custom fabricated in house with the material and dimensions as per Table 3.1 and Figure 3.1, respectively. The fabrication process is as follows.

Three PZT-5H wafers is fabricated. For this purpose, a scaffold system including three separate parts are designed and 3-D printed; (i) a cubic mold with a cylindrical hole, (ii) a bottom lid with a few artifacts to hold the core resonator and two wafers in place, and (iii) a slider pin to hold the third wafer (Figure 3.8a). These three parts, along with the core resonator and the PZT-5H wafers, are assembled together to prepare a complete mold for the Silicone rubber (Figure 3.8b and 3.8c). Upon assembly of the scaffold system, liquid rubber (Mold Star 20T) is poured in the mold, fully submerging the PZT-5H wafers and the core mass (Figure 3.8d). The cure time of the rubber is six hours. Four hours later, before the liquid rubber completely cures, the bottom lid and the slider pin are gently removed from the mold leaving the lead core and wafers inside the cylinder. Immediately after removal of those parts, the empty space is filled with newly prepared liquid rubber to avoid any inconsistency in the composition. This process and the corresponding timing were developed after a few trials in order for the rubber parts to have a seamless, homogenous bond (Figure 3.8e).

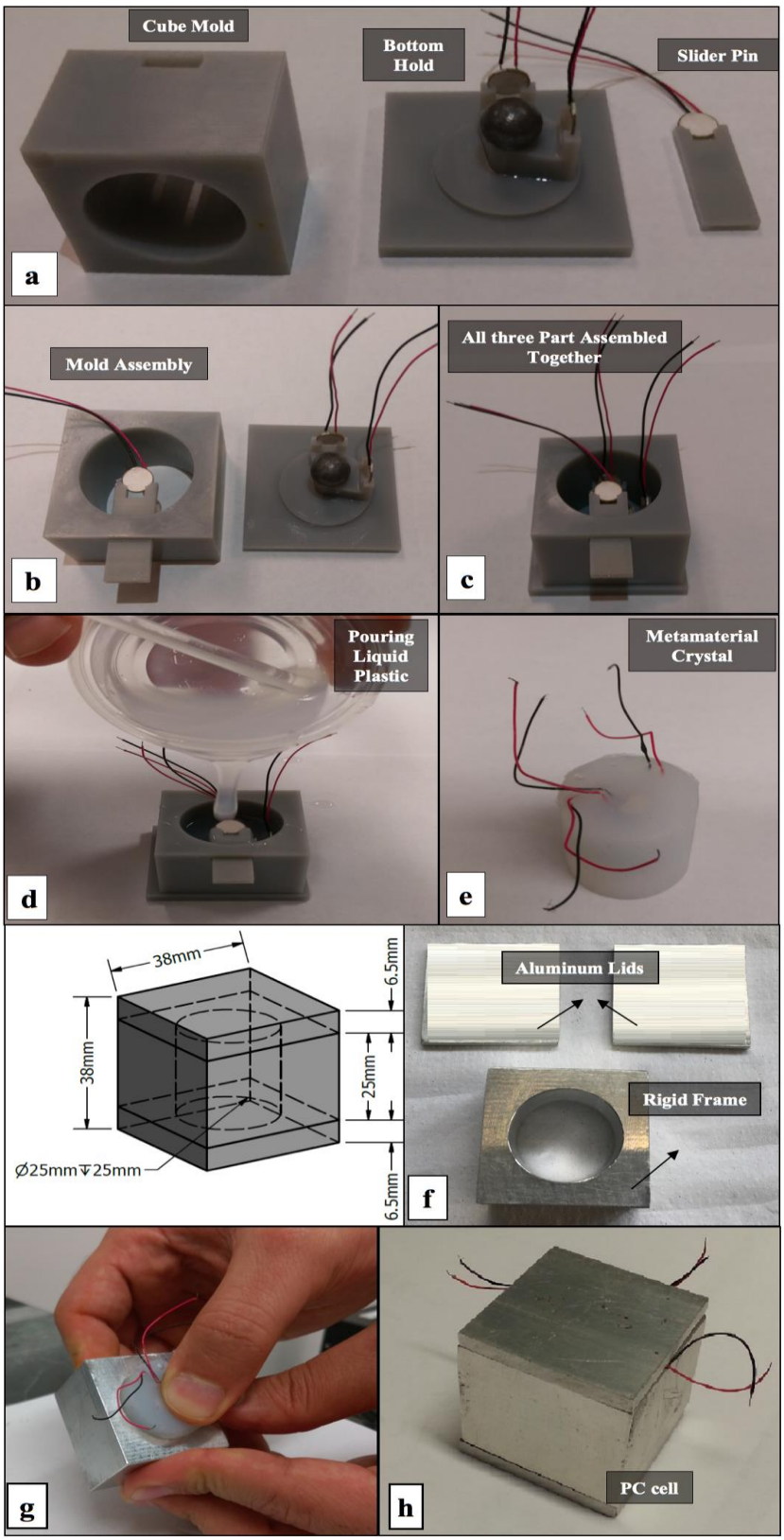

Figure 3.8: Fabrication steps of the proposed PC cell.

Finally, an aluminum frame and lids are machined and assembled (Figure 3.8f). Once the rubber matrix is completely cured, it is gently inserted inside the aluminum block, and the two lids are glued to the top and bottom of the frame (Figure 3.8h).

First, the cylindrical rubber matrix containing the lead core resonator and the three PZT-5H wafers is fabricated. For this purpose, a scaffold system including three separate parts are designed and 3-D printed; (i) a cubic mold with a cylindrical hole, (ii) a bottom lid with a few artifacts to hold the core resonator and two wafers in place, and (iii) a slider pin to hold the third wafer (Figure 3.8a). These three parts, along with the core resonator and the PZT-5H wafers, are assembled together to prepare a complete mold for the Silicone rubber (Figure 3.8b and 3.8c). Upon assembly of the scaffold system, liquid rubber (Mold Star 20T) is poured in the mold, fully submerging the PZT-5H wafers and the core mass (Figure 3.8d). The cure time of the rubber is six hours. Four hours later, before the liquid rubber completely cures, the bottom lid and the slider pin are gently removed from the mold leaving the lead core and wafers inside the cylinder. Immediately after removal of those parts, the empty space is filled with newly prepared liquid rubber to avoid any inconsistency in the composition. This process and the corresponding timing were developed after a few trials in order for the rubber parts to have a seamless, homogenous bond (Figure 3.8e). Finally, an aluminum frame and lids are machined and assembled (Figure 3.8f). Once the rubber matrix is completely cured, it is gently inserted inside the aluminum block, and the two lids are glued to the top and bottom of the frame (Figure 3.8h).

3.4.2 Electronic Circuitry

In order to utilize the electric potential generated by the piezoelectric wafers in

the PC cell, a custom-made energy harvesting circuitry was designed and constructed in-house (Figure 3.9). This circuitry is comprised of four sub-modules each of which is capable of interfacing with a different battery voltage level (i.e., 0.8V, 1.5V, 2.3V, and 3.0V). Each submodule includes an LTC3588 piezo harvester from Linear Technologies, which contains a low-loss full-wave bridge rectifier for the piezo element, a highly efficient buck converter, and other required circuitry to pump the harvested energy to a connected battery cell. Additionally, an input protective shunt allows higher charge accumulation for a certain amount of input capacitance, which is ideal for interfacing with high output impedance energy harvesting elements such as piezoelectric transducers.

Figure 3.9: Energy harvesting electronic circuitry.

The chipset has a very-low quiescent current lockout mode as well as a hysteresis window that enables a charge to add up in a capacitor in the under-voltage state. As soon as the voltage level reaches a certain minimum, the built-in buck converter efficiently releases the charge to the output cell and, subsequently, enters an ultra-low power sleep mode. This process starts anew when the accumulated charge

reaches the hysteresis level again. In each sub-module, the output voltage level is selectable by the user via two jumper headers [96-103].

3.4.3 Experimental Setup

In order to experimentally validate the functionality of the developed PC cell and systematically characterize its performance, in accordance with the intended features of the cell, a vibration exciter with the capability of 3-D excitation in a wide range of frequencies is required. The majority of vibration exciters available in the market as well as those custom-made, however, only provide unidirectional vibration although general ambient sources of vibration occur freely in 3-D space. Therefore, in our integrated Material Assessment and Predictive Simulation (iMAPS) lab, we have designed and fabricated Acousto-Electrodynamic Vibration Exciter, AEVE 3D, which can provide coupled/uncoupled vibrations in a wide frequency range [31, 88]. In this study, AEVE 3D was utilized to perform validation experiments with 1-D and 3-D loading excitations. AEVE 3-D consists of three mechanical exciters and three speakers which are connected in three Cartesian directions. Sinusoidal signals with desired frequency are generated and separately fed to each actuator. Figure 3.10 shows the experimental setup. In this study, only the mechanical exciters are used while the speakers remain off. As far as the mechanical shakers, AEVE 3D can provide a variety of uni- or multi-directional mechanical vibrations. For 3D excitations, all three shakers actuate the vibration tray at the same time, while in 1D excitations, only one shaker operates. To mount the fabricated unit cell firmly in the center of the AEVE 3-D's end-effector, a custom-made aluminum mounting structure is designed and fabricated (Figure 3.10a). Figures 3.10b and 3.10c demonstrate the

mounting procedure and how the PC cell is firmly placed in AEVE 3D such that each PZT-5H wafer in the cell is perpendicular to an excitation axis.

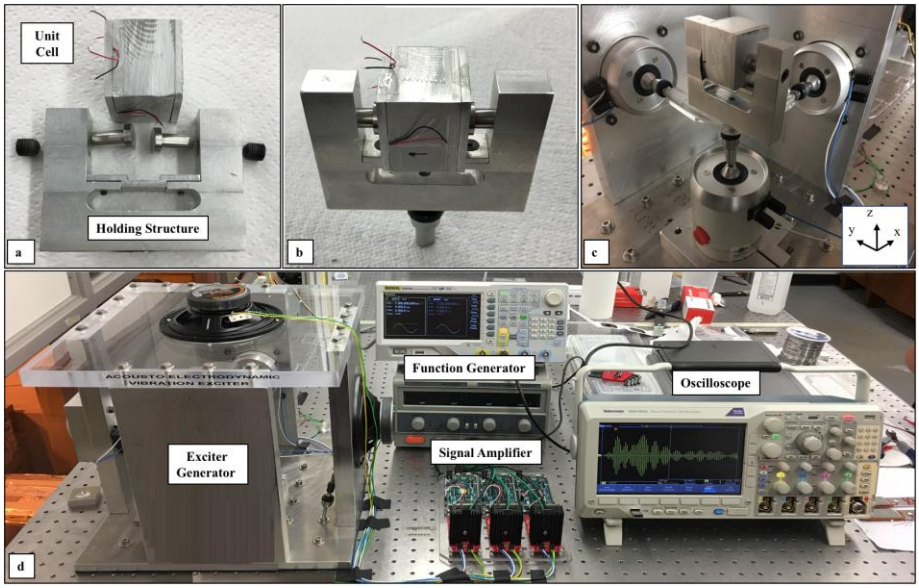

Figure 3.10: (a) Fabricated aluminum end-effector, (b) PC cell mounted in the aluminum end-effector, (c) PC cell mounted inside AEVE 3-D's actuation tray, (d) experimental setup including AEVE 3-D, function generator, signal amplifier, and oscilloscope to sense the generated electric potential.

3.5 Results and Discussions

Sinusoidal signals with frequencies in the range of 500 Hz to 550 Hz, evenly distributed at every 2 Hz, were generated by the AEVE 3-D's main electronic module and, after an amplification stage, were fed to its individual mechanical shaker in each direction. AEVE 3D's shakers output an RMS acceleration of 1.2g (g = 9.81 m/s^2). Four different excitation modes were adopted; 1) independent excitation solely in the x-axis, 2) independent excitation solely in the y-axis, 3) independent excitation solely in the z-axis, and finally 4) 3-D excitation in a coupled manner in x, y, and z axes. In the uncoupled, unidirectional excitations, only one actuator applied vibration while the other two were kept idle. Additionally, in the three uniaxial excitations, the output

voltage of the corresponding PZT-5H wafer was separately captured against a three 1kΩ resistive loads, and the corresponding output power was calculated by monitoring the current flows through the resistors. In the multi-axial excitation, however, the three output terminals were connected together with a parallel configuration, and the overall output power was fed to a 1kΩ resistor. Each excitation experiment was repeated 10 times at each frequency.

To be consistent with the experimental procedure, a 1kΩ resistor was added to the FEA models. Figure 3.11 depicts the output power obtained through FEA simulation and empirical testing for individual excitations in the x-, y-, and z-directions. As can be seen in this figure, the simulation results indicated that at 12g m/s^2 acceleration produced by AEVE 3-D, maximum output power of 9.5 mW, 9.5 mW, and 9.6 mW are generated in the x-, y-, and z-axes, respectively. The resonance frequency for these individual excitations occurs at 532 Hz, 532 Hz, and 530 HZ, respectively. Figure 3.11 also illustrates the output power harvested during the experimental tests. The associated uncertainty in the experimental data, obtained through repetitive experimentation, is also depicted. As can be seen, the empirical data and simulation results are in close agreement with each other. A number of factors may contribute to this discrepancy such as human error, fabrication errors, mismatches in the material properties, imperfections in the placement and tilt of the PZT wafers, ambient temperature, and imperfect adhesion between layers. The experimental data and simulation results for the 3-D excitation of the PC cell are shown in Figure 3.12. As can be seen in this figure, the maximum output power harvested from the cell is ~78mW at ~538 Hz, whereas numerical simulation shows

a maximum of ~86 mW at ~532 Hz. Again, both results are in close accordance with each other.

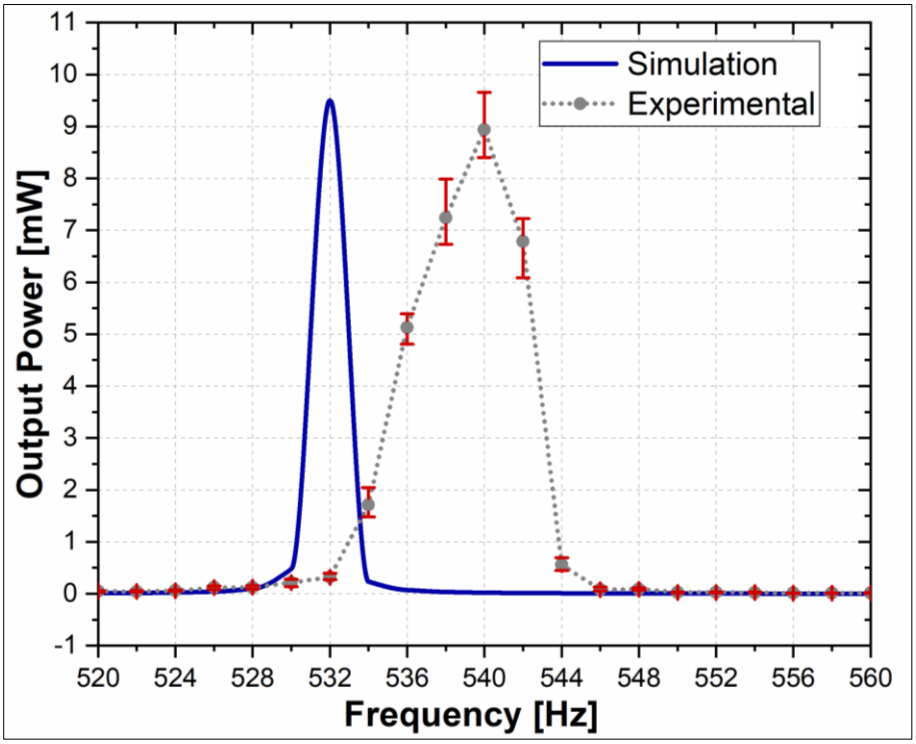

(a)

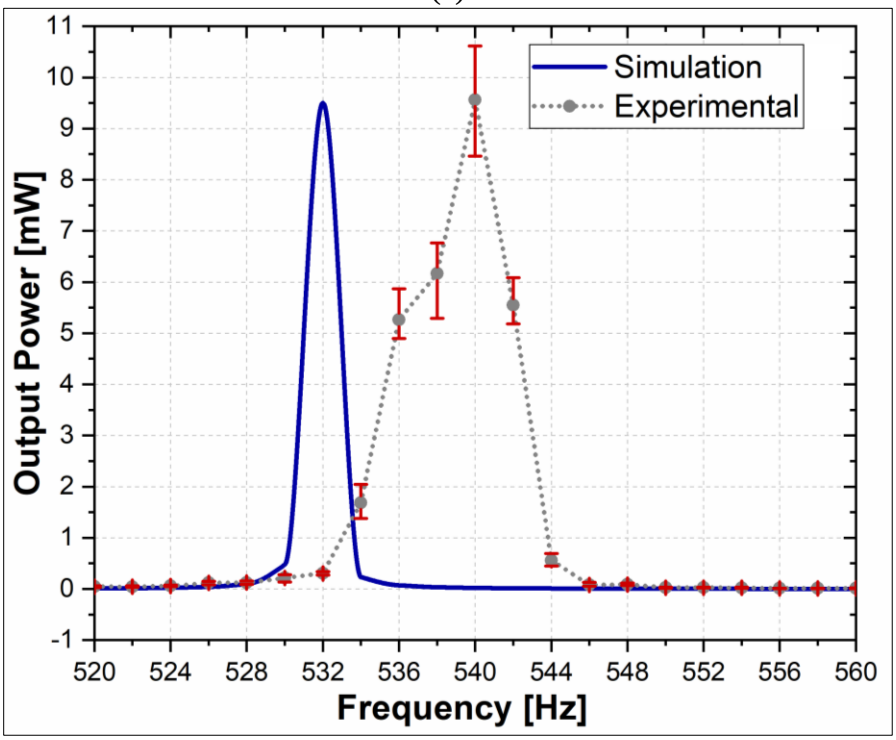

(b)

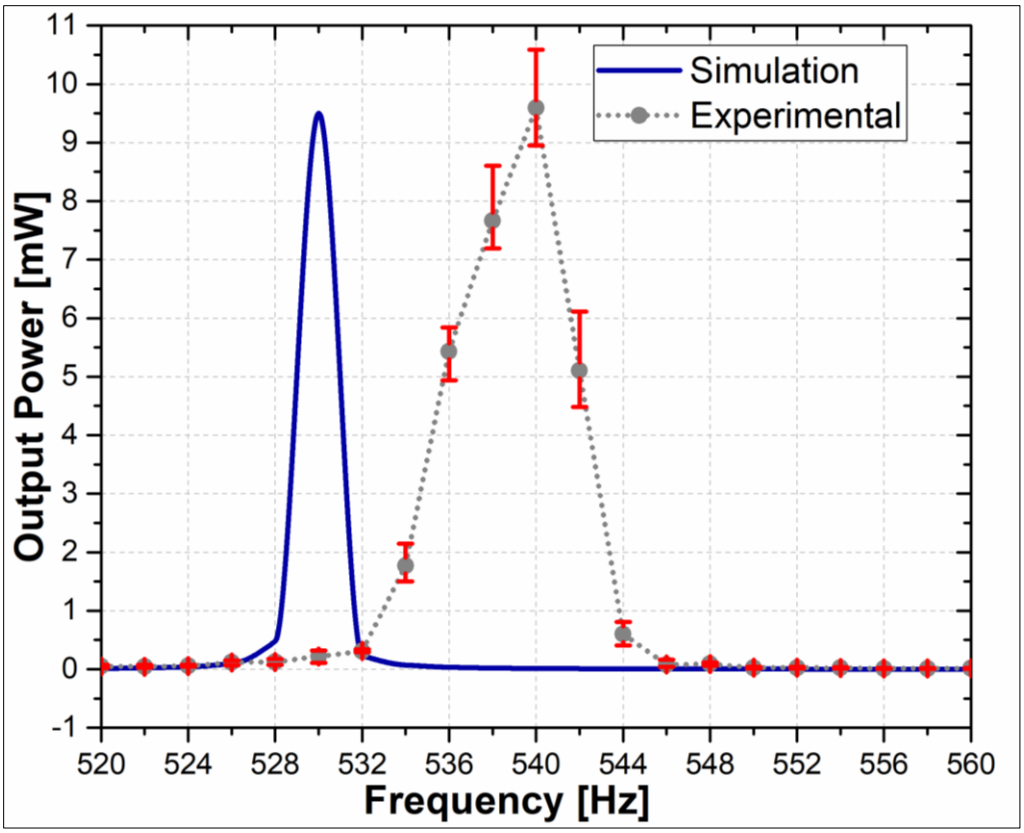

(c)

Figure 3.11: Simulation and experimental output power of the harvester cell during only (a) x-direction excitation, (b) y-direction excitation, and (c) z-direction excitation.

For the 3-D excitation, a recharging experiment was also performed using the energy harvester electronic board. A 40mAh Lithium-Polymer (LiPo) Ion battery with a nominal output of 3V was connected to the output of the board. Before the experiment, the battery was fully discharged to a level where its internal under-voltage protection shut down the output. We then charged the battery with a constant 20mA for about half an hour to drive the battery to an initial charging state.

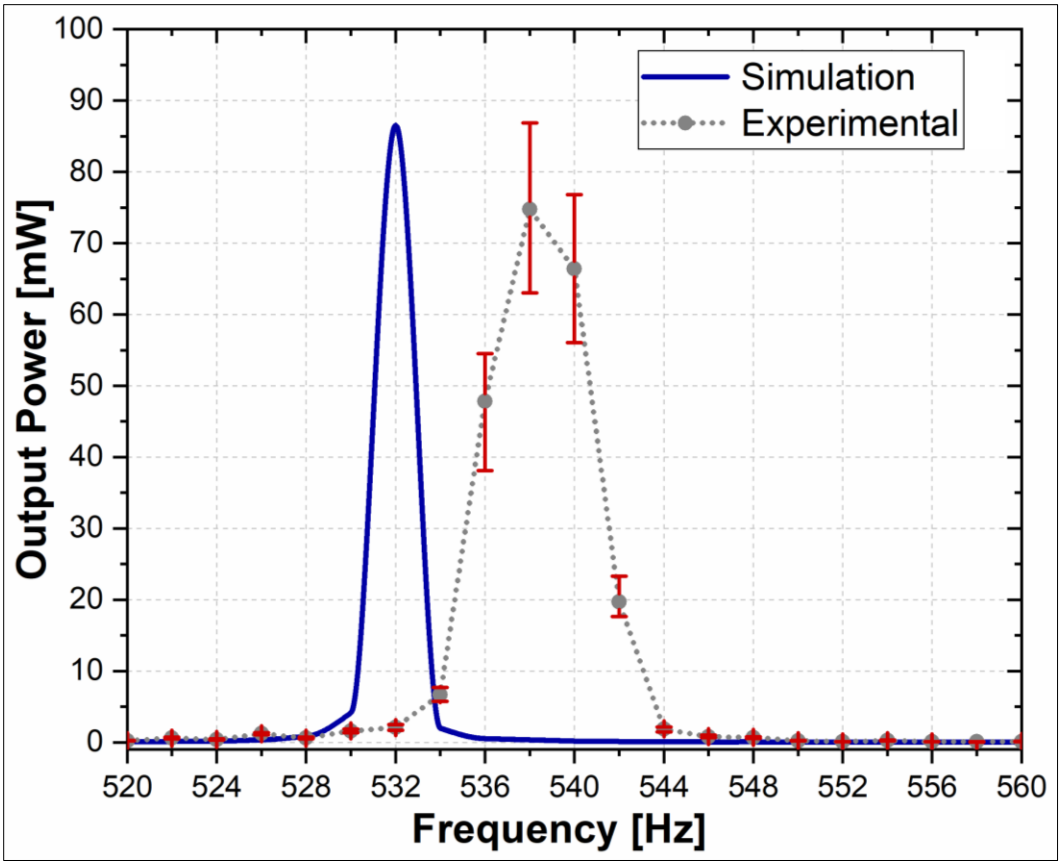

Figure 3.12: Simulation and experimental output power of the harvester cell during all 3-D vibration excitation.

At this point, the output terminal of the piezo elements was attached to the board input terminal while it underwent vibration at the resonance frequency. During the recharge process, the current flow to the battery terminal was monitored using digital multi-meter. This process continued for about 2 hours until AEVE 3D's shakers began to experience overheating. During the recharge process, a relatively constant 1.8 mA current was observed flowing into the LiPo battery [99-101].

3.6 **Chapter Conclusion**

In this study, a multi-axial vibration-based energy harvester was designed and fabricated using a Phononic Crystal metamaterial structure to scavenge energy from

low-frequency ambient vibrations. The structure was first conceived based on a band-stop acoustic filter technique and using a mass-in-mass structure with constituents of different material properties. It was hypothesized that at the resonance frequencies, the wave energy, entrapped within the rubber matrix as strain energy, can be converted to electric power using three strategically embedded piezoelectric wafers inside the cell. The proposed structure was then analytically modeled and simulated using COMSOL Multiphysics software. Upon analytical and numerical analyses, a prototype model was custom fabricated in house through an optimized process. Subsequently, the developed PC cell underwent a variety of low-frequency uni- and multi-directional vibration excitations, while the output potential was utilized to drive a resistive load. The simulation and experimental results were in close agreement.

The proposed energy harvester unit can be used to capture energy from ambient everyday vibrations which otherwise would be left abandoned and unused. An interesting application of this cell may be in the construction of household and industrial buildings in order to not only scavenge energy but to also attenuate ambient acoustic noise. In future studies, we will investigate such a possibility as well as development of broadband acoustic filters/energy harvesters capable of covering a wider frequency band.

CHAPTER 4:

HIGH VOLTAGE SINGLE AND MULTI-FREQUENCY ENERGY HARVESTING

4.1 Abstract

In the current study, a novel multi-frequency, vibration-based Energy Harvester (EH) is proposed, numerically verified, and experimentally validated. The structural design of the proposed EH is inspired from an inner-ear, snail-shaped structure. In the past decade, scavenging power from environmental sources of vibration has attracted a lot of researchers to the field of energy harvesting. High demands for cleaner and renewable energy sources, limited sources of electrical energy, high depletion rates of nonrenewable sources of energy, and environmental concerns have urged researchers to investigate new structures called Metamaterial energy harvesters to harness electrical potential. The proposed EH is a metamaterial structure which has a Polyvinylidene Difluoride (PVDF) structure incapsulated in an aluminum frame and follows the physics of a mass-in-mass Phononic crystal structure. The PVDF snail-shaped structure is encapsulated inside a silicone matrix with a specific material property. This EH reacts to the environmental vibrations and the encapsulating silicone entraps the kinetic energy within its structure. The EH unit cell behaves as a negative mass in the vicinity of its resonance frequencies. In this paper, the dynamic behavior of the proposed EH is numerically modeled in COMSOL

Multiphysics and, subsequently, validated experimentally using a unit cell fabricated in-house.

4.2 Introduction

The consumption of electrical energy will increase significantly to more than double globally from 2008 through 2035 [89]. The dramatic increase in the consumption of various forms of energy over the past decades has urged to search for alternative sources of power such as ambient energy harvesting systems [4, 89]. Low-power energy harvesters (EH) are being designed which are capable of harvesting energy from ambient sources. Research interests are increasing in this field and many endeavors on this topic can be found in the previous literature [6, 7].

Beeby et al. [33] reviewed the literature on electrical energy scavengers and harvesters for smart structures such as wireless microsystems and EH sensors, and concluded that among all these systems, the majority are spring-mass systems with three categories of transduction mechanical structures: piezoelectric mechanisms, electromagnetic-based solutions, and electrostatic-based structures [33]. Since 2002, by increasing the interest in energy harvesting, smart structures based on piezoelectric transduction mechanisms have attracted a lot of interest in the sensors industry. Our recent review paper on this topic demonstrates the increased applications of low-power gadgets, MEMS devices, actuators, and harvester sensors [88]. The main challenge in this field of research is to increase the amount of power scavenged using the developed energy harvesters. Many investigations have aimed to capture higher amounts of ambient energy via electromagnetic harvesters with closed-magnetic circuit. Although the electromagnetic harvesters have higher

efficiency compared to other harvesters, their harvested electrical power is still in the range of microwatts (μW).

Most piezoelectric-based energy harvesters employ a cantilever-beam harvesting mechanism. The electrical power harvested from these mechanisms is in the range of microwatts as well. Hence, they are suitable for applications with low-energy consumptions, such as low-power electronics and low-ampere battery chargers [104]. In our most recent review paper on EH mechanisms, the increased applications of energy harvesters for low-power devices, such as smart phones, GPS systems, wrist-band gadgets, and MEMS devices have been reported [59].

When the active piezoelectric material inside an EH cell is mechanically stressed, an electric power is generated and captured by means of an electric harvester circuit. The majority of such harvesters are fashioned as cantilever beams incorporating piezoelectric materials [62]. Capturing electric potential from low-frequency vibrations by means of cantilever-based mechanisms is difficult since the output charge quickly decays with the reduction of vibration frequency. The structural and geometric principles of such EHs working based on cantilever beams do not easily translate to low-frequency vibration domain as they would need humongous cantilever beam dimensions in low frequencies. Harvesting energy from low-frequency ambient vibrations is appealing due to the abundance of such vibration sources. Traditionally, researchers utilize conventional materials for EH devices. However, these materials do not possess the ability to respond to different vibrations across a wide range of frequencies. To mitigate problems associated with low-frequency vibration-based EH devices, piezoelectric-based metamaterial-inspired devices have been proposed. Metamaterials are artificial materials engineered to

have properties that have not yet been found in nature [53]. Acoustic metamaterials are typically used for controlling and guiding acoustic waves and vibrations, and obey the laws of negative refractive index materials, obtained via the modification of the mass density and bulk modulus. A negative modulus may cause an element to expand while under compression. Similarly, a medium with a negative mass may accelerate in the opposite direction of an applied force at particular frequencies [3]. Such metamaterials act like stop-band filters for vibrational waves by trapping them inside their constituents as strain energy. Therefore, it has been suggested to capture and transform this kinetic energy to electric potential with the introduction of active materials capable of electromechanical transduction.

Metamaterials possess an important property referred to as negative index [4], which has opened new avenues for energy harvesting with higher efficiencies [89] such as Phononic Crystal-based metamaterial introduced recently [6]. Phononic crystals (PCs) have embedded cavitis in their structure, which entrap acoustic energy at certain resonance frequencies depending on the material properties of the cell constituents. This trapped acoustic energy can be harvested using smart materials such as Polyvinylidene Difluoride (PVDF). Gonella et al. first introduced the concept of simultaneous wave filtering [105], which is possible due to low transmissibility of PC cells at certain frequency ranges. As a result, low-frequency stop-band filters can be designed. In a PC cell, it is possible to recover the trapped strain energy in a soft cell constituent using embedded piezoelectric wafers. Maximum power can be harvested at the resonance frequency when the piezoelectric wafer is strained at its maximum caused by an embedded resonator. A recent study demonstrates

that by using multiple piezoelectric elements inside metamaterial cells, it is possible to capture trapped energy in milliwatt range (mW) [6].

In this Chapter, we propose a novel energy harvester which is comprised of a snail-shaped piezoelectric element incorporated inside a soft silicone encapsulant and placed inside a metallic frame. This harvester is capable of capturing electrical potential at multiple frequencies using only a single unit cell. The proposed EH, furthermore, can harvest energy in a variety of vibration environments with the same base structure.

4.3 Design considerations and Modeling

In this section, the model structure and the components utilized in this proposed metamaterial vibration-based energy harvester cell are described.

4.3.1 Structural Design of Phononic Crystal Unit Cell

In the last decade, several metamaterial structures have been proposed for the purpose of electrical energy scavenging. These metamaterial devices are called Phononic Crystals (PCs) which are categorized based on their capabilities of entrapping vibrational energy in their structural components. In this study, a metamaterial PC, inspired from the shape of a snail shell, with the capability of harvesting electrical potential at different low-frequency vibrations (<1000Hz) is proposed. The proposed model is capable of targeting different range of frequencies by changing the material properties, as well as the geometry configurations. Phononic crystals are generally modelled based on a mass-in-mass configuration. In a PC cell with a specific geometric structure, a negative effective dynamic mass occurs at the resonance frequencies [6], at which wave energy is trapped inside the PC cell's soft constituents as dynamic strain energy.

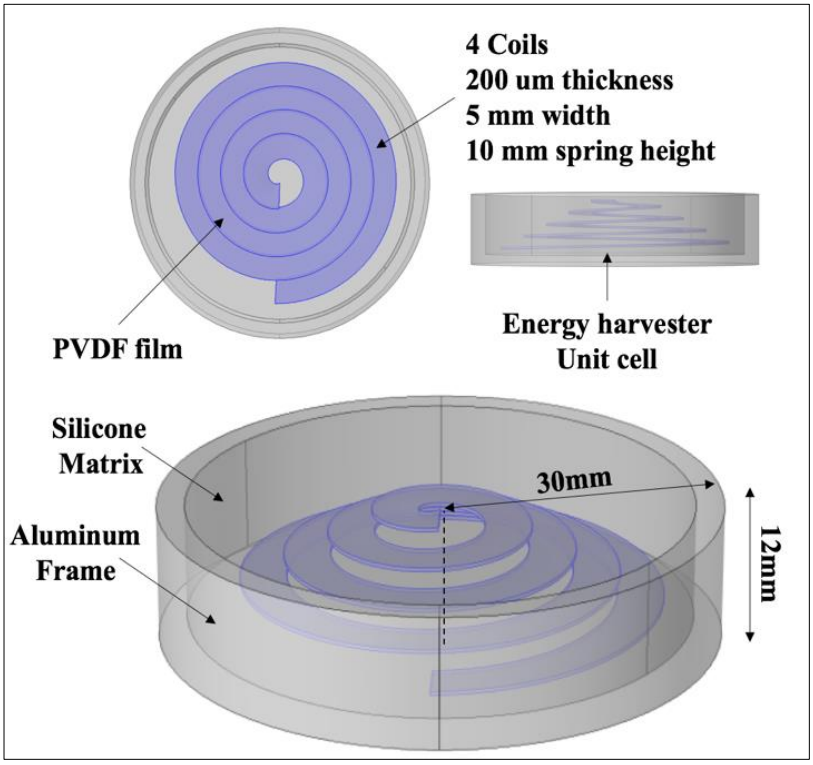

Figure 4.1: The CAD design of the proposed energy harvester configuration and placement of the polyvinylidene difluoride in aluminum frame.

The metamaterial-based PC, presented here as an energy harvester unit, comprises of a hollow, 2mm-thick cylindrical aluminum frame as a housing, which encapsulates a silicone-piezoelectric structure inside itself. This silicone-piezoelectric structure consists of a PFDF film and a specific mixture of tin-cure silicone rubber. Figure 4.1 demonstrates the CAD model of the proposed cell. In this proposed EH cell, PVDF fashioned as a snail shell configuration is strategically surrounded in a smooth tin-cure silicone rubber with desired material properties. The overall dimensions of the PVDF element and the cylindrical silicone rubber are presented in figure 4.1.

Table 4.1: Material properties

Material	Density (kg/m^3)	Modulus of elasticity (Pa)	Poisson's Ratio
PVDF	1780	$2.8e^9$	0.18
Silicone	970	$99e^5$	0.49
Aluminum	2700	$6.89e^{10}$	0.33

4.3.2 Numerical Analysis of the Phononic Crystal Unit Cell

In this study, a numerical modeling using finite-element analysis (FEA) in the COMSOL Multiphysics software is performed with the intention to verify the proposed metamaterial-inspired vibration-based EH cell's behavior in response to vibrational excitations. In simulations, the PC cell was analyzed in (i) eigenfrequency domain and (ii) piezoelectric device environment to obtain the available resonance frequencies. During the analysis, the surface of the PVDF film was kept perpendicular to the excitation direction which is considered vertical (i.e., in z-axis) in this case. Table 4.1 summarizes the material properties used for the purpose of numerical analysis.

After performing the eigenfrequency analysis, several resonance frequencies were found. Figure 4.2 displays the eigenfrequency responses of the proposed design's constituents at different eigenfrequencies. For the proposed design, resonance frequencies of 190.55 Hz, 196.27 Hz, 196.57 Hz, 278.64 Hz, and 280.41 Hz are found from numerical analysis. In the proposed EH, based on the properties and dimensions of the materials used, the resonance frequencies vary. At the resonance frequencies, the kinetic energy is entrapped within the soft rubber and, the PVDF material is polarized along its surface, and,

consequently, the PVDF material experiences maximum harmonic compressive strain perpendicular to its surface [7, 106].

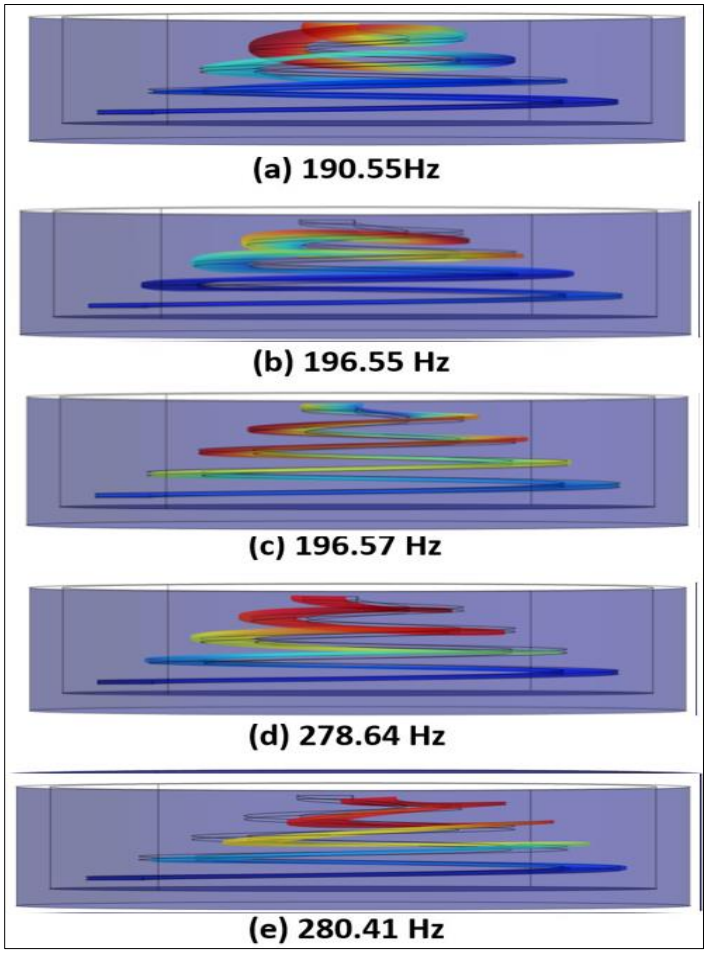

Figure 4.2: Displacement plot of the proposed harvester cell at different resonance frequencies. (a) 190.55 Hz, (b) 196.27 Hz, (c) 196.57 Hz, (d) 278.64 Hz, and (e) 280.41 Hz.

The displacement plot is depicted from a side view at different resonance frequencies in Figure 4.2. This figure shows the maximum displacement of the PVDF film at different resonance frequencies. This maximum strain energy induces maximum displacement in the PVDF element, thereby generating maximum electrical potential.

It is noteworthy that the resonance frequencies, and the corresponding band gaps, can be changed to target different resonance frequencies by altering the proposed model's dimensions (e.g., aluminum frame, PVDF film), as well as material properties (e.g., silicone matrix). Furthermore, weakly-dispersed band gaps are created due to local resonance in the silicone matrix.

4.3.3 Structural Design of a Meta-tile from Phononic Crystal Unit Cells

In this section, a rectangular array of the proposed unit cell in the previous section is designed and placed in an Aluminum frame filled with PDMS material, figure 4.3. The main purpose of this design is to harvest energy in higher range in a range of frequency.

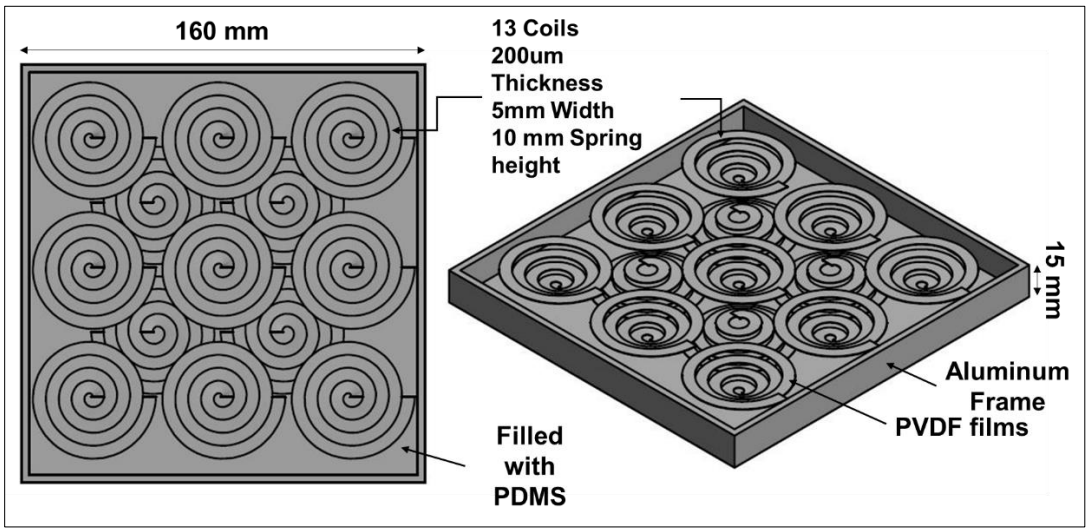

Figure 4.3: The CAD design of the proposed Meta-tile energy harvester configuration and placement of the 13 polyvinylidene difluoride films in aluminum frame.

In this section, a metamaterial PC, inspired from the shape of a snail shell, with the capability of harvesting electrical potential at different low-frequency vibrations (<1000Hz) is placed in a novel design to target a wide range of frequencies. The proposed model is capable of targeting different range of frequencies by changing the material properties, as well as the geometry configurations. Phononic crystals are generally

modelled based on a mass-in-mass configuration. In a PC cell with a specific geometric structure, a negative effective dynamic mass occurs at the resonance frequencies, at which wave energy is trapped inside the PC cell's soft constituents as dynamic strain energy.

4.3.4 Numerical Analysis of the Meta-tile from Phononic Crystal Unit Cells

In this part, a numerical modeling using finite-element analysis (FEA) in the COMSOL Multiphysics software is performed with the intention to verify the proposed Meta-tile energy harvester's performance in response to vibrational excitations. In simulations, the Meta-tile was analyzed in (i) eigenfrequency domain and (ii) piezoelectric device environment to obtain the available resonance frequencies. During the analysis, all the surface of the PVDF films embedded in PDMS were kept perpendicular to the excitation direction which is considered vertical (i.e., in z-axis) in this case. Table 4.2 summarizes the material properties used for the purpose of numerical analysis.

Table 4.2: Material properties

Material	Density (kg/m^3)	Modulus of elasticity (Pa)	Poisson's Ratio
PVDF	1780	$2.8e^9$	0.18
PDMS	956	$5.7e^5$	0.49
Aluminum	2700	$6.89e^{10}$	0.33

After performing the eigenfrequency analysis, several very close resonance frequencies were found. Figure 4.2 displays the eigenfrequency responses of the proposed design's constituents at different eigenfrequencies. Numerical analysis shows that there are more than 50 resonance frequencies for this proposed Meta-tile in the range of 117Hz to 210 Hz.

For the proposed Meta-tile design, resonance frequencies are 117.24 Hz, 117.99 Hz, 117.01.57 Hz, 132.13 Hz, 132.97 Hz, 133.45 Hz, 136.84 Hz, 141.4 Hz, 144.05 Hz, 146.66 Hz, 148.63 Hz, 148.71 Hz, 149.12 Hz, 155.58 Hz, … and to 210.33 Hz. In the proposed Meta-tile, based on the properties and dimensions of the materials used, the resonance frequencies vary. At the resonance frequencies, the kinetic energy is entrapped within the soft PDMS and, the PVDF material is polarized along its surface, and, consequently, the PVDF material experiences maximum harmonic compressive strain perpendicular to its surface. The displacement plot is depicted in Figure 4.4 from the orthographic view of the Meta-tile energy harvester at some of the above-mentioned different resonance frequencies.

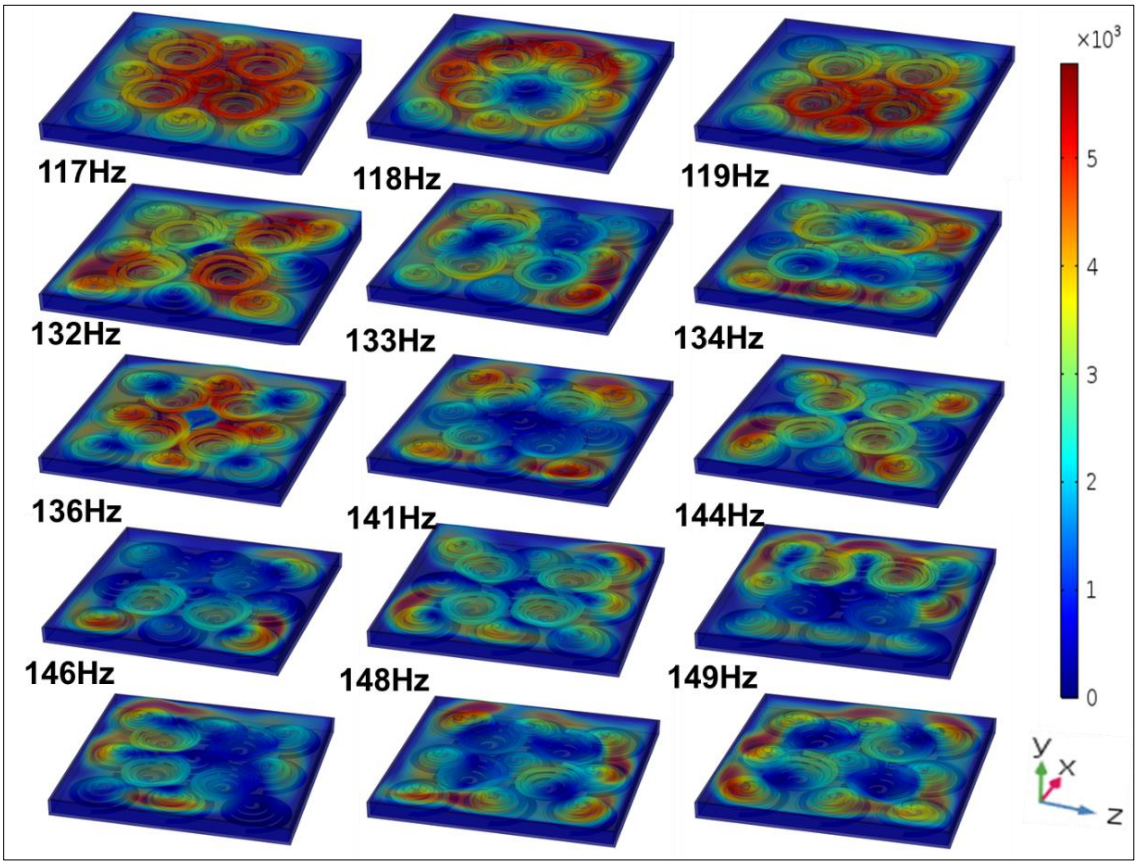

Figure 4.4: Displacement plot of the proposed Meta-tile Energy harvester at the first 15 different resonance frequencies.

This figure shows the maximum displacement of the PVDF films at different resonance frequencies. This maximum strain energy induces maximum displacement in the PVDF element, thereby generating maximum electrical potential.

4.4 Experimental Validation and Testing

In this section, the fabrication procedure of the proposed EH cell and description of the vibration exciter testbed and the experimental setup are provided.

4.4.1 Fabrication of the Energy Harvester Unit Cell and the Meta-tile

In this subsection, we aim to experimentally validate the numerical analysis provided in the previous sections. Figure 4.5 shows the final fabricated unit of the EH cell which was custom made in Integrated Material Assessment & Predictive Simulation (iMAPS) lab. In the first step, for the fabrication of the Energy harvester unit cell, the cylindrical silicone matrix containing the PVDF and the required wiring and circuitry are fabricated. For this purpose, aluminum frame was machined based on the desired dimensions using a lathe machine and a milling machine. The inner diameter of the aluminum frame was precisely machined and polished to be at 60mm with tolerance of ~ ±0.05mm. The height of the frame was also precisely finished to be at 10mm. The thickness of the frame is set to be at 2mm. Another aluminum circular lid was fabricated to be used as a cap to cover the bottom side of the energy harvester aluminum frame. Accurate machining of the frame is essential in having accurate experimental data closely following the numerical analysis.

In the next step, a PVDF film was accurately laser-cut following the spiral CAD model via a single spot laser cutter which is an opto-mechanical system for cutting sensitive materials with extreme precision and small feature sizes (in μm scale). Upon assembly of

the aluminum frame parts, the PVDF was accurately stretched to its intended dimension and placed in the middle of the aluminum frame. Subsequently, liquid silicone rubber (Mold Star 20T) was poured in the frame and left aside for 30 minutes to cure in room temperature. In the meantime, the surface of the liquid silicone was kept flat by placing a flat glass plate on the aluminum frame. This process and the corresponding timing were developed after a few trials in order for the silicone rubber parts to have a seamless and homogenous bond. After having the silicone matrix entirely cured, the final dimensions and weight of the unit cell were measured to follow the exact considered material properties in numerical analysis.

Eventually, for the fabrication of the Meta-tile energy harvester, 13 number of PVDF films were accurately laser-cut following the spiral CAD model via a single spot laser cutter which is an opto-mechanical system for cutting sensitive materials with extreme precision and small feature sizes (in μm scale). All the 13 coils were placed in a cubic aluminum structure based on the proposed CAD design. Right after mounting the coils in the Aluminum frame, the PVDF films were accurately stretched to its intended dimension and placed across the aluminum frame, Figure 4.5. Subsequently, PDMS liquid was poured in the Aluminum frame and left in oven for 80 minutes to fully cure in 78 °C temperature. In the meantime, the surface of the PDMS was kept flat by placing a flat glass plate on the aluminum frame. This process and the corresponding timing were developed after a few trials in order for the PDMS parts to have a seamless and homogenous bond.

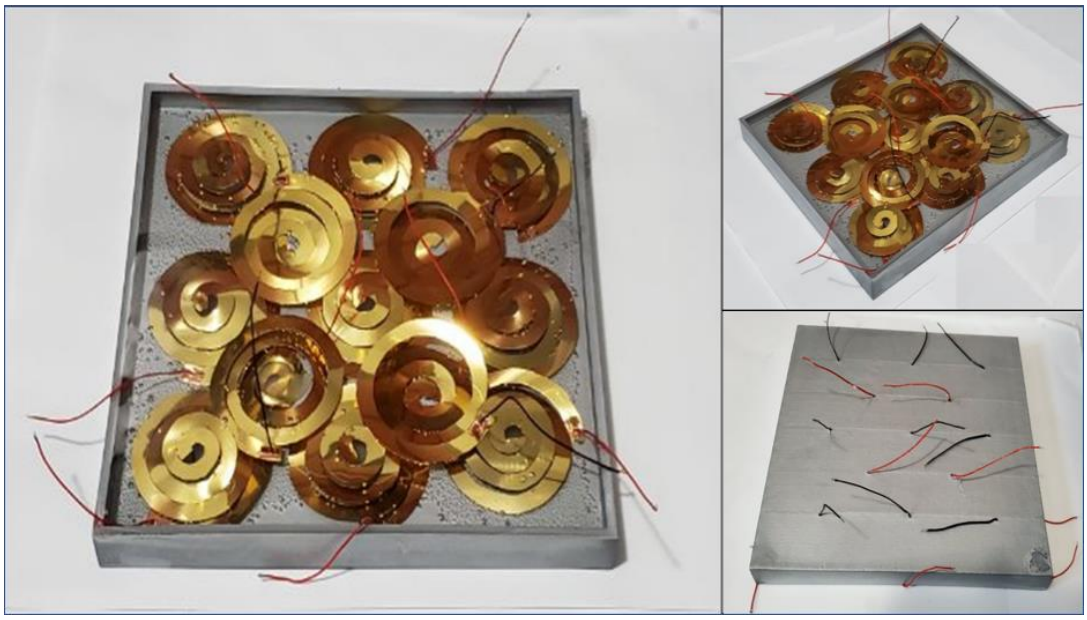

Figure 4.5: The Final Fabricated unit of the EH Meta-tile which was custom made in Integrated Material Assessment & Predictive Simulation (iMAPS) lab.

4.4.2 Vibration Exciter Testbed and Experimental Validation

In order to validate the functionality and performance of the fabricated EH cell, a precise vibration exciter testbed was utilized. In iMAPS laboratory, we have designed and fabricated an Acousto-Electrodynamic Vibration Exciter testbed, referred to as AEVE 3D, Figure 4.6a. This vibration exciter works in a wide range of frequencies and is capable of applying constant force and constant acceleration. AEVE 3D is capable of providing coupled/uncoupled vibrations in a wide frequency range in the forms of acoustic or mechanical excitations using three perpendicular mechanical shakers and three perpendicular loud speakers [87, 107]. AEVE 3D's actuators are electrically synchronized and assembled in three Cartesian directions. The desired sinusoidal signals with desired frequencies are generated and separately fed to each actuator. In this study, only the mechanical excitation portion of the machine is utilized to perform the experiments. Figure 4.6b demonstrates the placement of the fabricated energy harvester unit cell and at the heart

of the AEVE 3D. The constructed EH unit cell was firmly fixated inside AEVE 3D so that the direction of the excitation is perpendicular to the surface of the PVDF element.

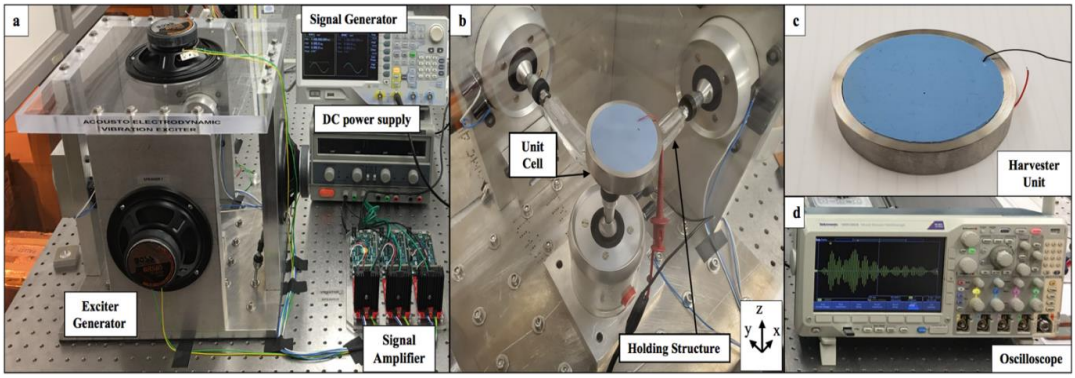

Figure 4.6: (a) Experimental setup including AEVE 3-D machine, function generator, signal and amplifier, (b) the placement of the unit cell inside the AEVE 3-D machine, (c) the fabricated unit cell, (d) oscilloscope to sense the generated electric potential.

4.5 Experimental Validation and Testing

The precise model of the proposed EH cell (i.e., using the measured parameters of the fabricated model such as weight) was simulated in COMSOL Multiphysics to investigate the harvester's power output in a wide range of frequencies containing resonance frequencies in (i) frequency domain and (ii) piezoelectric device environment. A displacement oscillation load was applied to the bottom of the model, along the axis perpendicular to the surface of the PVDF element, in order to understand the oscillation patterns of the EH cell. At frequencies in the vicinity of resonance, the unit cell behaves like a medium with a negative effective dynamic mass due to special decay of wave amplitude as reported in the stablished literature [7].

During the experimentations for the unit cell energy harvesting, AEVE 3D's sinusoidal signals' frequencies ranged from 180 Hz to 300 Hz, evenly distributed at every 1 Hz. The amplified signals were fed to the corresponding axis of the machine with. Concurrently,

the output voltage of the EH cell was accurately recorded against a 10kΩ resistive load, which was then used to calculate the instantaneous power. Each excitation experiment was repeated 20 times. This 10kΩ resistor was also added to the numerical study with the purpose of having the same scenario for both experimental and numerical studies. Numerical results are presented in figure 4.7. According to this figure, exactly at 5 different resonance frequencies of the proposed energy harvester cell, we have the maximum output power which are at 190.55 Hz, 196.27 Hz, 196.57 Hz, 278.64 Hz, and 280.41 Hz. The numerical and experimental analyzing of the proposed EH show that the cell has the maximum electrical power of ~ 1mW at its resonance frequencies.

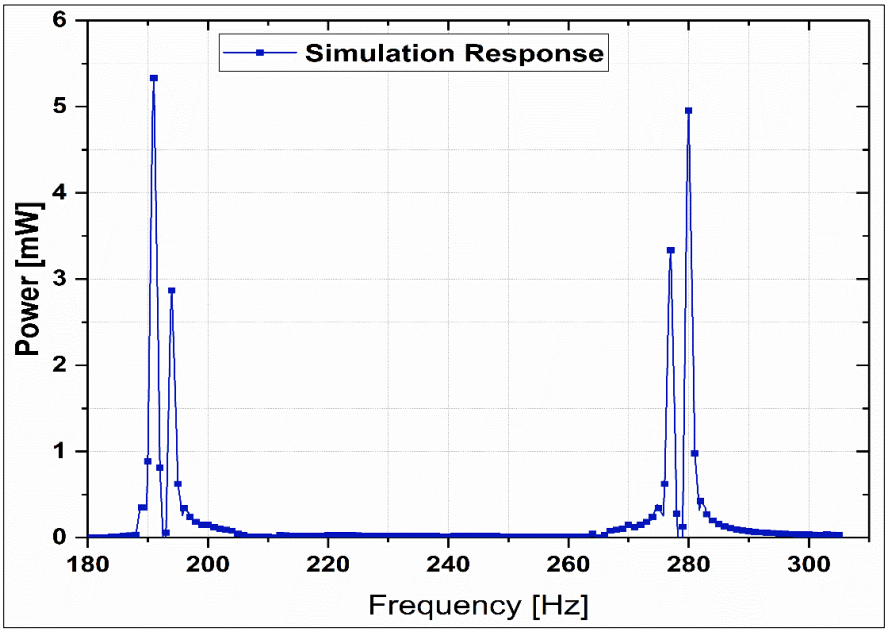

Figure 4.7: Numerical output power of the harvester cell against a 10kΩ load.

The maximum output power during experimentations also occurs at resonance frequencies which are identical to frequencies obtained in the numerical analysis. The experimentally obtained power output is presented in Figure 4.8. Although the experimental and the numerical results are in very close agreement, there is still a negligible discrepancy between FEA and experimental results, which can be attributed to a variety of

factors, such as human error, fabrication tolerance, mismatches in the material properties, imperfections in the placement and tilt of the PVDF element, ambient temperature, and imperfect adhesion between layers.

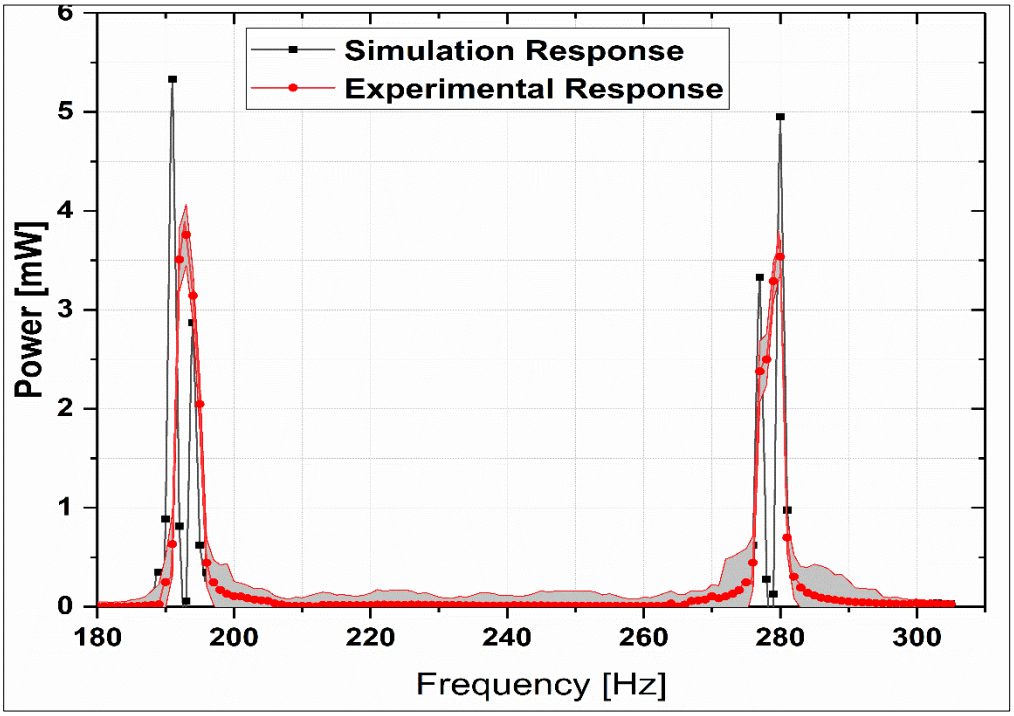

Figure 4.8: Experimental output power of the harvester cell against a 10kΩ load.

During the experimentations for the Meta-tile, AEVE 3D's sinusoidal signals' frequencies ranged from 110 Hz to 210 Hz, evenly distributed at every 1 Hz. And similar to the previous experiments for the unit cell, the amplified signals were fed to the corresponding axis of the machine. Concurrently, the output voltage of the EH cell was accurately recorded against a 10kΩ resistive load, which was then used to calculate the instantaneous power. Each excitation experiment was repeated for 20 times to achieve the most accurate results. This 10kΩ resistor was also added to the numerical study with the purpose of having the same scenario for both experimental and numerical studies.

Numerical results for the Meta-tile energy harvester are presented in figure 4.9. According to this figure, from a band of frequency of ~ 110 Hz to 210 Hz, we have the maximum output power which is ~ 11 mW.

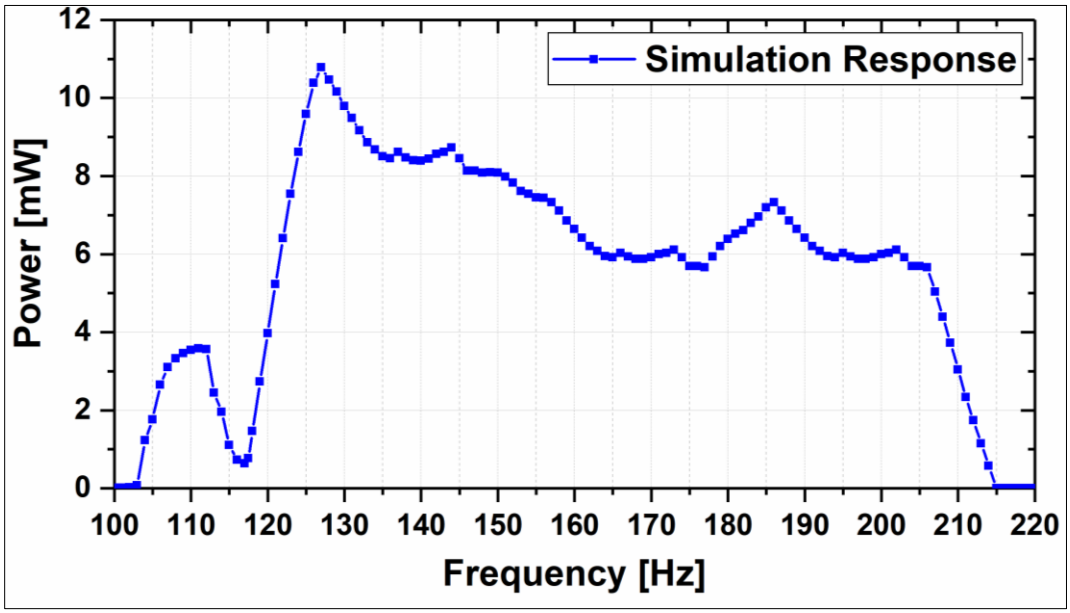

Figure 4.9: Numerical output power of the Meta-tile harvester against a 10kΩ load.

The maximum output power during experimentations for the Meta-tile also occurs at this range of frequencies which are identical to the range of frequencies obtained from the numerical analysis. The experimentally obtained power output is presented in Figure 4.10. Although the experimental and the numerical results are in very close agreement, there is still a negligible discrepancy between FEA and experimental results, which can be attributed to a variety of factors, such as human error, fabrication tolerance, mismatches in the material properties, imperfections in the placement and tilt of the PVDF element, ambient temperature, and imperfect adhesion between layers.

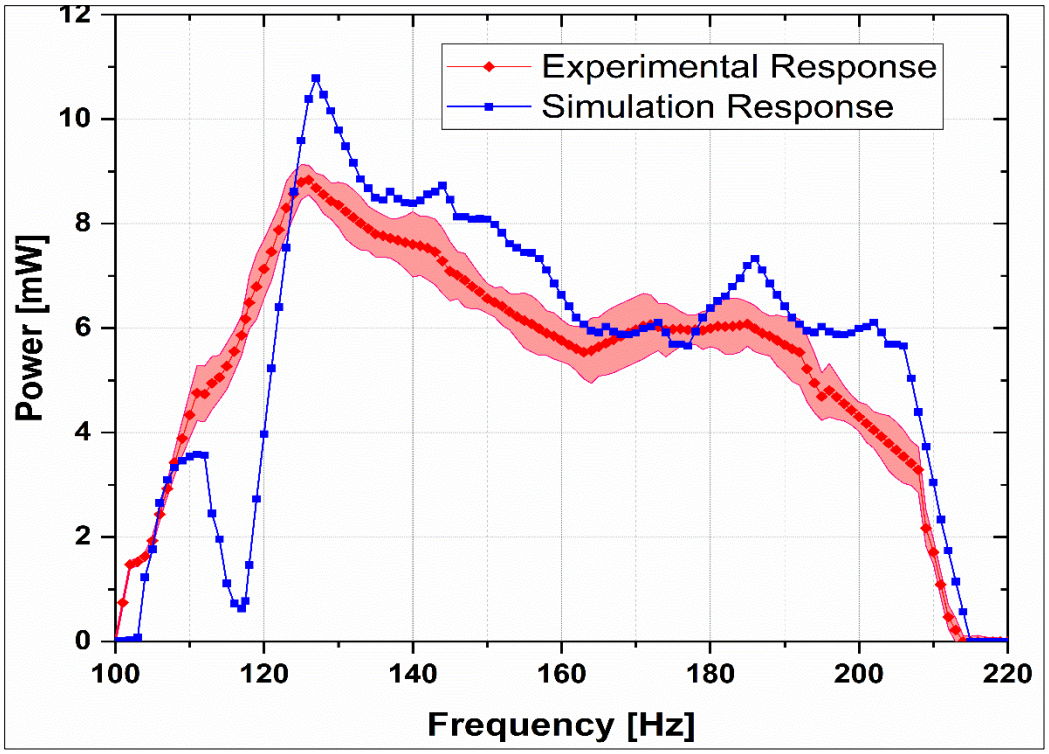

Figure 4.10: Experimental output power of the harvester cell against a 10kΩ load.

4.6 **Chapter Conclusion**

In this chapter, a novel multi-frequency vibration-based energy harvester (EH) unit cell and a Meta-tile energy harvester were proposed, numerically verified, and experimentally validated. The design of the EH unit cell and the Meta-tile were inspired from an inner-ear snail-shaped structure. The proposed EHs are metamaterial structures with PVDF structures covered inside a silicone matrix or PDMS material and encapsulated in an aluminum frame. These EHs react to the environmental vibrations and the embedded silicone/PDMS entrap the kinetic energy within its structure. The whole EH structures behave as a negative mass in the vicinity of resonance frequencies. The behaviors of the proposed EHs were numerically modeled in COMSOL Multiphysics, and the proof of concept of the proposed structures were fabricated and experimentally validated. The

numerical and experimental analyzing of the proposed EHs show that the structures have the maximum electrical power of ~ 1mW for the unit cell and ~11 mW for the Meta-tile at single and multiple resonance frequencies.

CHAPTER 5:

BIO-INSPIRED META-MATERIAL SINGLE OR DISTINCT BANDPASS ACOUSTIC SENSOR

5.1 Abstract

In this chapter, inspired from the human cochlea, two artificial basilar membrane structures based on an array of gold electrodes microfabricated along the opposite surfaces of a piezoelectric continuum (Plate type) and Zinc oxide piezoelectric microfabricated on a 10 μm silicone rubber membrane (Beam type) are proposed. For the plate type acoustic sensor, the proposed piezoelectric continuum features an isosceles trapezoidal geometry and is situated atop an elastomer matrix with embedded electrode grooves and a duct. At first, a detailed analytical model is presented, which formulates the continuum's planar deflection equation, governing its elastodynamic behavior. Subsequently, in order to verify the analytical outcomes, a Multiphysics finite element analysis is performed in COMSOL® software. Both analytical and numerical models demonstrate desired frequency selectivity and mapping of a biological basilar membrane. Subsequently, a proof of- concept model of the proposed structure is custom-fabricated through standard photo- and soft lithography techniques using Polyvinylidene Difluoride (PVDF), Gold, and Polydimethylsiloxane (PDMS) materials. Finally, the fabricated artificial basilar membrane is experimentally characterized using a custom-built acoustic exciter, and its effective performance is validated in the frequency range of 3 kHz to above 8 kHz from Apex to Base sides. For the

proposed beam type acoustic sensor, similar to the plate type, a trapezoidal geometry is adopted. Here, proposed continuum features a 10- μm thick isosceles trapezoidal geometry out of silicone material and is situated atop an elastomer matrix with embedded electrode grooves and a duct. Unlike the plate type concept in which the continuum is the piezoelectric material (PVDF), in the beam type concept, the electrodes themselves are the piezoelectric materials (ZnO) which are sandwiched in between to silicone membranes. The design is in such a way that there are 100 electrodes along the 100 mm continuum and length and the thickness of each electrode varies linearly along the length of the trapezoidal continuum. Hence, the first electrode which is near the apex side has 8 mm length, 300 μm width and 20 μm thickness and the last electrode near the base has 3 mm length, 300 μm width and 110 μm thickness. Eventually, its effective performance of the beam type acoustic sensor verified in the frequency range of ~ 0.5 kHz near Apex side to ~ 20 kHz near Base side.

5.2 **Introduction**

Sensor technology is a rapidly growing area of interest in science and product design, embracing developments in electronics, photonics, mechanics, chemistry, and biology. Ultrasound, non-contact radar, optoelectronic sensor solutions and laser technologies are among the current trends in the sensing technology industry. Acoustic sensors cover a large area of the sensor technology due to their wide application in many engineering domains. Their presence is widespread in everyday life, where they are used to sense sound and vibration excitations. Acoustic sensors are used for indoors and outdoors in the harshest conditions, for a variety of applications such as automotive industry, sonar systems, micro-mechanical devices, manufacturing instrumentation, 3D printing, micro-electronic devices,

and in many chemical and biological smart structures. Acoustic sensors are highly demanded in the aforementioned domains with the rapid advancement of the technologies that leads to the complex measurements and operations with a high level of accuracy. The consumer-driven market demands these sophisticated sensors with high quality standards as well as uncompromised reliability.

Acoustic sensors can be classified into two categories of (i) distinct single frequency sensors, where a unique frequency is of interest and the sensors are devised to only respond to acoustic stimuli with that single frequency, and (ii) bandpass sensors, where a desired frequency band is sensed and the rest of the frequencies are filtered out [1, 2]. A band is defined as the range of frequency where the energy transmission coefficient is very low and almost no energy can pass through the structure [3, 4]. Resonance phenomenon is the key point in acoustic sensors to select a specific frequency [6-8]. Due to the resonance principle, large-scale geometries are required for fabrication of acoustic sensors in low-frequency applications. Hence, a novel but universal frequency selection process is necessary which can be adopted for sensing almost any wide range of frequencies with controlled geometric configurations.

Traditionally, researchers utilize conventional materials for detecting acoustic waves. However, these materials do not possess the ability to respond to acoustic vibrations across a wide range of frequencies. Thus, to address this incapability, application of metamaterials has been proposed. Metamaterials are artificial materials engineered to have properties that have not yet been found in nature. They are assemblies of multiple individual elements produced from conventional materials, such as metals or plastics, which are typically constructed into repeating patterns [10-12]. It is well-established that in any acoustic

metamaterial structure, frequency band gaps are the results of either local resonance or Bragg scattering [13, 14]. Low-frequency sonic waves can be controlled by introducing locally resonant components into a unit metamaterial (known as sonic crystal) [15, 16], whereas conventionally high frequency stop bands can be formed by multiple scattering (Bragg) of the periodic inclusion of the sonic crystals [14, 17, 18]. Acoustic metamaterials offer a number of exceptional properties (e.g., negative bulk modulus, negative effective mass density) that are not achievable using natural materials.

Nature is the best source of ultimate scientific references. Hence, to advance the existing state-of-the-art knowledge, researchers are not only digging hard in their associated areas, but also taking inspiration from natural phenomena. A recent seminal study demonstrated that the human cochlea performs a bandpass filtration functionality where it senses only a specific frequency band (20 Hz to 20 KHz) and mechanically filters out all other frequencies. General description of the cochlea can be found in the works of Dallos [108], Evans [109], Kessel and Kardon [110], Miller [111], and Shepherd [112]. Sound waves travel down the external auditory meatus and, vibrate the eardrum. On the other side of the eardrum is the internal auditory meatus, which opens during swallowing to equalize pressure across the eardrum [113, 114]. Vibrations of the eardrum couple into the small bones, called the hammer or malleus [115]. Vibration of the malleus causes waves to travel in the cochlea [116-118]. Inside the cochlea, sound waves are propagated by a membrane, called basilar membrane [119]. Basilar membrane is the key component in sensing sonic frequencies and filtering out all other frequencies in the environment by means of varying stiffness of the membrane from the base end to apex end, which makes the cochlea the most advanced bandpass filter in nature [120, 121]. The cochlea is a highly

complex mechanical sensory system. The key functionality of cochlea is the spatial selectivity of the sonic frequencies [122]. Basilar membrane selects the sonic frequencies by naturally varying the mechanical properties from the basal to the apical ends [123]. The length of human's unrolled cochlea is about 35 to 40 mm long and about 2 mm in diameter [119], Figure 5.1. If the spiral cochlea structure could be unrolled, it would appear as a long fluid-filled tube, with a trapezoidal-shaped basilar membrane.

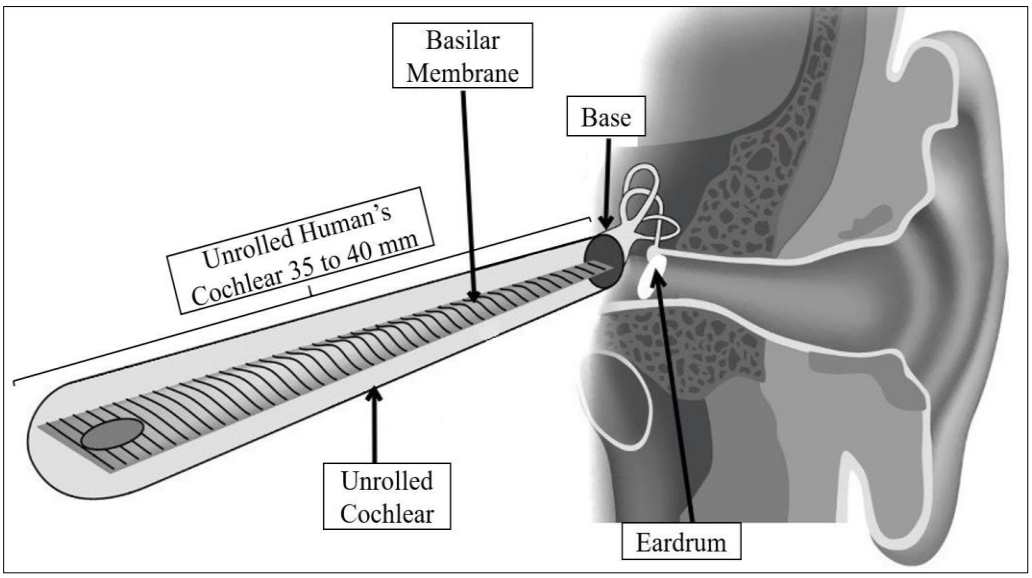

Figure 5.1: An Unrolled human's cochlear, simplified to emphasize trapezoidal shame and length of basilar membrane.

The basilar membrane is stiff and narrow near the basal end, and flexible and wide near the apical end, with a smooth logarithmic transition along its length. In a nutshell, in developing a bandpass frequency sensor, the basilar membrane performs four principal operations as: (1) produce local resonance, (2) sense desired frequency and filter out all other frequencies, (3) sense input frequency with a sensory medium and, (4) select frequency spatially.

In recent years, a notable number of attempts have been made to develop bandpass frequency sensors adopting the mechanics of basilar membranes [124-131]. For instance, Tanaka et al. [25] fabricated a fishbone-like structure from a thin Si plate as an equivalent mechanical model of the cochlea. A micro-cochlea model was presented by Witt Brodt et al. [132] using a thin polyimide plate as a basilar membrane. More recently, Shintaku et al. [133] proposed a microbeam array with variable thickness, and investigated its suitability for an acoustic sensor with a wide range of frequency selectivity. Tanujaya et al. [134] presented an artificial basilar membrane prototype to catch sinusoidal waves at various frequencies using a laser Doppler vibrometer. White and Grosh [135] constructed a micro-engineered hydromechanical cochlea that included a micro-machined membrane as well as a fluid-filled duct to mimic the cochlear chamber. However, the response frequencies detected by the acoustic input were above the audible frequency range. In a recent study, Kim et al. [124, 136] assessed the frequency selectivity of an artificial basilar membrane constructed using a piezoelectric beam array. Though a considerable number of studies have been concluded to model artificial mechanical cochlea, to the best of our knowledge, a true high-speed predictive model, an ultra-precise numerical model, and a fabricated metamaterial-based sensor have not been reported in the literature. In this study, we have modeled and fabricated a bandpass frequency sensor, inspired by the basilar membrane structure, that can detect sonic waves in the audible frequency range.

5.3 Plate Type Sensor Predictive Model and Analytical Formulation

Since it is established that the basilar membrane possesses the ability to select a specific frequency band, in this study, it is intended to develop a bandpass acoustic sensor

mimicking the basilar membrane structure. The basilar membrane, when unrolled, has a trapezoidal structure which is narrow at the base point and gradually becomes wider at the apex. The basilar membrane in the cochlear is fixated to boundary supports from all directions except at the apex side [108].

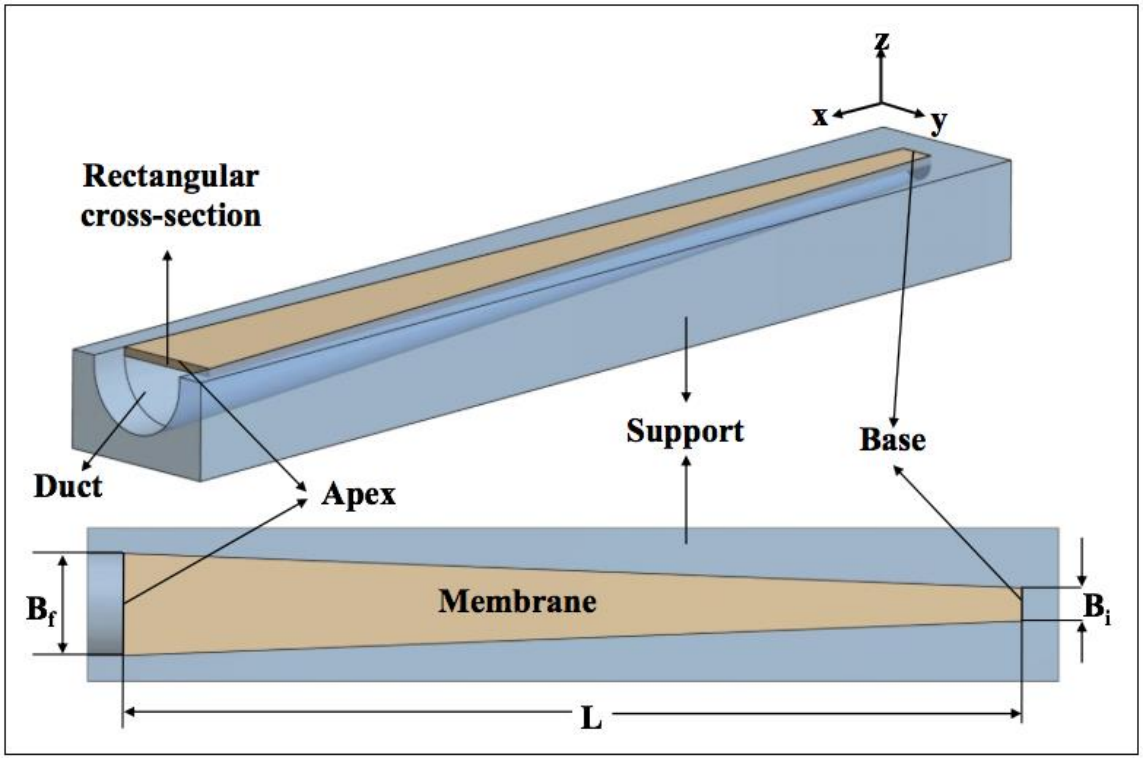

Figure 5.2: Proposed geometric configuration of the frequency band sensor mimicking a basilar membrane structure.

Following the basilar membrane structure, Figure 5.2, a trapezoidal domain is considered as the broadband sensing device in this study. The model parameters are defined in Table 5.1.

Considering the ABM geometry and boundary conditions, the model parameters that can be controlled are the continuum's Poisson ratio, Young's modulus of elasticity, density, thickness, and length of each side. The derivation procedure for elastodynamic equations

of the proposed ABM continuum governing its vibration behavior at a given (x, y) coordinate is shown below.

Table 5.1: Model parameters and notations

Symbol	Quantity
L	Basilar Membrane Length
B_i	Base Width
B_f	Apex Width
D	Bending Stiffness of the Membrane
P	Harmonic Pressure
E	Modulus of Elasticity
ρ	Density
ξ	Dynamic Deflection
h	Thickness of Membrane
ν	Poisson Ratio
ω	Excitation Frequency
u	u- Axis
v	v- Axis

Eqn. (5-1) formulates the bending stiffness, K, of a rectangular plate based on its modulus elasticity, E, thickness, h, and Poisson ratio, ν [137]. Mauritsson and colleagues [138, 139] derived a series of dynamic plate equations based on the three-dimensional piezoelectric theory for a fully anisotropic piezoelectric rectangular plate as shown in eqn. (5-2).

$$K(x,y) = \frac{Eh^3}{12(1-\nu^2)} \qquad (5\text{-}1))$$

$$K\frac{\partial^4 w}{\partial x^4} + 2K\frac{\partial^4 w}{\partial x^2\,\partial y^2} + K\frac{\partial^4 w}{\partial y^4} + 2\frac{\partial K}{\partial x}\frac{\partial^3 w}{\partial x^3} + 2\frac{\partial K}{\partial y}\frac{\partial^3 w}{\partial y^3} + \frac{\partial^2 K}{\partial x^2}\frac{\partial^2 w}{\partial x^2} + \frac{\partial^2 K}{\partial y^2}\frac{\partial^2 w}{\partial y^2} + \nu\frac{\partial^2 K}{\partial x^2}\frac{\partial^2 w}{\partial y^2} +$$

$$\nu\frac{\partial^2 K}{\partial y^2}\frac{\partial^2 w}{\partial x^2} + K\frac{\partial^2 \nu}{\partial x^2}\frac{\partial^2 w}{\partial y^2} + K\frac{\partial^2 \nu}{\partial y^2}\frac{\partial^2 w}{\partial x^2} + 2\frac{\partial K}{\partial x}\frac{\partial^3 w}{\partial x\,\partial y^2} + 2\frac{\partial K}{\partial y}\frac{\partial^3 w}{\partial x^2\,\partial y} + 2\frac{\partial K}{\partial x}\frac{\partial \nu}{\partial x}\frac{\partial^2 w}{\partial y^2} + 2\frac{\partial K}{\partial y}\frac{\partial \nu}{\partial y}\frac{\partial^2 w}{\partial x^2} -$$

$$2\frac{\partial K}{\partial x}\frac{\partial \nu}{\partial x}\frac{\partial^2 w}{\partial x\,\partial y} - 2\frac{\partial K}{\partial y}\frac{\partial \nu}{\partial y}\frac{\partial^2 w}{\partial x\,\partial y} + 2(1-\nu)\frac{\partial^2 K}{\partial x\,\partial y}\frac{\partial^2 w}{\partial x\,\partial y} - 2K\frac{\partial^2 \nu}{\partial x\,\partial y}\frac{\partial^2 w}{\partial x\,\partial y} + p = -m\frac{\partial^2 w}{\partial t^2}$$

(5-2))

In this equation, ω denotes the excitation frequency, $w = \xi e^{i\omega t}$ is the harmonic deflection of the plate, and $P = pe^{i\omega t}$ represents the harmonic pressure excitation on the plate. If the dynamic deflection amplitude, ξ, is assumed to be a function of X- and Y-axis components, one can easily transform eqn. (5-2) to eqn. (5-3), simply by solving for the partial derivatives. However, since the ABM geometry proposed in this study features a trapezoidal geometry, eqn. (5-3) cannot be directly employed, and a coordinate transformation is needed.

$$K\frac{\partial^4 \xi}{\partial x^4} + 2K\frac{\partial^4 \xi}{\partial x^2\,\partial y^2} + K\frac{\partial^4 \xi}{\partial y^4} + 2\frac{\partial K}{\partial x}\frac{\partial^3 \xi}{\partial x^3} + 2\frac{\partial K}{\partial y}\frac{\partial^3 \xi}{\partial y^3} + \frac{\partial^2 K}{\partial x^2}\frac{\partial^2 \xi}{\partial x^2} + \frac{\partial^2 K}{\partial y^2}\frac{\partial^2 \xi}{\partial y^2} + \nu\frac{\partial^2 K}{\partial x^2}\frac{\partial^2 \xi}{\partial y^2} +$$

$$\nu\frac{\partial^2 K}{\partial y^2}\frac{\partial^2 \xi}{\partial x^2} + K\frac{\partial^2 \nu}{\partial x^2}\frac{\partial^2 \xi}{\partial y^2} + K\frac{\partial^2 \nu}{\partial y^2}\frac{\partial^2 \xi}{\partial x^2} + 2\frac{\partial K}{\partial x}\frac{\partial^3 \xi}{\partial x\,\partial y^2} + 2\frac{\partial K}{\partial y}\frac{\partial^3 \xi}{\partial x^2\,\partial y} + 2\frac{\partial K}{\partial x}\frac{\partial \nu}{\partial x}\frac{\partial^2 \xi}{\partial y^2} + 2\frac{\partial K}{\partial y}\frac{\partial \nu}{\partial y}\frac{\partial^2 \xi}{\partial x^2} -$$

$$2\frac{\partial K}{\partial x}\frac{\partial \nu}{\partial x}\frac{\partial^2 \xi}{\partial x\,\partial y} - 2\frac{\partial K}{\partial y}\frac{\partial \nu}{\partial y}\frac{\partial^2 \xi}{\partial x\,\partial y} + 2\frac{\partial^2 K}{\partial x\,\partial y}\frac{\partial^2 \xi}{\partial x\,\partial y} - 2\nu\frac{\partial^2 K}{\partial x\,\partial y}\frac{\partial^2 \xi}{\partial x\,\partial y} - 2K\frac{\partial^2 \nu}{\partial x\,\partial y}\frac{\partial^2 \xi}{\partial x\,\partial y} - \rho h\omega^2 \xi = -p$$

(5-3)

If we define the new coordinate system, U-V, such that V is along the Y-axis, and U has an angle with the X-axis, the x and y components can be expressed as $x = u\cos\theta$ and $y = u\sin\theta + v$, where θ is the acute base angle. Using the new coordinate system, the

dynamic deflection equation of our trapezoidal continuum, with the aforementioned boundary conditions, can be represented as in eqn. (5-4).

$$K\left[\frac{1}{\cos^4\theta}\frac{\partial^4\xi}{\partial u^4}-\frac{4\sin\theta}{\cos^4\theta}\frac{\partial^4\xi}{\partial u^3\,\partial v}+\frac{6\sin^2\theta}{\cos^4\theta}\frac{\partial^4\xi}{\partial u^2\,\partial v^2}-\frac{4\sin^3\theta}{\cos^4\theta}\frac{\partial^4\xi}{\partial u\,\partial v^3}+\frac{\sin^4\theta}{\cos^4\theta}\frac{\partial^4\xi}{\partial v^4}\right]+2K\left[\frac{1}{\cos^2\theta}\frac{\partial^4\xi}{\partial u^2\,\partial v^2}-\frac{2\sin\theta}{\cos^2\theta}\frac{\partial^4\xi}{\partial u\,\partial v^3}+\frac{\sin^2\theta}{\cos^2\theta}\frac{\partial^4\xi}{\partial v^4}\right]+K\left[\frac{\partial^4\xi}{\partial v^4}\right]+2\frac{\partial K}{\partial x}\left[\frac{1}{\cos^3\theta}\frac{\partial^4\xi}{\partial u^2\,\partial v^2}-\frac{2\sin\theta}{\cos^2\theta}\frac{\partial^3\xi}{\partial u\,\partial v^3}+\frac{3\sin^2\theta}{\cos^3\theta}\frac{\partial^3\xi}{\partial u\,\partial v^2}-\frac{\sin^3\theta}{\cos^3\theta}\frac{\partial^3\xi}{\partial v^3}\right]+2\left[\frac{\partial K}{\partial y}\frac{\partial^3\xi}{\partial y^3}\right]+\frac{\partial^2 K}{\partial x^2}\left[\frac{1}{\cos^2\theta}\frac{\partial^2\xi}{\partial u^2}-\frac{2\sin\theta}{\cos^2\theta}\frac{\partial^2\xi}{\partial u\,\partial v}+\frac{\sin^2\theta}{\cos^2\theta}\frac{\partial^2\xi}{\partial v^2}\right]+\frac{\partial^2 K}{\partial y^2}\left[\frac{\partial^2\xi}{\partial v^2}\right]+$$

$$\nu\frac{\partial^2 K}{\partial x^2}\left[\frac{\partial^2\xi}{\partial v^2}\right]+\nu\frac{\partial^2 K}{\partial y^2}\left[\frac{1}{\cos^2\theta}\frac{\partial^2\xi}{\partial u^2}-\frac{2\sin\theta}{\cos^2\theta}\frac{\partial^2\xi}{\partial u\,\partial v}+\frac{\sin^2\theta}{\cos^2\theta}\frac{\partial^2\xi}{\partial v^2}\right]+K\frac{\partial^2\nu}{\partial x^2}\left[\frac{\partial^2\xi}{\partial v^2}\right]+K\frac{\partial^2\nu}{\partial y^2}\left[\frac{1}{\cos^2\theta}\frac{\partial^2\xi}{\partial u^2}-\frac{2\sin\theta}{\cos^2\theta}\frac{\partial^2\xi}{\partial u\,\partial v}+\frac{\sin^2\theta}{\cos^2\theta}\frac{\partial^2\xi}{\partial v^2}\right]+2\frac{\partial K}{\partial x}\left[\frac{1}{\cos\theta}\frac{\partial^3\xi}{\partial u\,\partial v^2}-\frac{\sin\theta}{\cos\theta}\frac{\partial^3\xi}{\partial v^3}\right]+2\frac{\partial K}{\partial y}\left[\frac{1}{\cos^2\theta}\frac{\partial^3\xi}{\partial u^2\,\partial v}-\frac{2\sin\theta}{\cos^2\theta}\frac{\partial^3\xi}{\partial u\,\partial v^2}-\frac{\sin^2\theta}{\cos^2\theta}\frac{\partial^3\xi}{\partial v^3}\right]+2\frac{\partial K}{\partial x}\frac{\partial\nu}{\partial x}\left[\frac{\partial^2\xi}{\partial v^2}\right]+2\frac{\partial K}{\partial y}\frac{\partial\nu}{\partial y}\left[\frac{1}{\cos^2\theta}\frac{\partial^2\xi}{\partial u^2}-\frac{2\sin\theta}{\cos^2\theta}\frac{\partial^2\xi}{\partial u\,\partial v}+\frac{\sin^2\theta}{\cos^2\theta}\frac{\partial^2\xi}{\partial v^2}\right]-$$

$$2\frac{\partial K}{\partial y}\frac{\partial\nu}{\partial x}\left[\frac{1}{\cos\theta}\frac{\partial^2\xi}{\partial u\,\partial v}-\frac{\sin\theta}{\cos\theta}\frac{\partial^2\xi}{\partial v^2}\right]-2\frac{\partial K}{\partial x}\frac{\partial\nu}{\partial y}\left[\frac{1}{\cos\theta}\frac{\partial^2\xi}{\partial u\,\partial v}-\frac{\sin\theta}{\cos\theta}\frac{\partial^2\xi}{\partial v^2}\right]+2\frac{\partial^2 K}{\partial x\,\partial y}\left[\frac{1}{\cos\theta}\frac{\partial^2\xi}{\partial u\,\partial v}-\frac{\sin\theta}{\cos\theta}\frac{\partial^2\xi}{\partial v^2}\right]-2\nu\frac{\partial^2 K}{\partial x\,\partial y}\left[\frac{1}{\cos\theta}\frac{\partial^2\xi}{\partial u\,\partial v}-\frac{\sin\theta}{\cos\theta}\frac{\partial^2\xi}{\partial v^2}\right]-2K\frac{\partial^2\nu}{\partial x\,\partial y}\left[\frac{1}{\cos\theta}\frac{\partial^2\xi}{\partial u\,\partial v}-\frac{\sin\theta}{\cos\theta}\frac{\partial^2\xi}{\partial v^2}\right]-\rho h\omega^2\xi=-p \quad (5\text{-}4)$$

Eqn. (5-4) can be solved using the elastodynamic finite (central) difference discretization method proposed by Dovgilovich and Sofronov [140-143]. Δu and Δv represent the displacement components between two consecutive nodes. Considering the geometry of the continuum, Δu is invariable along the continuum. However, due to the trapezoidal geometry of the plate, Δv is a non-uniform variable, linearly increasing along the length of the continuum from the base to the apex. The elastodynamic equation of the proposed ABM continuum, represented by eqn. (5-4), was solved using a custom-written MATLAB program. As per the boundary conditions, it was assumed that the plate is fixated to the lateral supports at the base and the two non-parallel sides (i.e., legs of the trapezoid).

In addition, at the freely moving side (i.e., apex), the bending moment and shear force were considered to be zero. In this study, our material of choice for the ABM plate was Polyvinylidene Fluoride (PVDF), the properties of which were used to solve eqn. (5-4). These properties as well as the geometrical dimensions are tabulated in Table 5.2.

5.4 Plate Type Sensor Model Description and Numerical Modeling

To further investigate the proposed ABM dynamic behavior and to validate the analytical model, a finite-element analysis (FEA) was performed using COMSOL Multiphysics® employing the aforementioned boundary conditions. Since this study aims to verify the analytical and numerical models by fabricating a proof-of-concept prototype of the proposed ABM structure and experimental testing, we chose tractable feature sizes, as summarized in Table 5.2.

Table 5.2: Material properties of the model and notations

Parameters	Value	Unit
Stiffness (E)	4.1	GPa
Density (ρ)	1780	Kg/M^3
Poisson Ratio (ν)	0.18	
Length (L)	40	mm
Base width (B_i)	3	mm
Apex Width (B_f)	5	mm
Thickness (h)	45	µm

For the numerical simulations, a harmonic unit pressure, 1 Pa, (i.e., 94 dB sound pressure level), along the frequency range of 1 kHz to 10 kHz, was applied over the top surface of

the plate as the excitation input. Deflection patterns of the ABM plate were numerically analyzed, considering no-movement boundary condition at the base and lateral sides of the plate. Figure 5.3 plots the continuum's deflection responses at four distinct oscillation frequencies (i.e., 4538 Hz, 5533 Hz, 6546 Hz, and 7633 Hz). As depicted in this figure, the maximum localized deflection due to low-frequency excitations occurs toward the ABM's apical end, and gradually shifts toward the base as the excitation frequency increases. This spatial shift in the induced deflection is due to the fact that the bending stiffness of the plate is lower at the apex as compared to the base, which is directly caused by gradual variation in the width of the plate along the X-axis, even though the entire plate has a constant modulus of elasticity. The vibration energy with a given frequency is distributed across the entire plate but induces largest response at a single location with an eigenfrequency matching the excitation frequency.

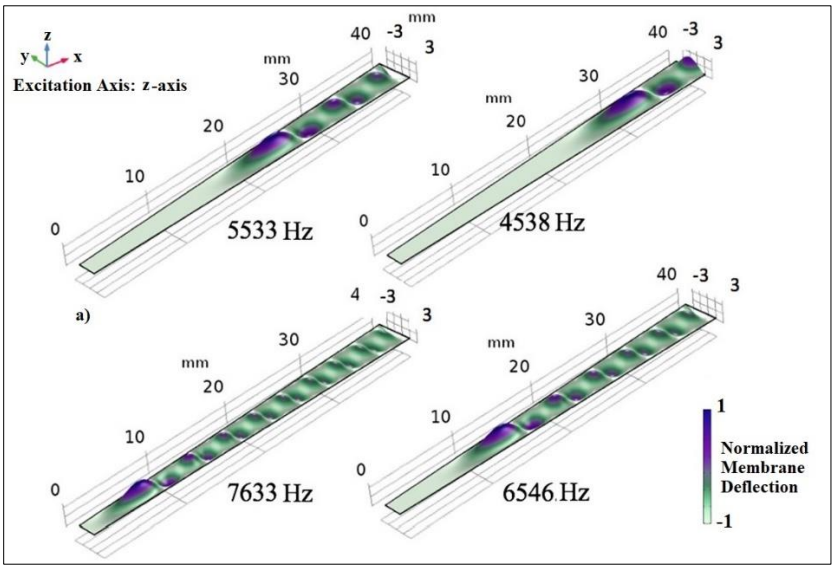

Figure 5.3: Normalized deflection patterns of the plate in response to different acoustic pressure excitation frequencies. This plate is suspended over a trapezoidal duct embedded in a bottom support and is fixated at every side except the apical end.

As can be seen in Figure 5.3, along with the maximum deflection peak, a number of

trailing peaks with smaller amplitudes appear toward the apical end. In the human cochlea, the BM is submerged in a viscous fluid, which serves as the travelling-wave medium, and hence forms a membrane-fluid interface. This interface serves to damp out the smaller deflection peaks, thereby attenuating the crosstalk among the frequency channels. For the sake of fabrication simplicity, the current proof-of-concept model was intended to function in the atmospheric medium, and a fluidic medium was avoided.

5.5 Beam Type Sensor Model Description and Numerical Modeling

In 2013, Tanujaya et al. [134] presented a beam type acoustic sensor inspired from an artificial basilar membrane prototype to catch sinusoidal waves at various frequencies using Laser Doppler Vibrometer. White and Grosh [135] constructed a micro-engineered hydromechanical cochlea that has a micromachined membrane as well as a fluid-filled duct to mimic the cochlear chamber. However, the response frequencies detected by the acoustic input were above the audible frequency range. In a recent study, Kim et al. [124, 136] assessed the frequency selectivity of an artificial basilar membrane constructed using a piezoelectric beam array. Though a considerable number of studies are performed to model artificial mechanical cochlea, a complete experimentally fabricated sensor based on a beam type Acoustic sensor inspired from a basilar membrane model is missing. A model is truly demanded that will guide and enhance the performance of the fabricated sensor or help to design the sensors accurately/predictively with tailored target application in mind. Figure 5.4 shows the schematic of the proposed spiral broadband sensor model including 100 Zinc Oxide electrodes with thickness from $2e^5$ Å (20 μm) to $1.1e^6$ Å (110 μm). For the proposed beam type acoustic sensor, similar to the plate type acoustic sensor mentioned in above section, a trapezoidal geometry is adopted. Here, proposed continuum features a 10 μm thick isosceles

trapezoidal geometry out of silicone material which eventually situated atop an elastomer matrix with embedded electrode grooves and a duct. Unlike the plate type concept in which the continuum is the piezoelectric material (PVDF), in the beam type concept, the electrodes themselves are the piezoelectric materials (ZnO) which are sandwiched in between to silicone membranes, Figure 5.4a. The design is in such a way that there are 100 electrodes along the 100 mm continuum in such a way that the length and the thickness of each electrode vary linearly along the length of the trapezoidal continuum as shown in figure 5.5.

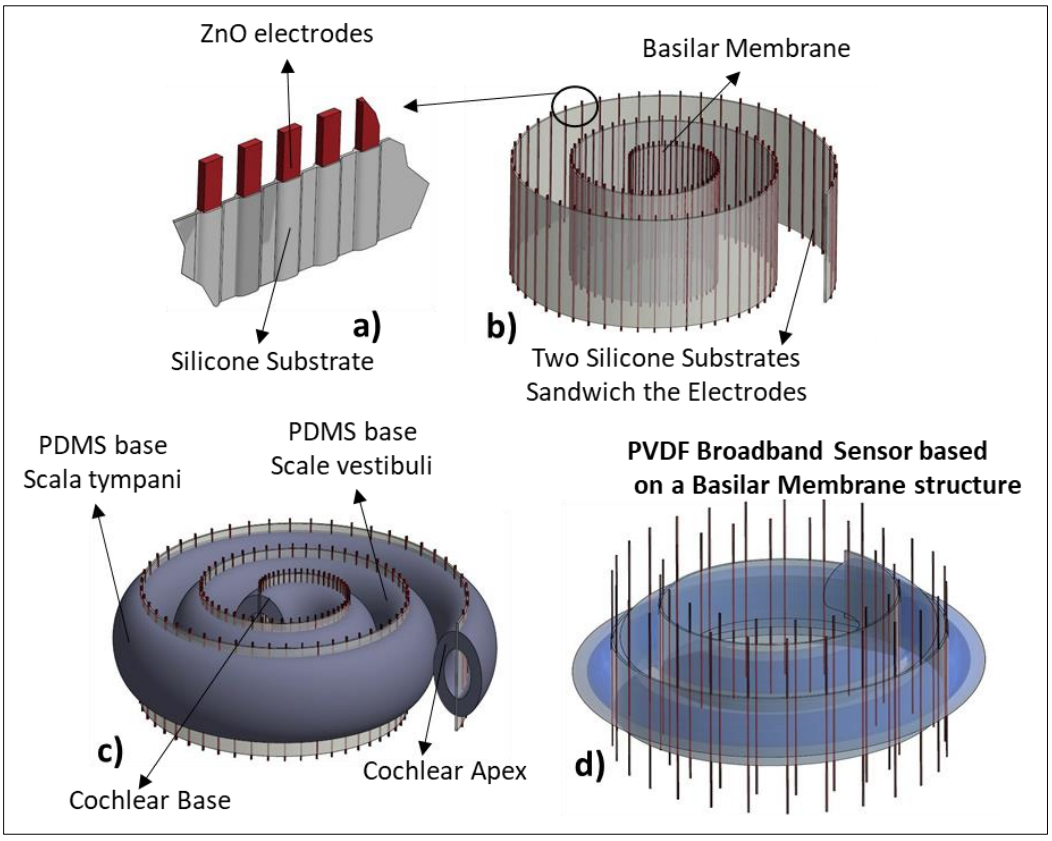

Figure 5.4: CAD Schematic of the proposed Broadband Sensor.

Hence, the first electrode which is near the apex side has 8 mm length, 300 μm width and 20 μm thickness and the last electrode near the base has 3 mm length, 300 μm width and 110 μm thickness. In this design, the silicone membrane which now has the electrodes sandwiched in between is eventually placed between another two PDMS structure that have a half conical

duct on them, Figure 5.4c. Finally, the whole structure which now is turned to a spiral shape is covers in another PDMS structure that holds the whole sensor fixed within itself, Figure 5.4d.

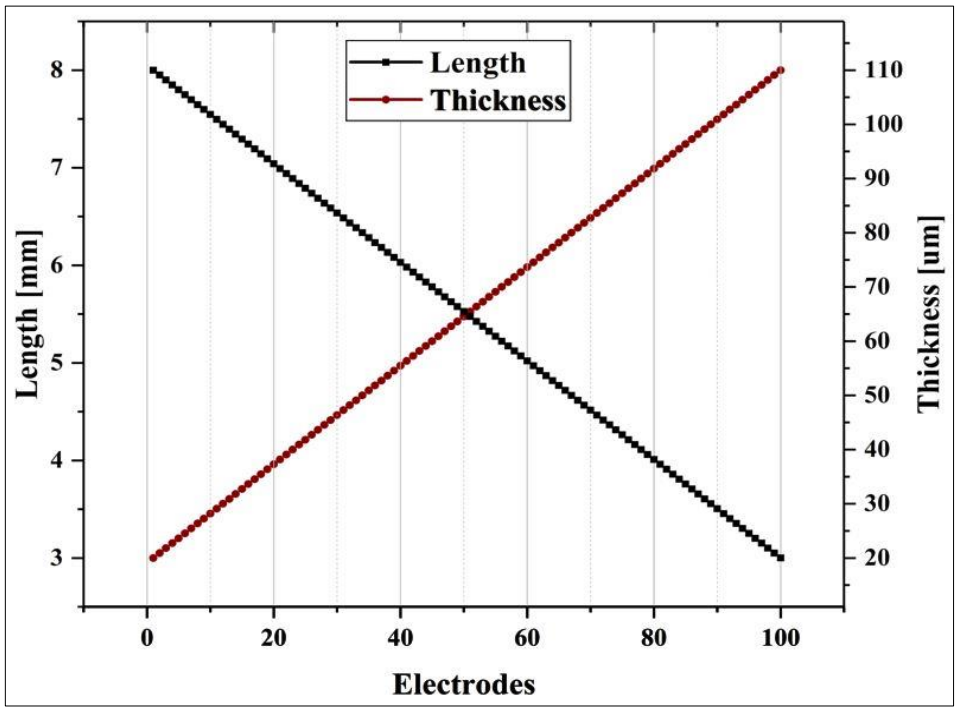

Figure 5.5: The length and the thickness of each electrode vary linearly along the length of the trapezoidal continuum.

5.6 **Plate type Sensor Fabrication**

In this section, the fabrication process and the experimental setup for fabrication of Plate type acoustic sensor are explained.

5.6.1 PDMS-PVDF Broadband Sensor Fabrication

The proposed broadband frequency sensor was fabricated in the Marcus Nanotechnology Research Center of Georgia Institute of Technology, Atlanta, USA. In order to experimentally validate the analytical and numerical modeling performed in the previous sections, the proposed model was custom fabricated with the dimensions as per

Table 5.2. Figure 5.6 shows various layers of the fabricated sensor. First, a Polydimethylsiloxane (PDMS) device was fabricated via soft lithography techniques as a support medium. In fact, this PDMS structure provides a tube shape structure which holds the basilar membrane. This PDMS structure mimics the functionality of an organ in the human's cochlear called Scala tympani. Figure 5.6 illustrates the fabrication process from the initial photolithography to the final device-substrate bonding. In this fabrication procedure, at first, SU-8 negative photoresist was used as a mold, and PDMS was used to form the basic form of the scala tympani support.

In the process of fabrication, a silicon wafer was utilized as the substrate with 3in diameter, SU-8 3025 was utilized as photoresist, and PDMS utilized as the main support device material with critical dimension accuracy of ~100um. In the first step, silicon wafers with the aforementioned trapezoidal shape and 45um thickness were placed on a hot plate at 200^{o}C for 15 mins to evaporate the excess moisture on the surface of the wafer. Next, SU-8 3025 negative photoresist was spin-coated at 95^{o}C at 500 rpm for 10 seconds on the wafer, followed by a second spin-coating at 3000 rpm for 40s. Subsequently, the beakers were rinsed and cleaned with IPA. A little developer was then poured in the beakers to cover the samples. After placing the wafers in the developer, the beakers were gently shaken to agitate the solution. At the end of this step, the samples were cleaned and dried on text-wipe with a Nitrogen spay gun as depicted in Figure 5.6a and 5.6b. After spin coating, the samples were inspected under microscope for a uniform development of the photoresists (Figure 5.6c). Next, PDMS polymer was prepared. PDMS was mixed with a 1:10 ratio of curing agent and PDMS monomers and stirred for 8 minutes using plastic straws. A desiccator was used to remove the bubbles in the mixture. The wafers were

covered by the mixture and placed inside a convection oven to cure the PDMS matrix (Figure 5.6 d-f).

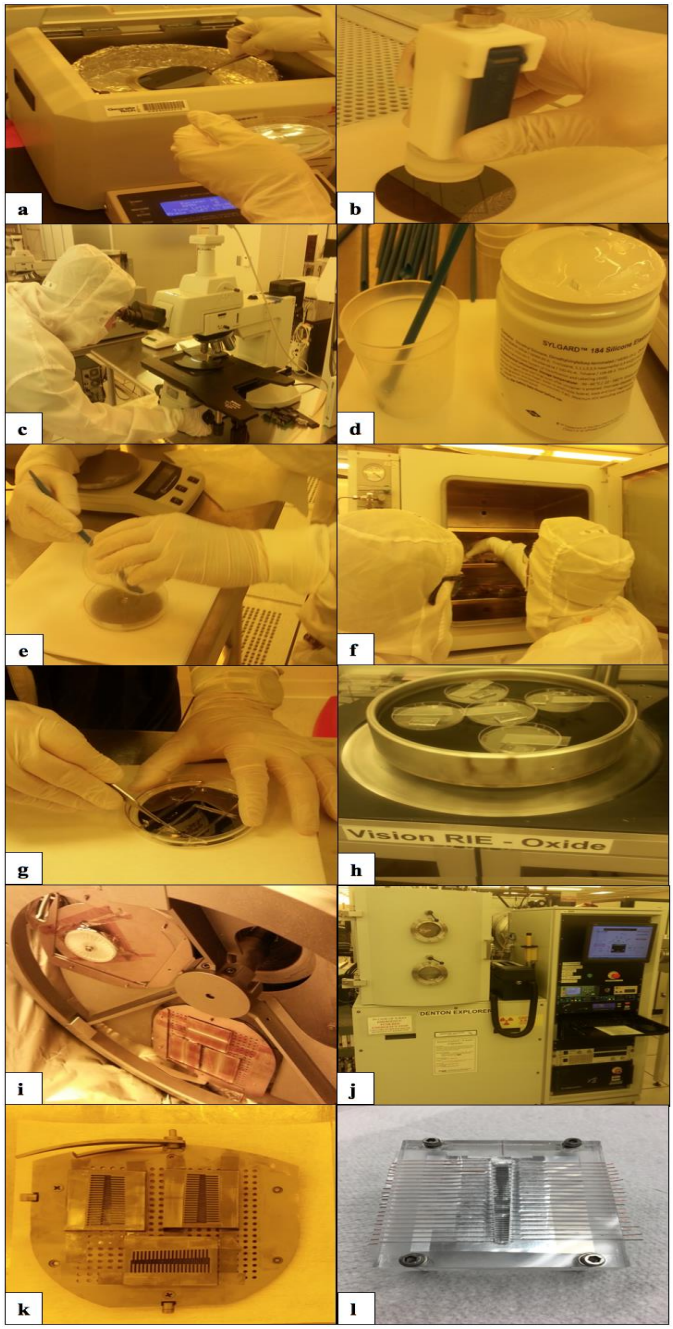

Figure 5.6: Fabrication steps of the proposed Basilar Membrane sensor.

The samples were then transferred to a Vision 320 RIE, which is a manually loaded reactive ion plasma system to shallow silicon using SF6 as an etching gas (Figure 5.6 g-h).

Upon this step, the solid PDMS samples contain the desired pattern of scala tympani and can be bonded to a PVDF basilar membrane prepared next.

For preparing the PVDF membranes, a Denton Explorer E-beam Evaporator was used, which is a six-pocket e-beam evaporator for coating various metals and dielectrics. A high-intensity beam of electrons was focused on the center of a crucible containing the material to be evaporated. In this step, PVDF membranes were precisely cut by a laser cutter and placed between shadow masks in order to be placed inside the Denton Explorer. The pressure inside the evaporator's chamber was lowered to $3e^{-6}$ Torr in order to increase the mean free path and prevent air molecules from interrupting metal atoms as they travel from the evaporation source to the membrane. Then, gold was heated to the point of vaporization by a high-intensity beam of electrons and was deposited on the membrane at a 2 Å/s rate. In this step, 30 electrodes from gold with the thickness of 1 μm were deposited on the membranes. Endpoint detection procedure was implemented through the Inficon XTC/2 quartz crystal rate. In the final step, each membrane was bonded to the scala tympani PDMS samples and firmly placed on an acrylic structure as shown in Figure 5.6l.

5.6.2 Experimental Setup.

In order to experimentally validate the functionality of the fabricated sensor and systematically characterize its performance, in accordance with the intended features of the sensor, a vibration exciter with the capability of accurate acoustic excitation in a wide range of frequencies is required. In our integrated Material Assessment and Predictive Simulation (iMAPS) laboratory, we have designed and fabricated an Acousto-Electrodynamic Vibration Exciter, AEVE-3D, which can provide precise acoustic vibration excitations in

a wide frequency range [31, 88]. AEVE 3-D consists of three mechanical shakers and three acoustic exciters which are connected in three Cartesian directions. Sinusoidal signals with desired frequencies are generated and separately fed to each actuator. Figure 5.7 shows the experimental setup. In this study, only the vertical acoustic exciter was used while the other two acoustic exciters and the mechanical shakers remained off. To mount the fabricated sensor firmly in the center of the AEVE 3-D's end-effector, a custom-made aluminum mounting structure was designed and built. All the experiments and data collection were performed in an acoustic noise isolated environment in our laboratory.

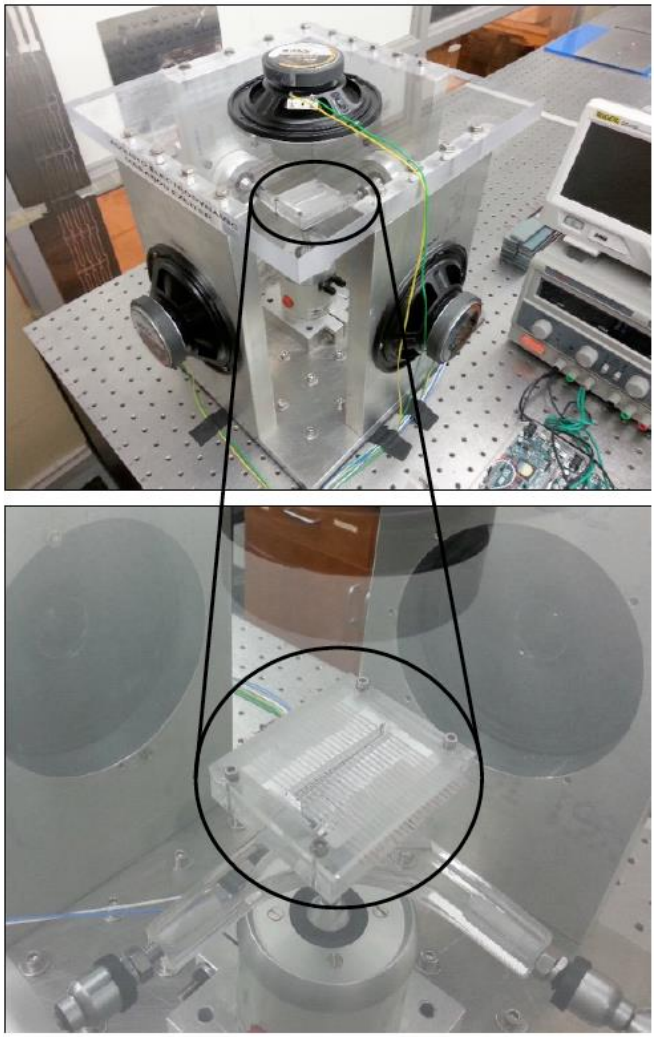

Figure 5.7: Experimental setup including AEVE 3-D, function generator, signal amplifier and a DAQ in sound isolated laboratory.

5.6.3 Data acquisition system

To measure the outputs of each individual deposited electrode in this sensor, a custom-made multi-channel, ultra-fast, ultra-high precision data acquisition system (DAQ) was developed. This DAQ employed a precision digital-to-analog converter (ADC) from Texas Instruments (i.e., DDC2256A), a signal conditioning stage, an instrumentation amplification stage, a power management system. The DDC2256A is a 24-bit, multi-channel ADC which allows up to 256 individual signals be sampled and digitized simultaneously at very high sampling rates, which is particularly compatible with the low-voltage, high-frequency nature of the typical signals in this application. Upon sampling and digitization of the basilar membrane sensor, all the resulting data are output over a single low-voltage differential signaling (LVDS) serial interface. The LVDS interface is specifically suitable for this application as it minimizes noise coupling in this high-channel data acquisition application. Furthermore, the signal-conditioning and amplification stages accommodate signal filters and regulate supply voltages required for the proper functioning of the DAQ. Upon receipt of the readings from the basilar membrane sensor in the micro-processing unit, online data processing and digital filtration techniques is employed, followed by relaying the processed data stream to a computer through high-speed USB ports for further analysis and real-time data visualization.

5.7 Plate type Sensor Fabrication

In this section, the fabrication process and the experimental setup for fabrication of Beam type acoustic sensor are explained. Figure 5.8a and 5.8b show the CAD design and the 3D printed shadow mask that is used in Denton explorer evaporation machine to deposit the electrodes on the 10 µm thick silicone membrane. Here in, Zinc Oxide is used to fabricate the

required membrane which is including 100 electrodes with thicknesses from $2e^5$ Å (20 μm) to $1.1e^6$ Å (110 μm). In the fabrication procedure, a high-intensity beam of electrons bombards the center of a crucible to evaporate our piezoelectric material inside the crucible and then the chamber is be pumped down to a pressure of 3e-6 Torr in order to deposit the electrodes. Depositing the electrodes on the Silicone membrane through the shadow mask starts at 2 Å/s rate. Since, in the proposed design, each electrode has a different thickness, after reaching each electrode to its proper thickness, the corresponding groove for that electrode gets closed to avoid more deposition on that electrode. Hence, the first groove on the shadow mask that is for electrode on the Apex gets closed at $2e^5$ Å thickness and this process continues to the last electrode that is on the Base side and it gets closed at $1.1e^6$ Å thickness. In the next part, PDMS polymer is prepared. PDMS is mixed with a 1:10 ratio of curing agent and PDMS monomers and stirred for 8 minutes using plastic straws. A desiccator is used to remove the bubbles in the mixture.

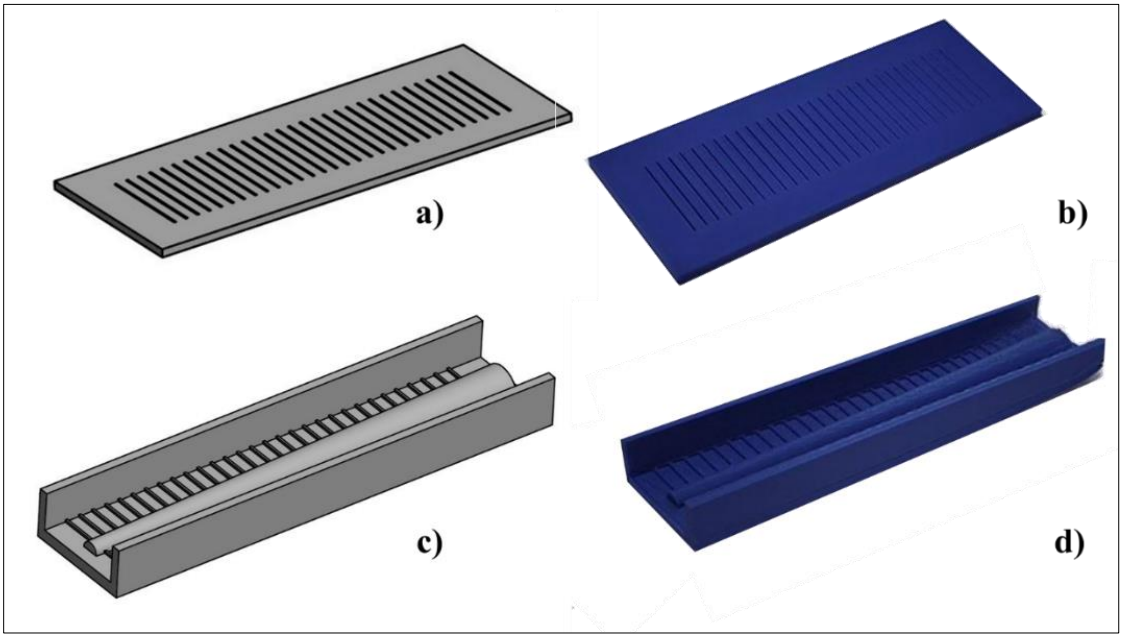

Figure 5.8: The CAD drawing and the 3D printed shadow mask for the electrode deposition and the mold for the PDMS structure of the proposed acoustic sensor.

The wafers mold in Figure 5.8c and 5.8d covered by the mixture and placed inside a convection oven to cure the PDMS matrix. Upon this step, the solid PDMS structures containing the desired pattern of scala tympani and scala vestibuli that can be bonded to the silicone membrane is prepared.

5.8 Results and Discussions

As mentioned in Section III, depending on the broadband sensor application, the frequency band varies according to its geometric configuration and material properties. Due to the fabrication limitations, the PVDF material properties and the reported geometric configuration reported in Table 5.2 are utilized to analytically and numerically model the sensor and eventually present a proof-of-concept sensor. Furthermore, to solve the deflection equation, a uniform plate thickness was assumed for the basilar membrane sensor. In such scenario, analytical and numerical modeling results, presented in Figure 5.9, show that, over the 40mm length of the basilar membrane from 5mm apex width (free condition) to 3mm base width (fixed condition), the frequency band changes from 3036Hz to 8059Hz. The developed predictive analytical model and numerical model support different types of boundary conditions, geometric configurations, and material properties. However, in this study, sensing capabilities are reported only employing the fixed boundary connections (except apex side) with PVDF material properties and geometric configuration reported in Table 5.2.

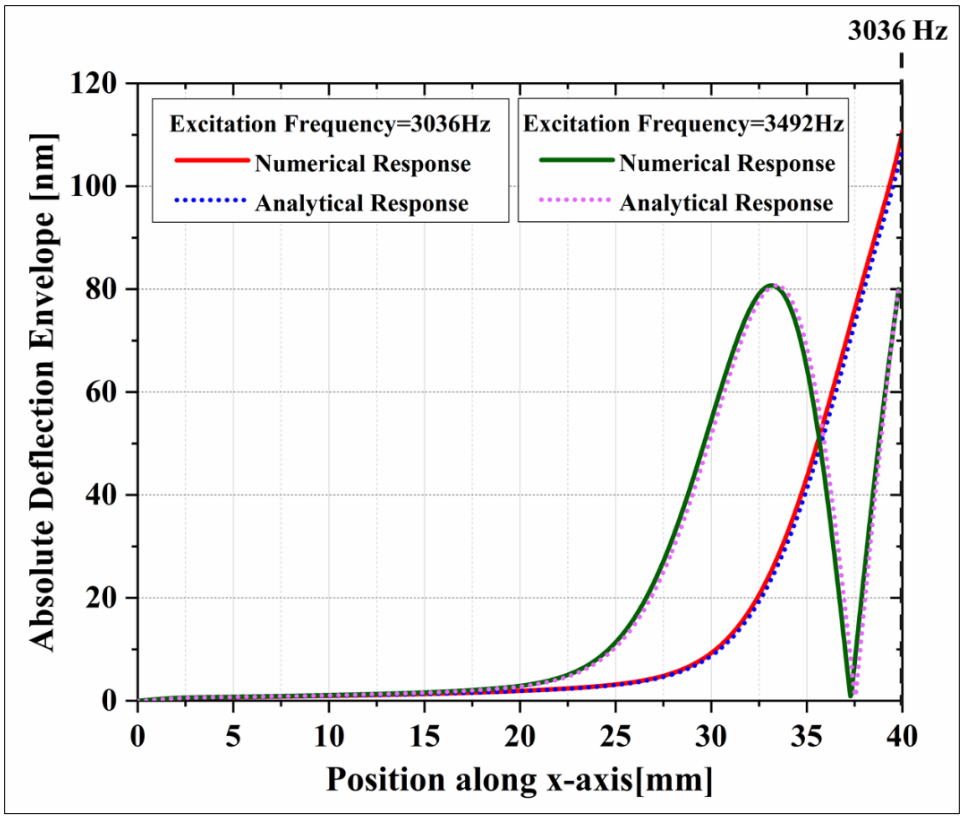

(a)

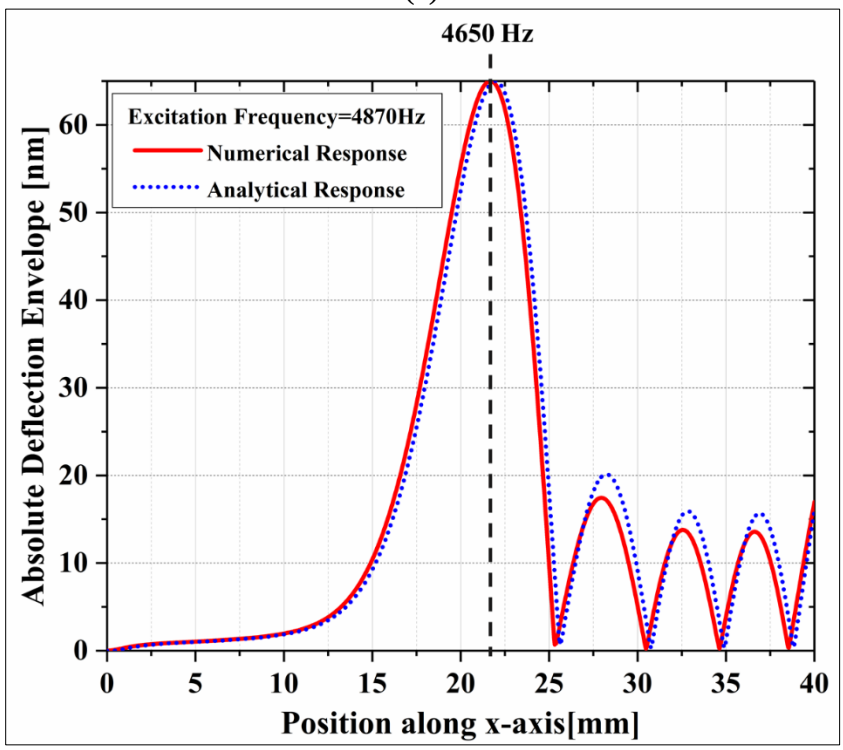

(b)

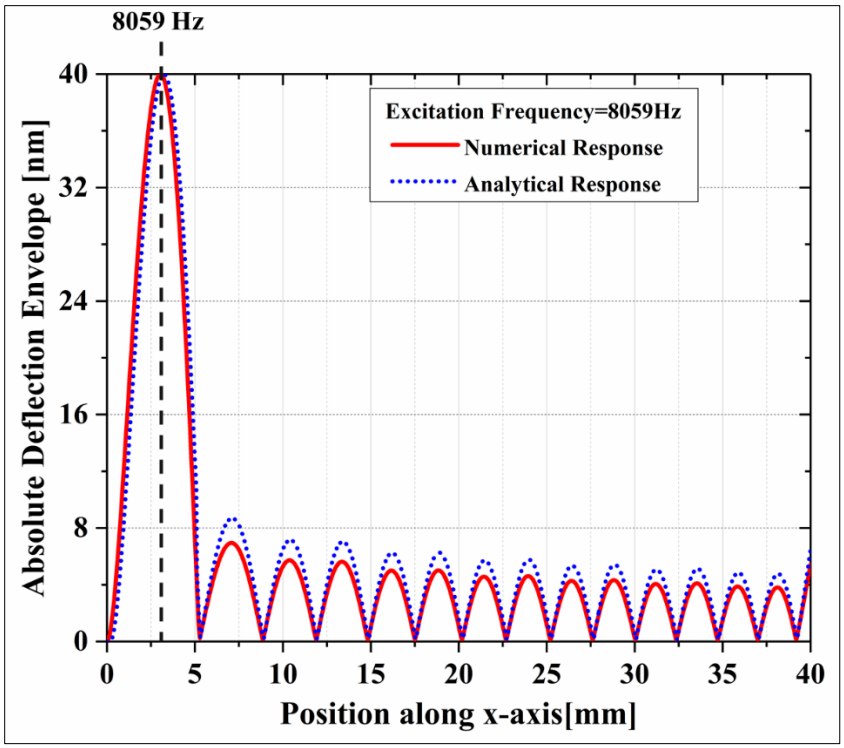

(c)

Figure 5.9: Numerically (COMSOL Multiphysics) and analytically obtained deflection profile of the sensor at (a) Apex side frequency at~3 KHz (b) middle point at 4650 Hz (c) Base side frequency at ~8 KHz.

Figure 5.9a shows that at the lower frequency range of this ~5KHz frequency band sensor, which is ~3KHz, the maximum localized deflection of the membrane can be measured towards the apical end of the model, while the Figure 5.9c shows that at the higher frequency range of this sensor which is ~8KHz, the maximum localized deflection can be measured towards the base side of the membrane model. The deflection location is shifted towards the apex side or base side with decreasing or increasing excitation frequency, respectively. This phenomenon is quite trivial since the bending rigidity of the structure is lower at the apical end, compared to the base, and this is due to the increase in the width of the membrane, even though a constant modulus of elasticity is defined for the computations. Comparing the analytical and numerical deflection results in Figure 5.9, it

can be seen that the apex and base responses from both predictive model and the FEM analysis are in very close agreement.

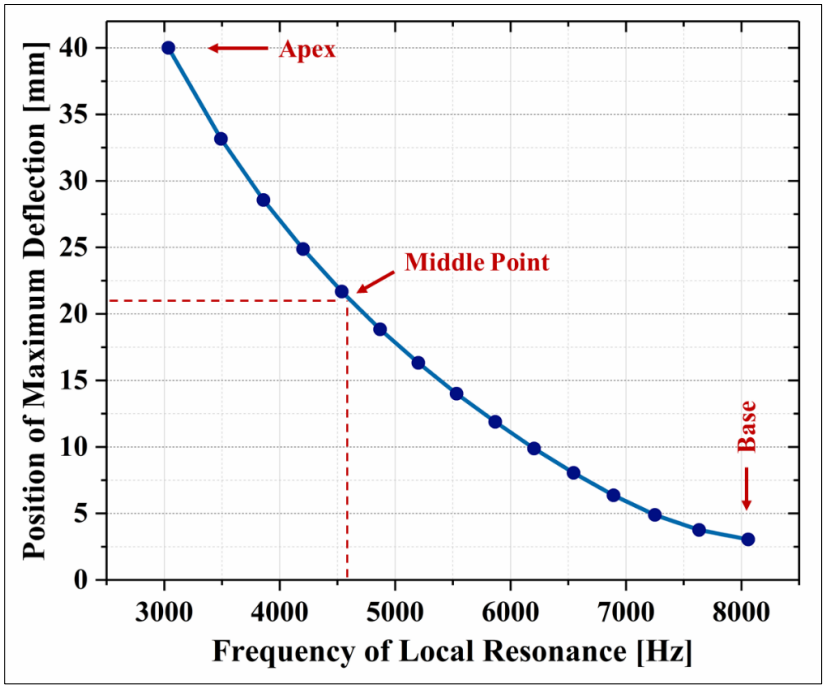

Figure 5.10: Location of maximum deflection peak in response to acoustic excitations with varying frequencies.

Figure 5.10 shows the FEA results for the position of maximum deflection with respect to the excitation frequency. According to this figure, the maximum deflection location shifts toward the apical end or basal end with decreasing or increasing the frequency of acoustic excitations, respectively. This observation confirms the desired spatial frequency selectivity and mapping of the proposed ABM structure, which was inspired from the biological basilar membrane. This characteristic is in accordance with the behavior expected from the proposed structure as the bending stiffness of the plate becomes larger from the apex toward the base, which is due to the gradual growth in the width of the ABM plate, even though a constant modulus of elasticity was defined for the entire plate.

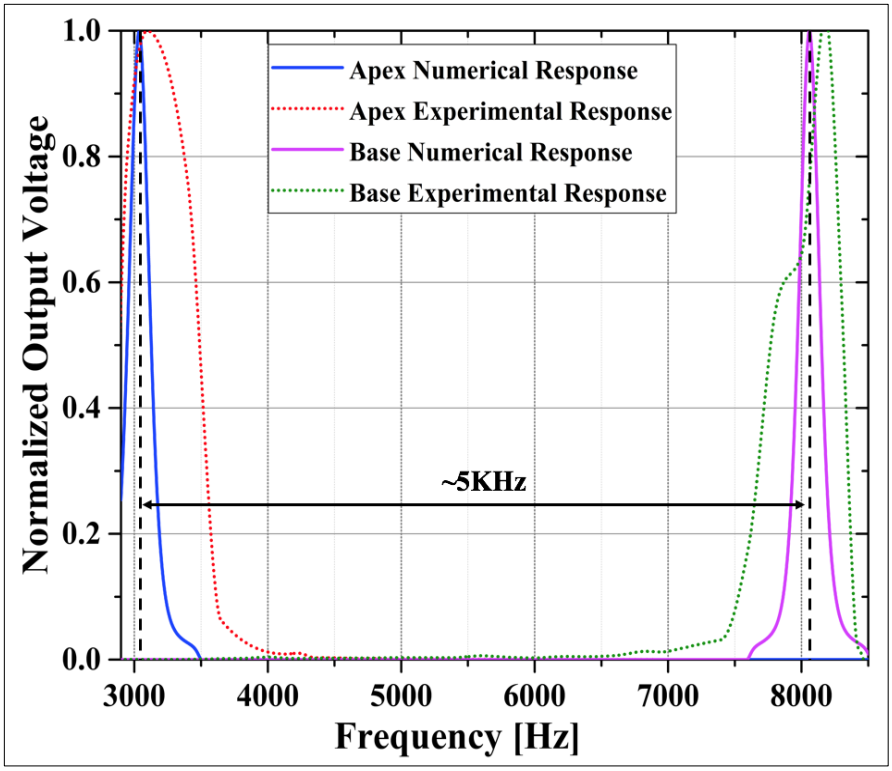

(a)

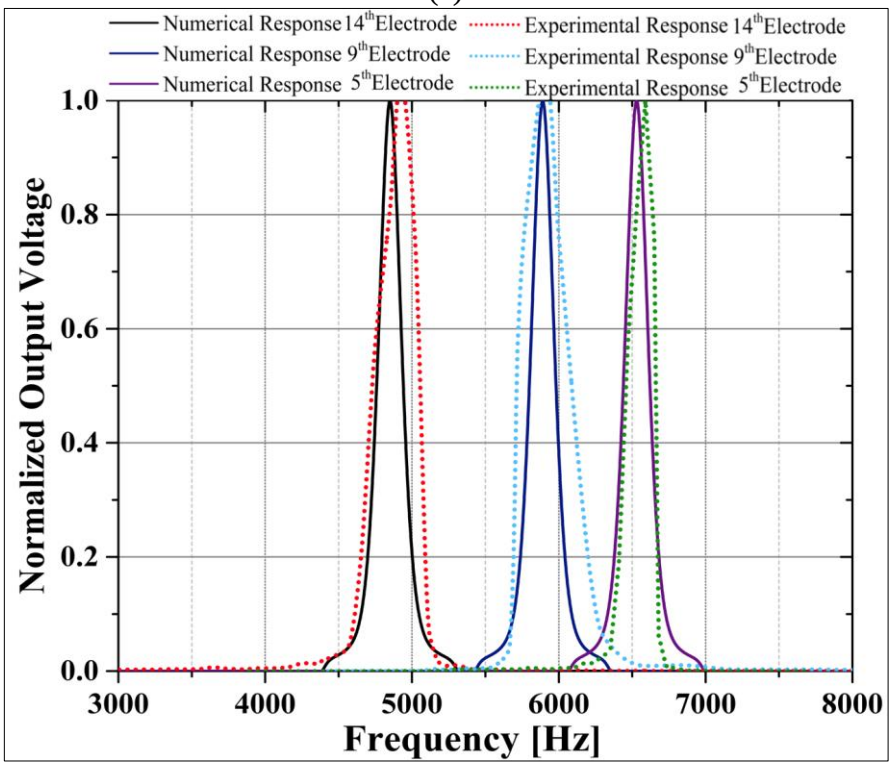

(b)

Figure 5.11: Numerical results and experimental responses of 5 different electrodes at different frequencies.

Although, in the numerical analyses for validation of the analytical model, deflection was used as the output signal of interest, such deflection can easily be converted to electrical voltage through implementing smart materials, such as piezoelectric material. During the fabrication process, similar to the numerical modeling, the apex side of the membrane was maintained free and the base side was held fixed. 30 electrodes with the thickness of 1 micron were deposited on the 40mm length of the PVDF membrane with distance of 1.333mm such that the first electrode is on the apex side, and the 40^{th} electrode is shifted by 1.333mm toward the base side. In this study, the fluidic media was avoided. As a proof-of-concept, the current design of our sensor is intended to function in the air medium. For the sake of better presentation, only the measured outputs of 5 individual deposited electrodes started from apex towards the base side are presented in Figure 5.11. As expected, the maximum output response of the developed PVDF base basilar membrane at frequency of ~3KHz is by the electrode deposited on the apex side, while the maximum output response, at frequency of ~8KHz, is by the electrode deposited near the base side of the membrane (Figure 5.11a). Additionally, Figure 5.11b presents the normalized output response of three other electrodes at three different locations at their corresponding frequency. Comparing the numerical and experimental measured outputs in Figure 5.11, it can be seen that the response from the FEM analysis and fabricated sensor are in very close agreement. The experimental measured outputs showed that, over the 5KHZ frequency range of the fabricated sensor, there is a minor difference (lower than 80Hz) between numerical and experimental outputs across the membrane. A number of factors may contribute to this uncertainty, such as human error, slippage of the experimental setup, ambient temperature, and gradual degradation in the functionality of the fabricated

samples. However, it was observed that the frequencies at which the peak responses occur are highly consistent across experiments although the amplitudes may show minor variability.

5.9 Chapter Conclusion

In this study, an artificial basilar membrane (ABM) electrode array with longitudinal coupling, inspired from the structure of a human basilar membrane, was proposed. The proposed ABM incorporated a PVDF trapezoidal continuum with an array of old electrodes distributed across its top and bottom surfaces, as well as a PDMS support matrix with a longitudinal duct and electrode grooves. We provided analytical and numerical modeling for the proposed structure and verified its functionality through fabrication of a proof-of-concept model and experimental testing. The ABM developed in this study demonstrated the intended spatial frequency and mapping along its longitudinal axis, mimicking its real-life counterpart, and converted the acoustic stimulations to electric potential without an external power source. In future studies, we will optimize the proposed ABMs structure for its size, as well as its detection bandwidth to cover the entire audible frequency range.

CHAPTER 6:

MISCELLANEOUS ACTIVITIES

6.1 Abstract

A high percentage of failures in sensors and devices employed in harsh industrial environments and airborne electronics is due to mechanical vibrations and shocks. Therefore, it is of paramount importance to test equipment reliability and ensure its survival in long missions in the presence of physical fluctuations. Traditional vibration testbeds employ unidirectional acoustic or mechanical excitations. However, in reality, equipment may encounter uncoupled (unidirectional) and/or coupled (multi-directional) loading conditions during operation. Hence, to systematically characterize and fully understand equipment's behavior, a testbed capable of simulating a wide variety of vibration conditions is required. The primary objective of this work is design, fabrication, and testing of AEVE 3D, an Acousto Electrodynamic three-dimensional (3-D) Vibration Exciter, which simulates coupled and decoupled (with unpowered arms) 3-D acoustic and/or 3-D mechanical vibration environments. AEVE 3D consists of three electromagnetic shakers (for mechanical excitation) and three loudspeakers (for acoustic excitation) as well as a main control unit that accurately calculates and sets the actuators' input signals in order to generate optimal coupled and decoupled vibrations at desired frequencies. In this paper, the system's architecture, its mechanical structure, and

electrical components are described. In addition, to verify AEVE 3D's performance, various experiments are carried out using a 3-D Piezoelectric energy harvester and a custom-made Piezoelectric beam.

6.2 Introduction

In rugged industrial environments as well as aeronautics, a major portion of failures in devices and sensors are due to mechanical vibrations and sudden shocks. Therefore, it is of paramount importance to test equipment reliability and ensure its survival in long missions in the presence of physical fluctuations prior to in situ applications. Vibration tests using exciters help designers to determine the optimal configurations and component placement in order to avoid future problems and failures [144, 145]. Vibration refers to a phenomenon generally occurring in mechanical structures upon harmonic excitation [146]. Resonance, a key phenomenon in vibration analysis, takes place when the frequency of the excitation comes close to the natural frequency of a structure [147]. While structural resonance can be devastating for some mechanical structures, it is useful in an energy-harvesting domain to scavenge electric energy from mechanical vibration [6, 51, 87]. Thus, understanding how vibration influences mechanical structures has become prominent in such structures, and vibration testing has become a fundamental methodology of the experimental science. A few examples of vibration studies in laboratories are; vibration test to simulate the vehicle response under road roughness, fatigue strength test for engineering materials under high frequency, endurance test, and instrument calibration by exerting simple harmonic output forces or displacements [148]. Vibration analysis is also crucial in aircraft and ship manufacturing, machining, bridges and buildings [149].

Vibration tests are commonly conducted under an artificial environment provided by the vibration exciters [150]. A vibration exciter is a transducer which converts electrical energy into an oscillating mechanical motion [146]. Three types of vibration exciters are commonly used in the industry; mechanical, electrohydraulic, and electrodynamic [151]. Mechanical vibration exciters operate based on the principle of vibration excitation using a centrifugal force or directly by a cam-shaft mechanism [152]. In electrohydraulic vibration exciters, an exciting force from a high-frequency servo-valve controls a hydraulic piston and excites a working table. Bai et al. [153] proposed a novel electrohydraulic vibration exciter consisting of a 2-D servo control valve and double acting hydraulic cylinder. The vibration frequency and amplitude were determined by the rotary and linear motion of a 2-D valve spool, respectively. Electrohydraulic exciters are characterized by their large output force although their frequency domain highly depends on the servo valve's dynamic response rate, which is limited to a few hundred Hz [150, 151]. Electrodynamic vibration exciters operate based on the Lorentz principle by supplying an electromagnetic coil with a sinusoidal current waveform. Electrodynamic exciters are limited to specific configurations and operating parameters and generally vibrate along a single axis [154]. In comparison with the mechanical exciters, the electrodynamic exciters have a wider bandwidth. However, due to magnetic saturation, they are incapable of producing a large output force without sacrificing the bandwidth.

Sources of ambient vibrations can be divided into three main categories: 1) seismic vibration, 2) acoustic vibration, and 3) vibration applied directly to the load on the working surface [155]. Seismic vibration refers to all sources that make the floor vibrate, such as vehicle engines, wind blowing against buildings, and ventilation fans [156, 157]. Many of

the sources that generate seismic vibrations also generate acoustic vibrations. The difference is that acoustic vibrations are the effect of air pressure variations on the object [158]. In recent years, researchers have adopted different configurations of vibration testbeds to simulate a wide variety of ambient vibrations. In 2012, Kim et al. [159] proposed a resonant-type electromagnetic 1-D vibration exciter which consisted of an inner steel yoke with four rectangle-shaped small permanent magnets and an outer steel yoke with eight large permanent magnets. This vibration exciter was then used as a testbed for the rapping of an electrostatic precipitator to remove dust from collecting plates without direct impact on them. Despite the novel idea, the proposed vibration exciter was only capable of providing 1-D excitation with a low frequency range and amplitude [106, 160, 161].

Pluta et al. [151] presented a 2-D mechanical vibration exciter consisting of two servomechanisms, a station of hydraulic power supply, an electric power supply, and a control system to provide extorting bi-axial vibrations. Their aparatues was then used to machanically excite a telecommunication mast in order to analyze its dynamic behavior, and to design various vibration reduction systems and transmission factors Ziming et al. [162] developed a unidirectional hydraulic vibration testbed, and studied mechanics of periodic hydraulic fluctuations. The developed exciter was then used as a test apparatus to analyze nonlinear fluid-structure interaction in dynamic environments. A novel approach for a 1-D hydraulic vibration exciter was proposed by Faming et al. [147], in which the rotary motion of a spool oriented its land grooves and windows on the sleeve, and thereby alternated the hydraulic flow into and out of the hydraulic cylinder chambers.

However, their findings showed that the system had limited frequency bandwidth due to its restricted valve linear opening area.

In the electrohydraulic vibration exciter presented by Zibin et al. [150], to enhance the amplitude of the vibration exciter, the researchers used a novel bi-directional digital valve capable of providing large output force and displacement amplitudes. Their approach had a simple configuration, demonstrated a high frequency response, and was robust against hysteresis Jia et al. [163] developed a four-axis, 2-D structural fatigue test system including four electrohydraulic vibration exciters. Their system operated in a frequency range of 5-200 Hz, and functioned based on the concept of an acting cylinder and a bias control servo valve. A dual-resonant structure vibration testbed was used by Li et al. [164] for vibration energy harvesting in a random frequency environment. The unidirectional vibration exciter was used to generate vertical excitations. It was shown that, as the vibration frequency varied, two proof masses in the harvester collided together and provided a strong coupling. Another unidirectional exciter was developed by Ju et al. [165] to test a vibration energy harvester which had a magneto-electric laminate composite [166, 167], [168] as well as a spring-less spherical permanent magnet as a proof mass. In their work, a proof-of-concept harvester was fabricated and characterized at various input accelerations and frequencies. Vibration exciter machines are also used to calibrate and validate various aspects of accelerometers and vibration sensors such as sensitivity, frequency response characteristics, and linearity [169-171].

Another application of vibration analysis is in the modal analysis for quality assurance called Acoustic Resonance Testing (ART). ART is a non-destructive test that uses the vibrational characteristics of an object to find defects. Using ART, one relies upon the fact

that the defect inside a physical structure has a distinct and unique set of characteristic frequencies [172, 173]. For instance, ball bearing fault segmentation at different time steps is important to avert failure. Mohanty et al. [174] studied the vibro-acoustic characteristics of ball bearings using wavelet-based multi-scale principal component analysis in order to extract the frequency range of the ball bearings operation along tangential, axial, and radial direction of the bearing.

Most vibration exciters used in engineering laboratories are only capable of 1-D excitations. However, ambient vibration sources (mechanical/acoustic) are typically available in 3-D coupled/uncoupled states. For example, when a bridge is exposed to a wind blow, or during an earthquake, the bridge's mechanical components (e.g., joints and links) vibrate in all possible directions. Hence, to understand the behavior of the bridge components and validate their performance, it is vital to test the components under various coupled 3-D vibrations rather than only unidirectional ones. Similar applications can be found in other domains such as vehicle shock absorbers [175], vibration-based energy harvesters [165], and life expectancy of electric components in the presence of vibration [176].

In this work, a 3-D Acousto Electrodynamic Vibration Exciter, AEVE 3D, is presented which is capable of uni- or multi-directional (i.e., 1-D, 2-D, and 3-D), coupled/uncoupled vibration excitations. Another novel feature of this apparatus is its ability to generate both acoustic and mechanical excitations in one unified framework. The proposed device is designed as a laboratory apparatus mainly to study dynamic behaviors of various devices and prototypes under mechanical and/or acoustic vibrations. AEVE 3D incorporates three electromagnetic shakers to generate mechanical excitations

in three Cartesian coordinate axes, and three loudspeakers to apply acoustic excitations. A main control unit was developed to individually command and drive these six actuators (i.e., shakers and loudspeakers) at various frequencies. The electronic unit included micro-controllers and a signal conditioning and amplification stage. Furthermore, a graphical computer application was designed to communicate with the microcontrollers through USB protocol, and set the desired frequencies for each actuator. Finally, two different piezoelectric vibration sensors (one commercial and one custom-made in house) were employed to validate the performance and effectiveness of AEVE 3D. Compared to the existing apparatus available in the market and lab-made systems, the contributions of this works are as follows.

A) AEVE 3D is capable of providing coupled or uncoupled uni- or multi-directional vibrations.
B) AEVE 3D enables simultanous 3-D acoustic and 3-D mechanical vibration tests.
C) AEVE 3D has a high mechanical frequency range of up to 2 kHz and high acoustic vibration frequency range of up to 6 kHz in all 3 directions in both coupled and decoupled forms.

6.3 **Model design**

Figure 6.1 depicts the architecture of AEVE 3D including its main units including a user operating panel, a main control unit, and a mechanical unit. The operating panel is basically a graphical user interface (GUI) that allows the user to set the desired frequencies for each individual actuator. This GUI receives the experiment parameters from the user and transmits them to the main electronic unit through USB ports. The electronic unit,

subsequently, constructs six sinusoidal waveforms with the given frequencies. An amplification stage then amplifies the waveforms and feeds them to the shakers and loudspeakers. The mechanical unit is then responsible for translating these electrical oscillations to independent mechanical and acoustic vibrations at the vibration tray. In the following sections, these units are explained in further detail.

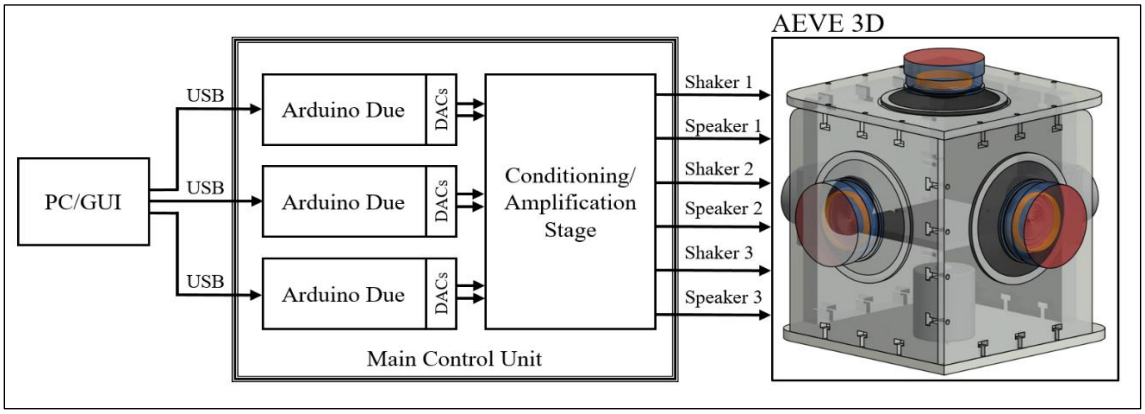

Figure 6.1: AEVE 3D's overall architecture

6.3.1 Mechanical Unit

The mechanical unit of AEVE 3D is shown in Figure 6.2, which includes three electromagnetic shakers (Bruel and Kjaer permanent magnet vibration exciter, LDS V201, with peak sine force ratings of 17.8 N). These shakers are attached to three frame walls of the test setup along three Cartesian axes (-ve x, -ve y, and -ve z), to generate unidirectional mechanical excitations along the respective directions. Additionally, to generate acoustic vibrations, the mechanical unit incorporates three loudspeakers (6.5-inch dual cone 80-Watt Boss Audio System loudspeakers with a frequency response of up to 18 kHz and Impedance of 4 Ohms) in the three opposite frame walls along the Cartesian axes.

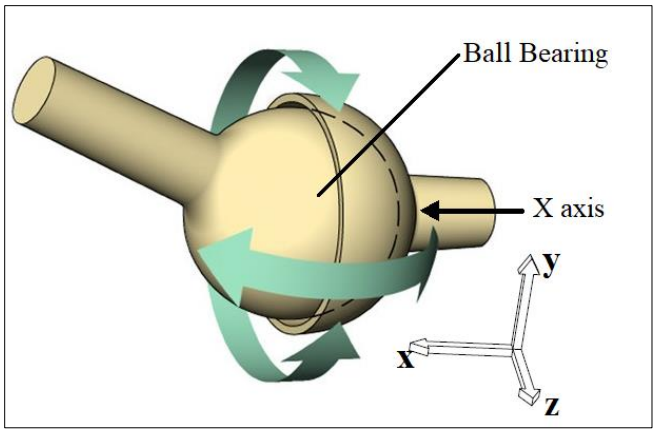

Figure 6.2: Movement of ball and socket joint in the y-z plane.

At the middle of the apparatus, a flat movable platform is installed where the test device is mounted. The platform is attached to the mechanical shakers via three ball-and-socket joints (BSJs). BSJs can provide a rotational movement around its ball bearing center. This rotational movement takes place in each specific plane (e.g., y-z plane in Figure 6.3) which is perpendicular to the base/socket movement direction (e.g., x axis in Figure 6.3). Hence, an object attached to a BSJ has the flexibility to move along all three Cartesian axes.

The BSJs' socket links are connected to the shakers' output pins, while the ball segments are attached to the movable platform (Figure 6.3). If only one of the shakers is in operation, the platform vibrates along the excitation direction, while the BSJs attached to other shakers allow the platform to move freely with negligible alteration of the movement direction. The platform's motion profile can be determined by the phase of the harmonic excitations. With two shakers in synchronized operation, the BSJ enables a planar elliptical/circular movement for the platform. Similarly, with three synchronized shakers in operation, an elliptical/circular trajectory in 3-D space can be achieved. Using the BSJs, various unidirectional/uncoupled and multidirectional/coupled motion profiles can be

realized. Since the acoustic excitation amplitude is quite negligible compared to the mechanical one, the BSJs are independent of the acoustic portion of the system.

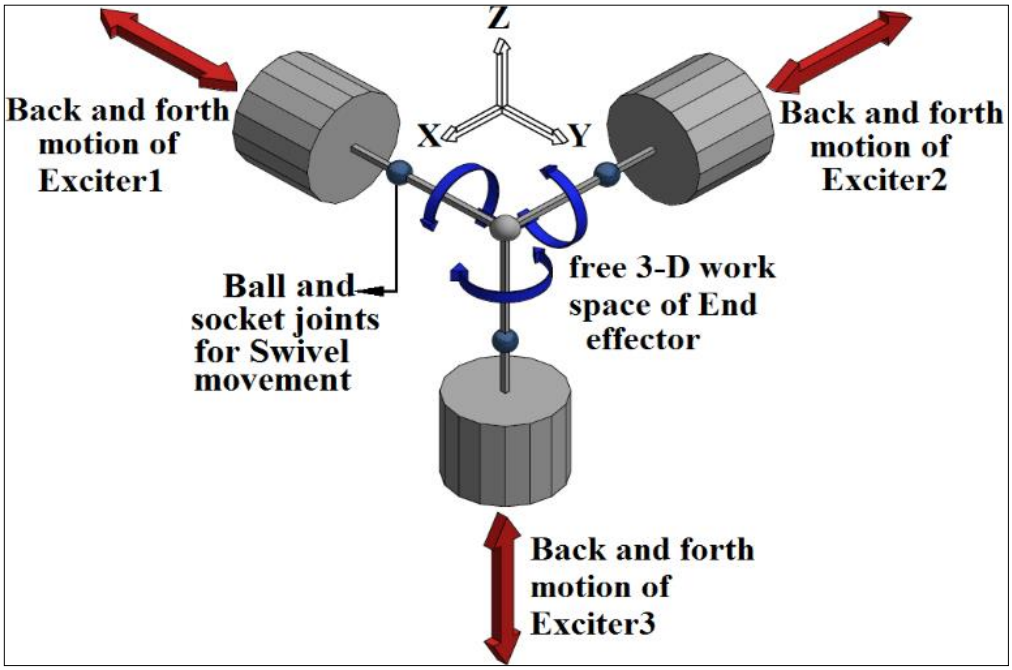

Figure 6.3: Ball-and-socket joints and the resultant workspace.

In the BSJs, some geometric nonlinearity arises at larger displacements due to the mechanical contacts. The current form of AEVE 3D only allows for small-to-medium displacement amplitudes (arms' displacement of the BSJs is less than 2 mm), where the nonlinearity effect is negligible. This phenomenon makes the vibration testbed more suited for applications such as energy harvester testing where the frequency content of the system is of higher interest. To mitigate this problem, one can use larger BSJs which minimize the nonlinear behavior and accommodate larger, linear displacements. In our analyses, nonlinearity was not investigated or accounted for. The nonlinearity and its effect on force-displacement relationship will be investigated in future work.

6.3.2 Control Unit

AEVE 3D consists of three shakers and three speakers which are connected in three Cartesian directions, as shown in Figure 6.4. Sinusoidal signals from a signal generator are fed to all six exciters through an amplifier to amplify the excitation amplitude.

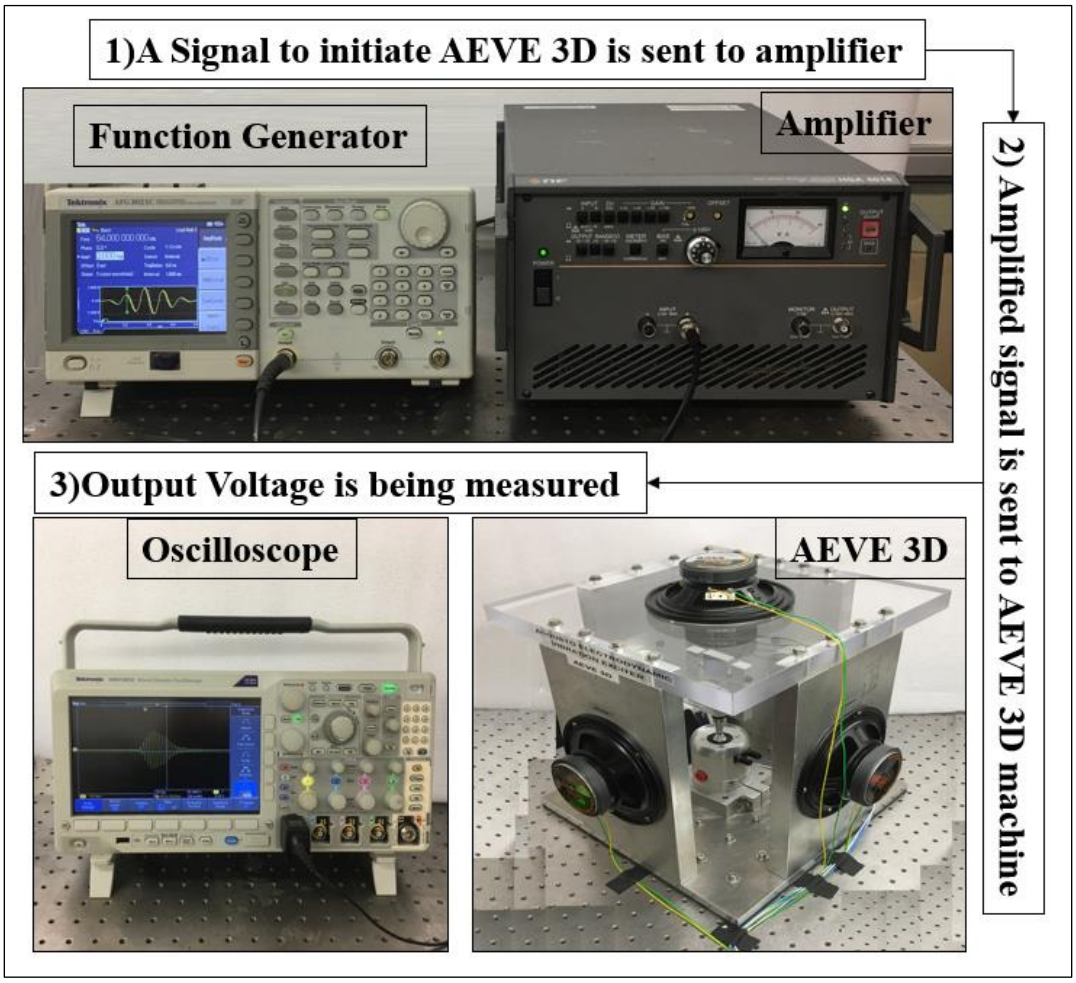

Figure 6.4: The overall architecture of the main control unit and testing section in coupled mode.

At first, as shown in Figure 6.5, all the exciters stimulated the specimen with the same frequency and phase in all directions as a coupled excitation motion, while the specimen's vibration was measured (i.e., the output voltage of some piezoelectric vibration sensors as discussed later on).

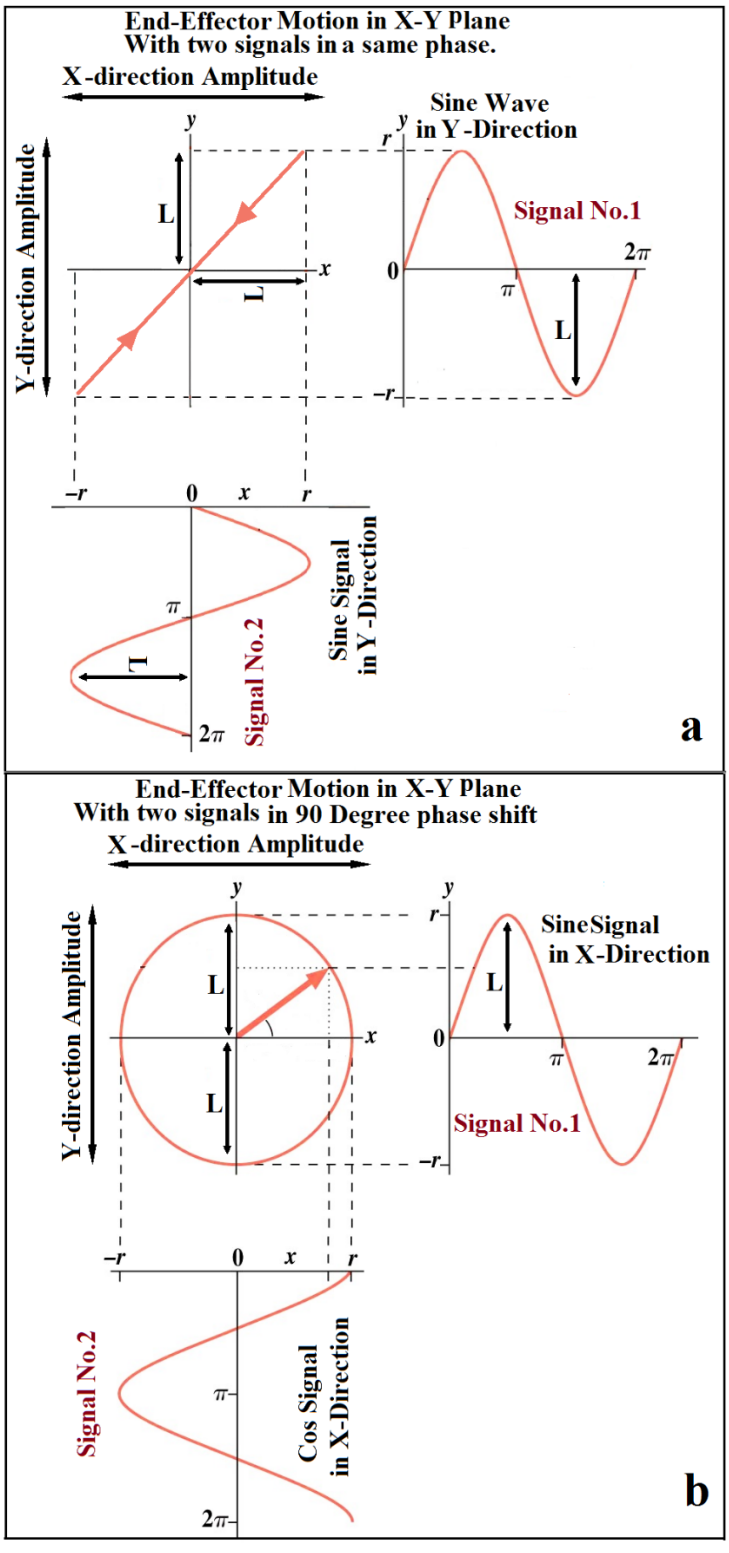

Figure 6.5: The reciprocating motion of the end-effector (a) when two sinusoidal signals have the same phase, and (b) when two signals have π/2 phase shift

In this section, the coupled excitation motion means that AEVE 3D vibrates the specimen mounted on the movable platform with the same frequency in all Cartesian directions, as all the exciters and speakers are fed with a same signal from the signal generator. However, to provide a controlled coupled (2-D and 3-D) and decoupled (1-D) motion of the end-effector, a separate electronic unit was introduced which included a six-channel signal generator and six-channel amplifier.

The six-channel signal generator was developed using three Arduino Due microcontrollers. The Arduino Due, which is based on a 32-bit ARM core microcontroller, was selected as it has two programmable digital-to-analog converters (DACs). Each microcontroller was programmed to generate two sinusoidal signals with adjustable frequencies using the two DACs. Each microcontroller was assigned to one shaker and speaker along one Cartesian axis.

To achieve the largest displacement of the end-effector in unit of time, the signals fed to each mechanical exciter must be accurately calculated and set. Figure 6.6 illustrates the end-effector's motion in the x-y plane with two input sinusoidal waveforms. Figure 6.6a shows the end-effector's reciprocating motion when the input signals fed to the x- and y-axis exciters have an amplitude of L and the same phase. Such scenario brings about a linear motion trajectory. Figure 6.6b, on the other hand, shows the end-effector motion trajectory in the x-y plane when the signals fed to the shakers have a $\pi/2$ phase difference. This scenario causes a circular motion of the end effector on the x-y plane. In 3-D space, through fine-tuning of the signals fed to the actuators and their relative phase, a circular motion of the end-effector can be produced.

Assuming the mechanism with the two horizontal exciters generating planar motion, the position and velocity vectors of the center of the platform can be written as:

$$\vec{\boldsymbol{p}} = \begin{bmatrix} A\sin(\omega t) \\ A\sin(\omega t + \theta) \end{bmatrix} \tag{6-1}$$

$$\vec{\boldsymbol{v}} = \begin{bmatrix} A\omega\cos(\omega t) \\ A\,\omega\cos(\omega t + \theta) \end{bmatrix} \tag{6-2}$$

Magnitude of the velocity, $|\vec{\boldsymbol{v}}|$, and its average, $\bar{v}$, can be computed as follows:

$$|\vec{\boldsymbol{v}}| = A\omega\sqrt{\cos^2(\omega t) + \cos^2(\omega t + \theta)} \tag{6-3}$$

$$\bar{\boldsymbol{v}} = \frac{\omega}{2\pi}\int_0^{\frac{2\pi}{\omega}} |\vec{\boldsymbol{v}}|\ dt \tag{6-4}$$

Considering $\theta = \frac{\pi}{2}$, then $|\vec{\boldsymbol{v}}|$ will have constant amplitude of $A\omega$, and $\bar{v}$ will be maximized:

$$|\vec{\boldsymbol{v}}| = \bar{v} = A\omega \tag{6-5}$$

For other values of θ, the value of $|\vec{\boldsymbol{v}}|$ changes with time. For example, at $\theta = 0$,

$$|\vec{\boldsymbol{v}}| = \sqrt{2}A\omega\cos(\omega t) \tag{6-6}$$

$$\bar{\boldsymbol{v}} = \frac{2\sqrt{2}A\omega}{\pi} \approx 0.9A\omega \tag{6-7}$$

Now considering the full mechanism with three exciters, the position vector can be written as:

$$\vec{\boldsymbol{p}} = \begin{bmatrix} A\sin(\omega t) \\ A\sin(\omega t + \theta_1) \\ A\sin(\omega t + \theta_2) \end{bmatrix} \tag{6-8}$$

Considering $\theta_1 = \frac{2\pi}{3}$ and $\theta_2 = -\frac{2\pi}{3}$, $|\vec{\boldsymbol{v}}|$ will have constant value, and $\bar{v}$ will be maximized:

$$|\vec{\boldsymbol{v}}| = \bar{v} \approx 1.22\, A\omega \tag{6-9}$$

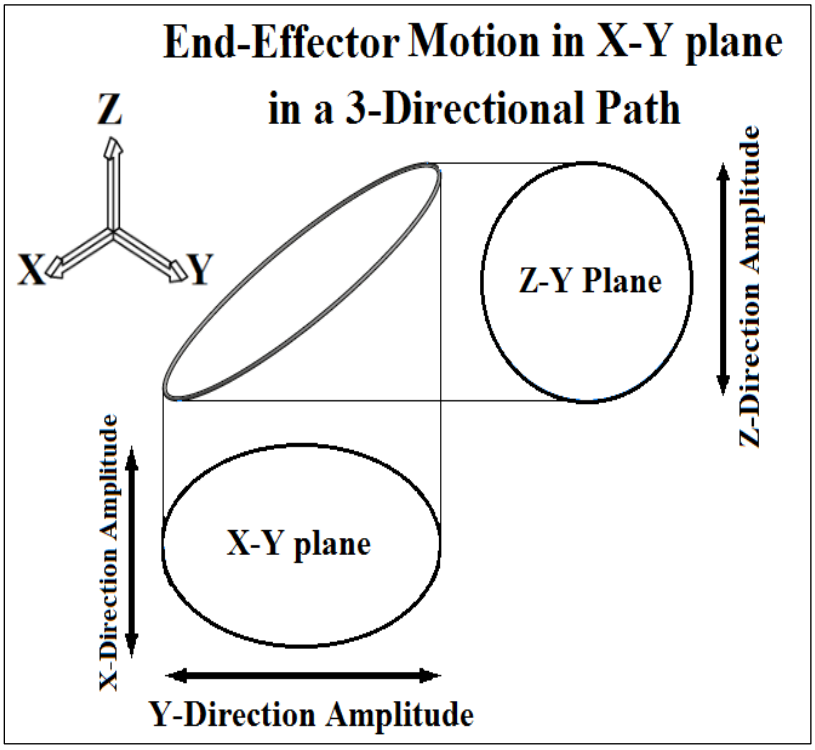

Figure 6.6: The 3-D motion of end-effector when three sinusoidal signals are fed to the shakers.

The signals constructed by the Arduino DACs are not nearly powerful enough to drive the speakers and shakers. Therefore, amplification of these signals is required to strengthen the generated sine waves and feed the actuators. To address the need, a 6-channel amplification stage was designed as an interface between the microcontrollers and the shakers/speakers. The amplification board consisted of three high-quality stereo amplifiers

each of which employed an STA540 power amplifier IC from STMicroelectronics at its heart. In its dual-channel configuration, the IC is capable of driving two four-ohms 38-watt speakers/shakers. The six signals from the Arduino Dues first underwent six bandpass audio filters (to precondition and remove the DC components) and then were input to the six channels of the amplification board.

6.3.3 Operating Panel

A desktop GUI as shown in Figure 6.8, was developed using MATLAB programming language, which receives the desired frequencies from the user and then communicates with the three microcontrollers through USB ports. Upon receipt of the desired frequencies, each microcontroller produces two sinusoidal signals with the set frequency using its internal clock and the math library. The internal clock of Arduino Due keeps tracks of the time elapsed since the microcontroller comes on. Using this clock, the desired frequencies, and the math library, Arduino Due computes and outputs two sine waveforms on its DACs. AEVE 3D features a high mechanical frequency range of up to 2kHz and high acoustic frequency range of up to 6kHz in all three directions in both coupled and decoupled scenarios.

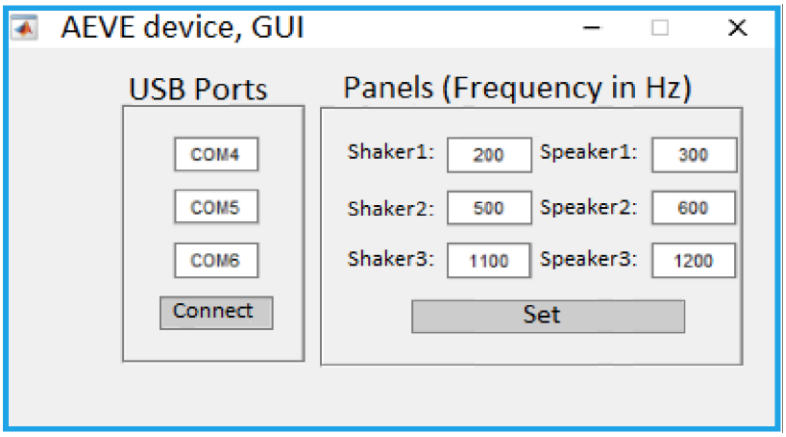

Figure 6.7: AEVE 3D's operator panel GUI.

6.4 Experimental Validation of the Machine

AEVE 3D was fabricated in the iMAPS laboratory of University of South Carolina, USA. A square box frame was constructed to hold the mechanical and acoustic exciters in the Cartesian coordinate system. The frame was made of 1" thick hard acrylic and aluminum sheet in order to have a firm and stable setup. While only the bottom (-ve z) mechanical exciter is screwed to the base of the frame, other vibration sources were clamped with the frame via several bolts. Finally, the movable platform, for holding different specimens, was connected to the exciters through BSJs.

6.4.1 Testing for Electro-Dynamic Mechanical Excitation

To validate the proposed 3-D vibration exciter, an arrangement of three piezoelectric cantilever energy harvesters (from Mouser Electronics Company, Mide Energy Harvester Modules with dimensions of 54.4 mm x 22.4 mm x 0.46 mm and resonance frequency of 130 Hz) was used as the testing sample. In the arrangement, three identical cantilever energy harvesters were connected in a tree style as shown in Figure 6.9. This tree-style harvester was mounted on AEVE 3D's movable platform and vibrated in both coupled and decoupled modes, while the harvester's output voltage was measured and collected.

Initially, the test specimen was excited in three separate experiments of unidirectional mode along Cartesian axes. In these experiments, even though all three cantilever harvesters were excited, it was expected to get a significant response only from the cantilever perpendicular to the excitation axis. The goal of these experiments was to validate the testbed's performance for unidirectional vibration by comparing the manufacturer's specified resonance frequency and maximum voltage output frequency.

Ideally, these frequencies should be in close agreement. Upon validation of the testbed for unidirectional excitation, the testbed's performance was investigated for coupled 3-D excitation. In order to inspect reliability of the developed system and calculate its uncertainty range, each experiment was carried out 10 times. For any cantilever beam, the first natural frequency always remains the same, irrespective of any mode of excitation [177]. Hence, for both unidirectional and multi-directional excitation, the maximum power output should be obtained at the first resonance frequency of the beam. However, while for unidirectional excitation a sharp voltage output peak can be found at the resonance frequency, a slightly wider peak is expected for multi-directional coupled excitation due to development of polarization and dipole moment in the other two directions.

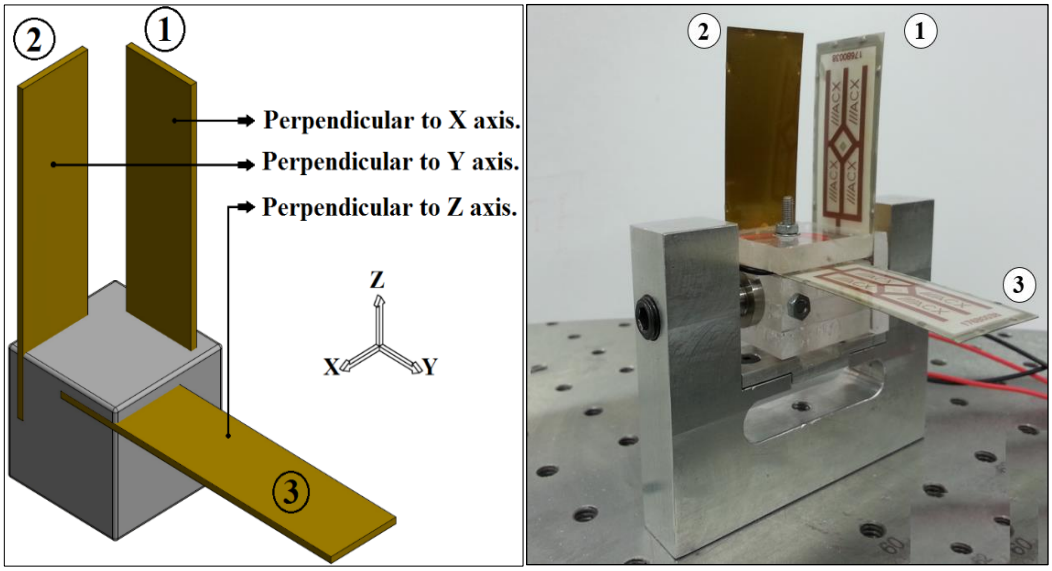

Figure 6.8: 3-D piezoelectric cantilever beam energy harvester tree test system.

6.4.2 Testing for Acoustic Excitation

To investigate the ability of the testbed to simulate an acoustic vibration environment, the same test specimens cannot be used due to its high stiffness. A low-stiffness cantilever structure is required to show a reasonable response to low acoustic pressure variations.

Hence, a Lead-Zirconate-Titanate (PZT-5H) cantilever structure was designed and fabricated in the iMAPS laboratory based on the acoustic frequency generation capacity of the speakers in AEVE 3D. The designed cantilever consisted of a thin PZT-5H strip sandwiched between two plastic encapsulants. A COMSOL Multiphysics numerical simulation was performed to obtain the required geometry of the cantilever structure. Simulation results indicated that the modeled cantilever beam, with a 23 mm length, 5 mm width, and 150 μm thickness, has its first natural frequency at 147.3 Hz.

6.5 Experimental Results

Three sets of experiments, each repeated 10 times, were performed to excite the specimen along three Cartesian directions. Results of the unidirectional mechanical excitation experiments are depicted in Figure 6.11. This figure shows the mean values of the output voltage from all three harvesters for x-, y- and z-directions along with the output error bound from the cantilever energy harvester in the tree-style structure. According to these results, it is evident that the system's behavior is highly repeatable and that AEVE 3D features a low uncertainty band. A normal distribution curve was first obtained at each frequency response from all 10 experiments, and then 95% confidence interval was calculated. In Figure 6.9, the gray envelopes represent the aforementioned confidence interval. A number of factors may contribute to this uncertainty such as human error, slippage of the BSJs used in the system, ambient temperature, and gradual degradation in the functionality of the cantilever beams. However, it was observed that the frequencies at which the peak responses occur are highly consistent across experiments although the amplitudes may show minor variability.

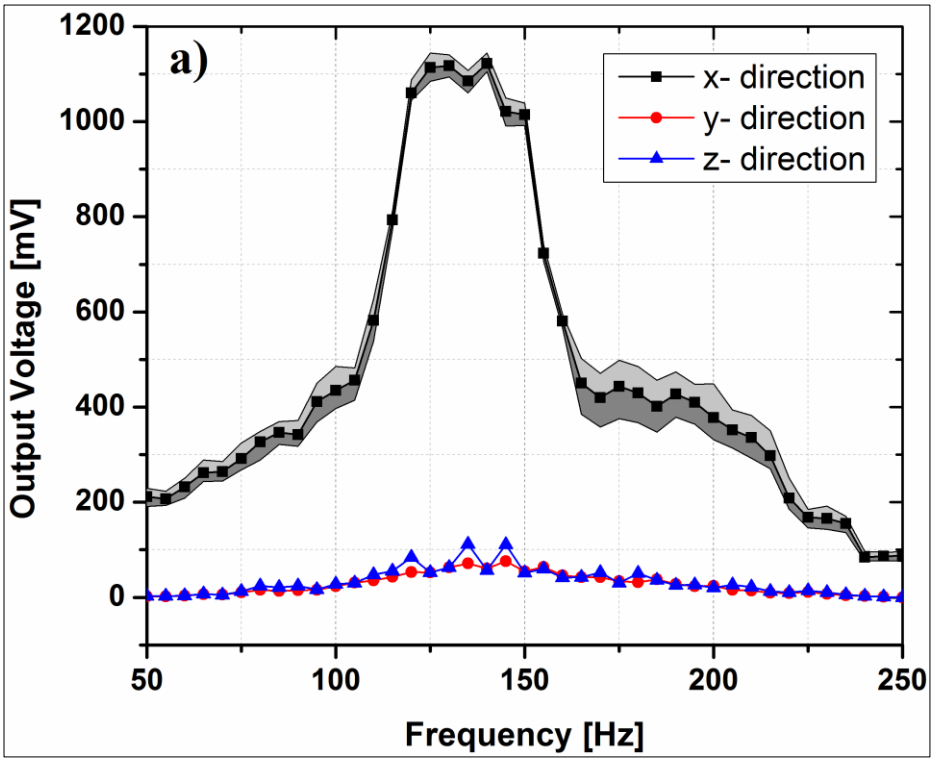

(a)

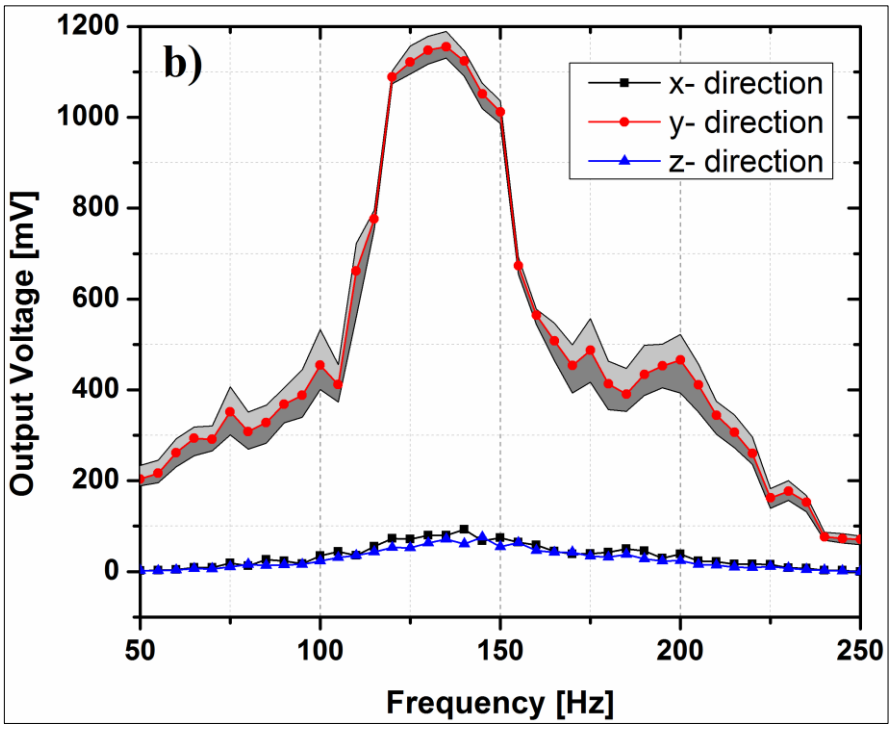

(b)

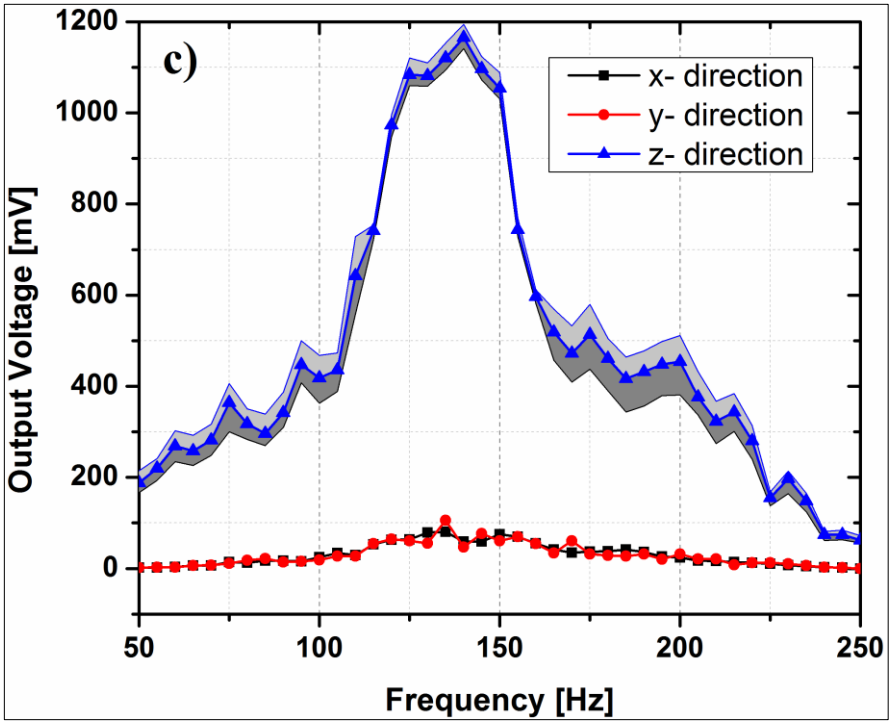

(c)

Figure 6.9: The output voltage from all three harvesters for excitations in a) x- direction, b) y- direction, and c) z-direction.

The established literature says that a cantilever harvester provides its maximum energy at the first resonance frequency [177]. Here, experimental results confirm that at any unidirectional excitation, this resonant response can be found only from the harvester perpendicular to the excitation axis. As expected, the responses from the other two harvesters are negligible. It can also be seen that the maximum voltage is achieved at ~130 Hz for all the harvesters, which agrees with the harvesters' first natural frequency (130 Hz) specified by the manufacturer.

Subsequently, the tree-style energy harvester was tested for 3-D coupled excitation. In order to avoid clutter and maintain readability of the graph, only the mean values, averaged from the collected data during 10 repeated experiments, are shown in Figure 6.10. It can

be observed that all the cantilever harvesters show similar responses and, expectedly, their highest output voltages occur at the first natural frequency.

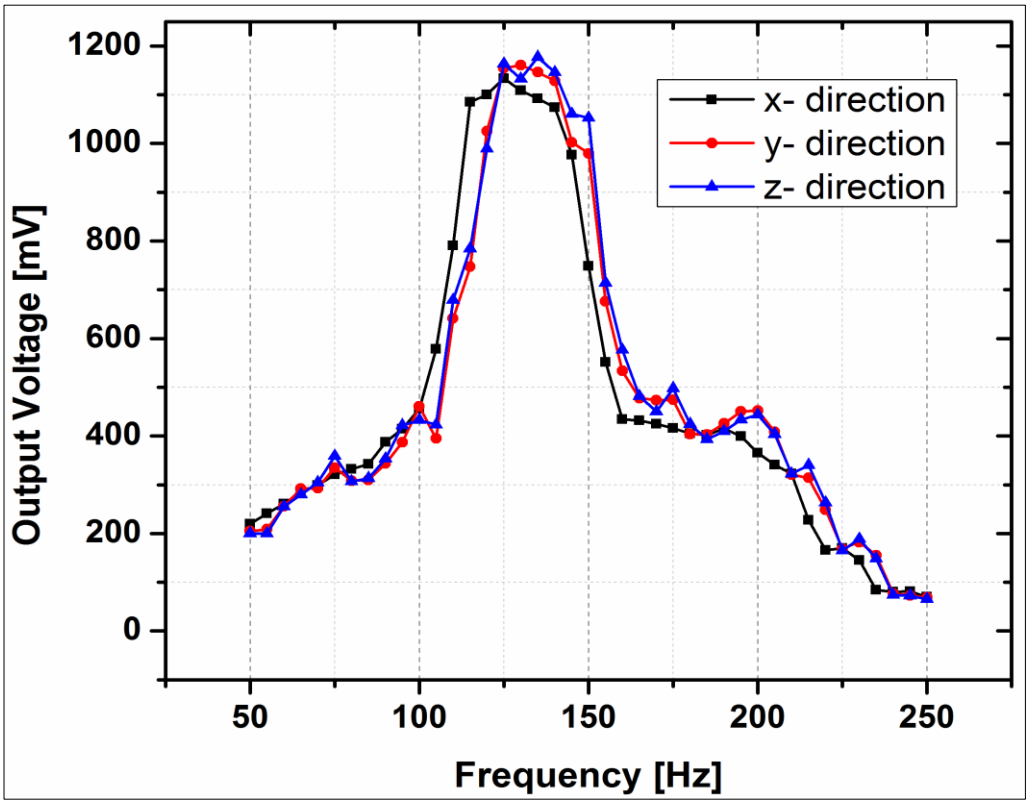

Figure 6.10: The voltage output from the tree-style cantilever energy harvesters with a 3-D coupled mechanical excitation.

Importantly, although for unidirectional excitation a reasonably sharp voltage peak was observed around 130 Hz for each harvester, a relatively wider band (120–140 Hz) is obtained for 3-D coupled excitation due to the development of polarization and dipole moment [177]. The output response from the cantilever tree in Figure 6.10, verifies the established literature [178] and confirms the ability of the testbed to provide coupled mechanical excitations. In addition to the widened bandwidth of the energy harvester, this figure reveals another aspect of coupled excitations over uncoupled ones. The measured output voltage from each cantilever beam in coupled excitation mode is a bit larger

compared to the unidirectional uncoupled excitation mode (Table. 6.1). For example, the average output voltage of the cantilever beam in x-axis excitation in the decoupled mode is 1121.9 (mV) while in the coupled mode is 1136.8 (mV). This shows a 1.3% improvement of output voltage in the coupled vibration scenario. A similar phenomenon is also observed for y- and z-directions where 1.4% and 1.7% improvements are observed, respectively.

Table 6.1: Average output voltage in response to 1-D and 3-D excitations in the frequency range of 120-140 HZ

Cantilever	Average output voltage[mV] in Unidirectional Excitation (Fig.10)	Average output voltage[mV] in Coupled Excitation (Fig.11)	Improvement
1	1121.9	1136.8	1.33%
2	1155.2	1170.9	1.36%
3	1165.8	1185.3	1.67%

According to the ISO GUM [179], measurement uncertainty is evaluated by Type-A and Type-B methods. The Type-A method is the evaluation of standard uncertainty via statistical analysis of the experimental observations, while uncertainties based on normal distributions constitute Type B if they are not the result of our own measurement data [180]. Figure 6.11 illustrates the type-A standard uncertainty of our own obtained results. According to this figure, the uncertainties evaluated adjacent to the sensor's resonance frequency (120-140 Hz) are less than 1%.

In the next step, AEVE 3D was examined for its acoustic excitation performance. As discussed in Section III, in this round of experiments, instead of the tree-style energy harvester, a 1-D cantilever beam was employed. For acoustic performance verification, only unidirectional excitations were examined using a single cantilever specimen. In each

experiment, cantilever beams were placed perpendicular to the excitation axis. Since it is challenging to analytically compute the natural frequency of the developed cantilever beam, a COMSOL Multiphysics simulation was performed to find the first resonance frequency. The simulation results indicated a resonance frequency of 147.3 Hz for the sandwiched beam. The experimental results obtained via acoustic excitation of the low-stiffness beam, independently excited in each Cartesian direction, are depicted in Figure 6.11. This figure shows the mean values of the output voltage across 10 repeated experiments. As evident in this figure, the maximum frequency (i.e., ~145 Hz) closely matches the first resonance frequency of the beam calculated through COMSOL simulation (i.e., 147.3 Hz).

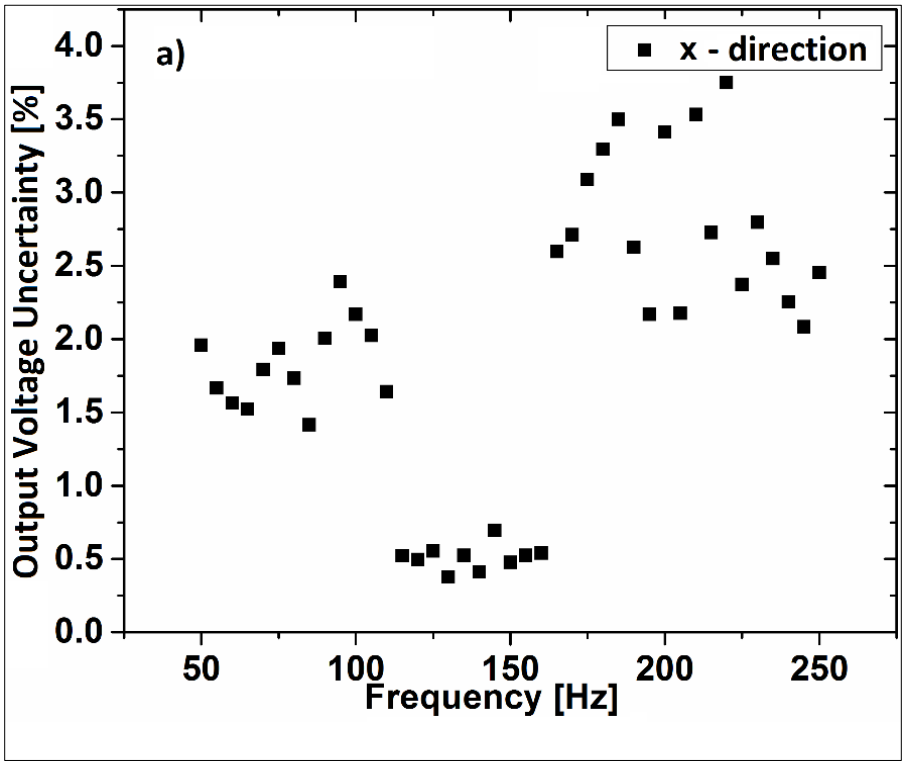

(a)

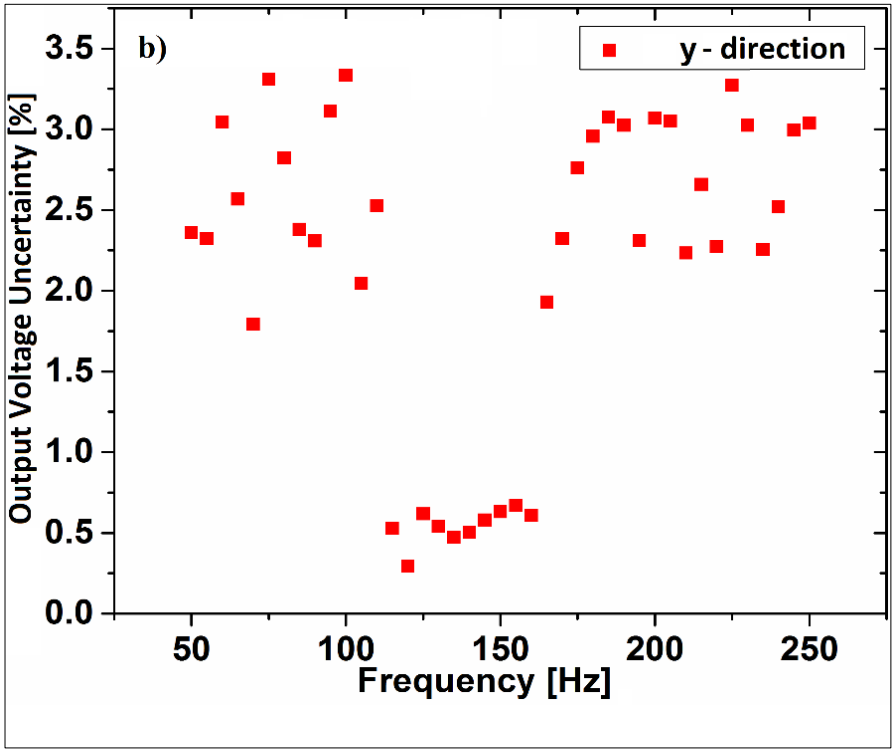

(b)

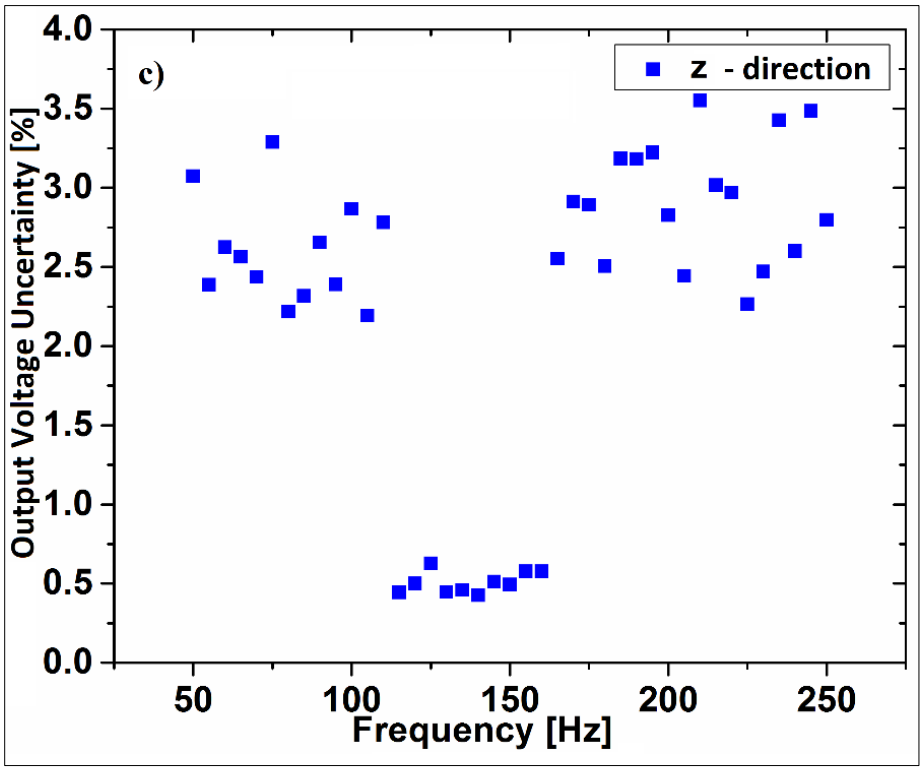

(c)

Figure 6.11: The type-A standard uncertainty of obtained results for corresponding excitations of Figure 6.11 in a) x-direction, b) y-direction, and c) z-direction.

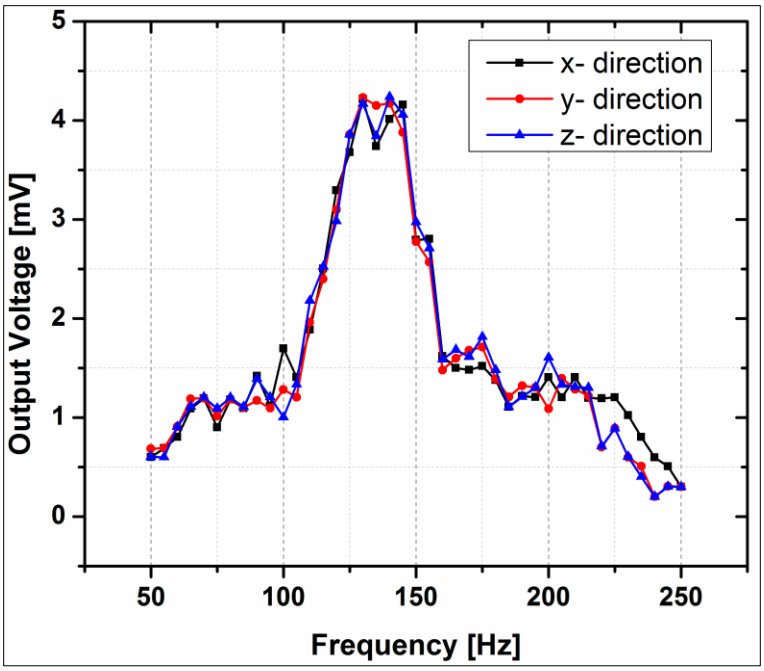

Figure 6.12: The output voltage from the 1-D cantilever beam with three individual unidirectional acoustic excitations in x-, y-, and z-directions, when the beam was placed perpendicular to the axis of excitation.

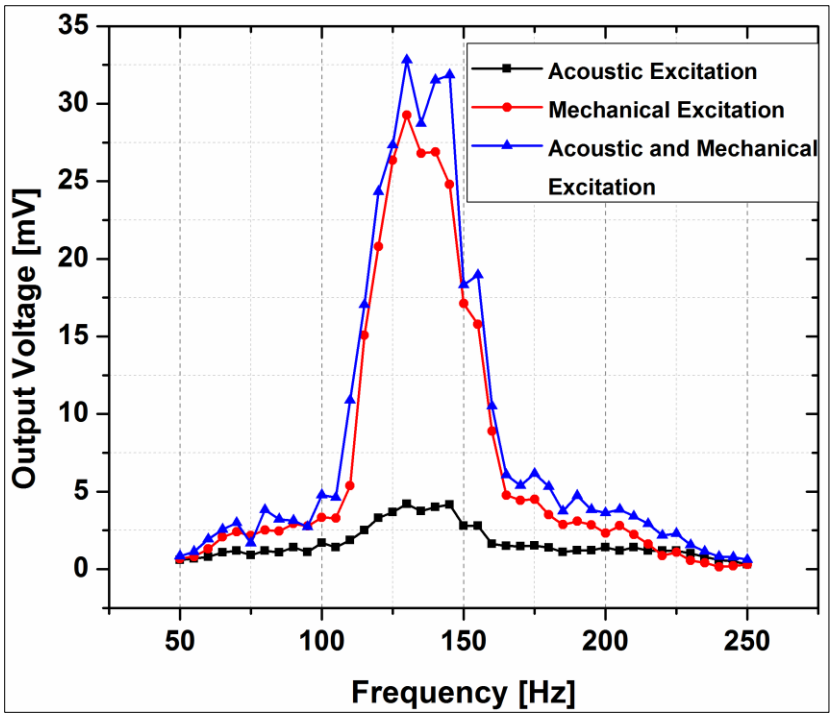

Figure 6.13: Output voltage of the 1-D cantilever beam in response to unidirectional i) mechanical vibrations (red), ii) acoustic vibrations (black), and iii) both mechanical and acoustic excitations combined (blue).

Expectedly, acoustic excitation generates much smaller output voltage as compared to its mechanical vibrations which is due to lower displacement amplitudes induced. The output voltage of the harvesters not perpendicular to the excitation directions were in the nV range, and, hence, are not shown in Figure 6.11.

Finally, AEVE 3D's performance was examined in the presence of individual and combined acoustic and mechanical excitations. In this round of experiments, the single sandwiched cantilever was used, and for the sake of simplicity, only unidirectional excitations are reported here. In each experiment, the cantilever beam was placed perpendicular to the axis of excitation. Figure 6.13 shows the mean values of 10 repeated experiments in three different conditions of i) mechanical excitation, ii) acoustic excitation, and iii) combined mechanical and acoustic excitations. According to this figure, all three conditions demonstrate resonance frequencies around 145 Hz, which is in accordance with the COMSOL simulation results. Expectedly, the output voltage generated due to acoustic

Excitation is much smaller as compared to the mechanical excitation, which is due to smaller displacement induced by air pressure variations. Figure 6.13 also shows that the output voltage of the cantilever beam is largest in the presence of both mechanical and acoustic excitations combined.

6.6 Chapter Conclusion

The current chapter presented AEVE 3D, Figure 6.14, which is a tri-axial acoustic electro-dynamic vibration exciter. Vibration exciters are traditionally used in engineering laboratories for dynamic analysis and characterization of devices, sensors, and instruments. Traditionally, unidirectional vibration testbeds have been used to simulate vibrating

physical environments. To prepare a more naturalistic vibration environment, AEVE 3D allows both mechanical and acoustic vibrations involving uni- or multidirectional vibrations. For the mechanical and acoustic excitations, electro-dynamic shakers and loudspeakers were utilized, respectively. A main control unit was developed which consisted of microcontrollers and a signal conditioning/amplification stage. A MATLAB GUI was designed which allows the user to easily connect to the hardware unit and set the desired frequencies for each of the six actuators. The performance of the testbed was verified against a tree-style energy harvester developed with commercial piezoelectric cantilever beams as well as a custom-made low-stiffness harvester.

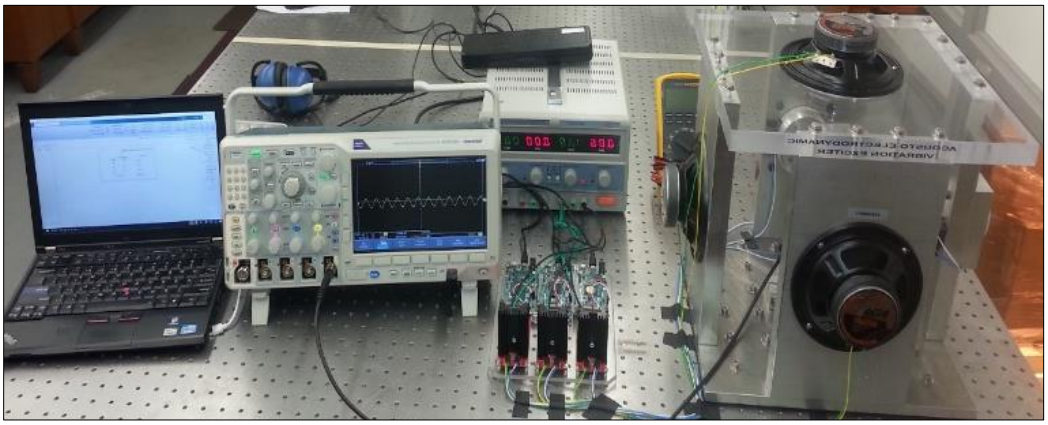

Figure 6.14: Three-Dimensional Acousto Electro-dynamic Vibration Exciter

REFERENCES

[1] Z. Gong *et al.*, "High-sensitivity Fabry-Perot interferometric acoustic sensor for low-frequency acoustic pressure detections," *Journal of Lightwave Technology*, vol. 35, no. 24, pp. 5276-5279, 2017.

[2] P. K. Tam and K. T. Wong, "Cramer-Rao bounds for direction finding by an acoustic vector sensor under nonideal gain-phase responses, noncollocation, or nonorthogonal orientation," *IEEE Sensors Journal*, vol. 9, no. 8, pp. 969-982, 2009.

[3] M. M. Indaleeb, S. Banerjee, H. Ahmed, M. Saadatzi, and R. Ahmed, "Deaf band based engineered Dirac cone in a periodic acoustic metamaterial: A numerical and experimental study," *Physical Review B*, vol. 99, no. 2, p. 024311, 2019.

[4] M. Saadatzi, F. Mir, M. N. Saadatzi, V. Tavaf, and S. Banerjee, "Modeling of a 3D acoustoelastic metamaterial energy harvester," in *Active and Passive Smart Structures and Integrated Systems XII*, 2018, vol. 10595, p. 105952U: International Society for Optics and Photonics.

[5] M. Goodarzi, M. N. Bahrami, and V. Tavaf, "Refined plate theory for free vibration analysis of FG nanoplates using the nonlocal continuum plate model," *Journal of Computational Applied Mechanics*, vol. 48, no. 1, pp. 123-136, 2017.

[6] F. Mir, M. Saadatzi, R. U. Ahmed, and S. Banerjee, "Acoustoelastic MetaWall noise barriers for industrial application with simultaneous energy harvesting capability," *Applied Acoustics*, vol. 139, pp. 282-292, 2018.

[7] F. Mir, M. S. Saadatzi, R. U. Ahmed, and S. Banerjee, "The possibility of harvesting electrical energy from industrial noise barriers using meta-wall bricks," in *Sensors and Smart Structures Technologies for Civil, Mechanical, and Aerospace Systems 2018*, 2018, vol. 10598, p. 105982S: International Society for Optics and Photonics.

[8] M. Saadatzi, F. Mir, M. N. Saadatzi, and S. Banerjee, "Modeling and Fabrication of a Multi-axial Piezoelectric Energy Harvester based on a Metamaterial-inspired Structure," *IEEE Sensors Journal*, 2018.

[9] S. Shrestha, V. Tavaf, and S. Banerjee, "Help-A framework for computational nondestructive evaluation of degraded composites with microscale discontinuiti," *Materials Evaluation*, vol. 78, no. 1, 2020.

[10] H. Ahmed, R. Ahmed, and S. Banerjee, "Butterfly metamaterial for acoustic holographic imaging through superlensing capability (Conference Presentation)," in *Health Monitoring of Structural and Biological Systems XII*, 2018, vol. 10600, p. 1060019: International Society for Optics and Photonics.

[11] H. Ahmed, R. Ahmed, M. M. Indaleeb, and S. Banerjee, "Multifunction acoustic modulation by a multi-mode acoustic metamaterial architecture," *Journal of Physics Communications,* vol. 2, no. 11, p. 115001, 2018.

[12] H. Ahmed, M. M. Indaleeb, M. Saadatzi, T. Sain, S. Ghosh, and S. Banerjee, "Investigation of wave trapping and attenuation phenomenon for a high symmetry interlocking micro-structure composite metamaterial," in *Smart Structures and NDE for Energy Systems and Industry 4.0*, 2019, vol. 10973, p. 109730W: International Society for Optics and Photonics.

[13] D. Caballero *et al.*, "Large two-dimensional sonic band gaps," *Physical Review E*, vol. 60, no. 6, p. R6316, 1999.

[14] A. S. Phani and N. A. Fleck, "Elastic boundary layers in two-dimensional isotropic lattices," *Journal of Applied Mechanics,* vol. 75, no. 2, p. 021020, 2008.

[15] C. Chesnais, C. Boutin, and S. Hans, "Effects of the local resonance on the wave propagation in periodic frame structures: Generalized Newtonian mechanics," *The Journal of the Acoustical Society of America,* vol. 132, no. 4, pp. 2873-2886, 2012.

[16] M. Oudich, Y. Li, B. M. Assouar, and Z. Hou, "A sonic band gap based on the locally resonant phononic plates with stubs," *New Journal of Physics,* vol. 12, no. 8, p. 083049, 2010.

[17] J.-C. Hsu, "Local resonances-induced low-frequency band gaps in two-dimensional phononic crystal slabs with periodic stepped resonators," *Journal of Physics D: Applied Physics,* vol. 44, no. 5, p. 055401, 2011.

[18] A. Krynkin, O. Umnova, A. Yung Boon Chong, S. Taherzadeh, and K. Attenborough, "Predictions and measurements of sound transmission through a periodic array of elastic shells in air," *The Journal of the Acoustical Society of America,* vol. 128, no. 6, pp. 3496-3506, 2010.

[19] H. J. Hoffman, R. A. Dobie, K. G. Losonczy, C. L. Themann, and G. A. Flamme, "Declining prevalence of hearing loss in US adults aged 20 to 69 years," *JAMA otolaryngology–head & neck surgery,* vol. 143, no. 3, pp. 274-285, 2017.

[20] F. R. Lin, J. K. Niparko, and L. Ferrucci, "Hearing loss prevalence in the United States," *Archives of internal medicine,* vol. 171, no. 20, pp. 1851-1853, 2011.

[21] Makati Medical Center. (2019, August 13). *Everything About Noise-Induced Hearing Loss*. Available: https://www.makatimed.net.ph/news-and-exhibits/news/are-you-going-deaf

[22] D. Hajioff, "Cochlear implantation: a review of current clinical practice," *British Journal of Hospital Medicine,* vol. 77, no. 12, pp. 680-684, 2016.

[23] M. Harada, N. Ikeuchi, S. Fukui, H. Toshiyoshi, H. Fujita, and S. Ando, "Micro mechanical acoustic sensor toward artificial basilar membrane modeling," *IEEJ Transactions on Sensors and Micromachines,* vol. 119, no. 3, pp. 125-130, 1999.

[24] S.-H. Shen, S.-T. Young, and W. Fang, "Design and fabrication of a MEMS filter bank for hearing aids applications," in *2nd Annual International IEEE-EMBS*

Special Topic Conference on Microtechnologies in Medicine and Biology. Proceedings (Cat. No. 02EX578), 2002, pp. 352-355: IEEE.

[25] K. Tanaka, M. Abe, and S. Ando, "A novel mechanical cochlea" Fishbone" with dual sensor/actuator characteristics," *IEEE/ASME transactions on mechatronics*, vol. 3, no. 2, pp. 98-105, 1998.

[26] T. Xu, M. Bachman, F.-G. Zeng, and G.-P. Li, "Polymeric micro-cantilever array for auditory front-end processing," *Sensors and Actuators A: Physical*, vol. 114, no. 2-3, pp. 176-182, 2004.

[27] F. Battiston *et al.*, "A chemical sensor based on a microfabricated cantilever array with simultaneous resonance-frequency and bending readout," *Sensors and Actuators B: Chemical*, vol. 77, no. 1-2, pp. 122-131, 2001.

[28] A. Moulin, S. O'shea, and M. E. Welland, "Microcantilever-based biosensors," *Ultramicroscopy*, vol. 82, no. 1-4, pp. 23-31, 2000.

[29] S. Shahruz, "Design of mechanical band-pass filters with large frequency bands for energy scavenging," *Mechatronics*, vol. 16, no. 9, pp. 523-531, 2006.

[30] S. Shahruz, "Limits of performance of mechanical band-pass filters used in energy scavenging," *Journal of sound and vibration*, vol. 293, no. 1-2, pp. 449-461, 2006.

[31] M. Saadatzi, M. N. Saadatzi, V. Tavaf, and S. Banerjee, "AEVE 3D: Acousto Electrodynamic 3-Dimensional Vibration Exciter for Engineering Testing," *IEEE/ASME Transactions on Mechatronics*, 2018.

[32] V. Tavaf, M. Saadatzi, and S. Banerjee, "Quantification of degraded constitutive coefficients of composites in the presence of distributed defects " *Journal of Composite Materials*, vol. 53, 2018.

[33] S. P. Beeby, M. J. Tudor, and N. White, "Energy harvesting vibration sources for microsystems applications," *Measurement science and technology*, vol. 17, no. 12, p. R175, 2006.

[34] S. R. Anton and H. A. Sodano, "A review of power harvesting using piezoelectric materials (2003–2006)," *Smart materials and Structures*, vol. 16, no. 3, p. R1, 2007.

[35] S. Priya, "Advances in energy harvesting using low profile piezoelectric transducers," *Journal of electroceramics*, vol. 19, no. 1, pp. 167-184, 2007.

[36] K. Cook-Chennault, N. Thambi, and A. Sastry, "Powering MEMS portable devices—a review of non-regenerative and regenerative power supply systems with special emphasis on piezoelectric energy harvesting systems," *Smart Materials and Structures*, vol. 17, no. 4, p. 043001, 2008.

[37] K. A. Cunefare, E. Skow, A. Erturk, J. Savor, N. Verma, and M. Cacan, "Energy harvesting from hydraulic pressure fluctuations," *Smart Materials and Structures*, vol. 22, no. 2, p. 025036, 2013.

[38] S. Moradi and V. Tavaf, "Crack detection in circular cylindrical shells using differential quadrature method," *International Journal of Pressure Vessels and Piping*, vol. 111, pp. 209-216, 2013.

[39] B. Mohammadi, M. Rohanifar, D. Salimi-Majd, and A. Farrokhabadi, "Micromechanical prediction of damage due to transverse ply cracking under fatigue loading in composite laminates," *Journal of Reinforced Plastics and Composites,* vol. 36, no. 5, pp. 377-395, 2017.

[40] H. S. Kim, J.-H. Kim, and J. Kim, "A review of piezoelectric energy harvesting based on vibration," *International journal of precision engineering and manufacturing,* vol. 12, no. 6, pp. 1129-1141, 2011.

[41] R. L. Harne and K. Wang, "A review of the recent research on vibration energy harvesting via bistable systems," *Smart materials and structures,* vol. 22, no. 2, p. 023001, 2013.

[42] R. Harne, M. Thota, and K. Wang, "Bistable energy harvesting enhancement with an auxiliary linear oscillator," *Smart Materials and Structures,* vol. 22, no. 12, p. 125028, 2013.

[43] D. Zhu, M. J. Tudor, and S. P. Beeby, "Strategies for increasing the operating frequency range of vibration energy harvesters: a review," *Measurement Science and Technology,* vol. 21, no. 2, p. 022001, 2009.

[44] S. Saadon and O. Sidek, "A review of vibration-based MEMS piezoelectric energy harvesters," *Energy Conversion and Management,* vol. 52, no. 1, pp. 500-504, 2011.

[45] R. Caliò *et al.*, "Piezoelectric energy harvesting solutions," *Sensors,* vol. 14, no. 3, pp. 4755-4790, 2014.

[46] J. Paulo and P. Gaspar, "Review and future trend of energy harvesting methods for portable medical devices," in *Proceedings of the world congress on engineering*, 2010, vol. 2, pp. 168-196.

[47] L. Mateu and F. Moll, "Review of energy harvesting techniques and applications for microelectronics," in *VLSI Circuits and Systems II*, 2005, vol. 5837, pp. 359-373: International Society for Optics and Photonics.

[48] J. Matiko, N. Grabham, S. Beeby, and M. Tudor, "Review of the application of energy harvesting in buildings," *Measurement Science and Technology,* vol. 25, no. 1, p. 012002, 2013.

[49] Z. Wan, Y. Tan, and C. Yuen, "Review on energy harvesting and energy management for sustainable wireless sensor networks," in *2011 IEEE 13th international conference on communication technology*, 2011, pp. 362-367: IEEE.

[50] Z. Chen, B. Guo, Y. Yang, and C. Cheng, "Metamaterials-based enhanced energy harvesting: A review," *Physica B: Condensed Matter,* vol. 438, pp. 1-8, 2014.

[51] V. Tavaf, M. Saadatzi, S. Shrestha, and S. Banerjee, "Quantification of material degradation and its behavior of elastodynamic Green's function for computational wave field modeling in composites," *Materials Today Communications,* vol. 17, pp. 402-412, 2018.

[52] V. Tavaf, M. Saadatzi, S. Shrestha, and S. Banerjee, "Effect of multiscale precursor damage on wave propagation through modulated constitutive properties of

composite materials," in *Health Monitoring of Structural and Biological Systems XII*, 2018, vol. 10600, p. 106001N: International Society for Optics and Photonics.

[53] M. M. Indaleeb, H. Ahmed, M. Saadatzi, and S. Banerjee, "Dirac-like cone modulation for phononic crystals using deaf band," in *Health Monitoring of Structural and Biological Systems XIII*, 2019, vol. 10972, p. 109721Z: International Society for Optics and Photonics.

[54] M. Khan, P. Sultana, M. Saadatzi, M. Tahiyat, T. Farouk, and S. Banerjee, "Enhancement of piezoelectric properties of nanofibers and nanocomposite membranes through corona treatment," *Bulletin of the American Physical Society*, vol. 64, 2019.

[55] E. I. Administration. (2009). *Use of Energy in the United States Explained*. Available: https://www.eia.gov/energyexplained/index.php?page=us_energy_use

[56] C. Helman. (2013). *How Much Electricity Do Your Gadgets Really Use?* Available: https://www.forbes.com/sites/christopherhelman/2013/09/07/how-much-energy-does-your-iphone-and-other-devices-use-and-what-to-do-about-it/#83c6d742f702

[57] M. Dresselhaus and I. Thomas, "Alternative energy technologies," *Nature*, vol. 414, no. 6861, p. 332, 2001.

[58] N. Panwar, S. Kaushik, and S. Kothari, "Role of renewable energy sources in environmental protection: a review," *Renewable and Sustainable Energy Reviews*, vol. 15, no. 3, pp. 1513-1524, 2011.

[59] R. Ahmed, F. Mir, and S. Banerjee, "A review on energy harvesting approaches for renewable energies from ambient vibrations and acoustic waves using piezoelectricity," *Smart Materials and Structures*, vol. 26, no. 8, p. 085031, 2017.

[60] S. Dongna, P. Jung-Hyun, A. Jyoti, C. Song-Yul, C. W. Howard, III, and K. Dong-Joo, "The design, fabrication and evaluation of a MEMS PZT cantilever with an integrated Si proof mass for vibration energy harvesting," *Journal of Micromechanics and Microengineering*, vol. 18, no. 5, p. 055017, 2008.

[61] S. Rafique and P. Bonello, "Experimental validation of a distributed parameter piezoelectric bimorph cantilever energy harvester," *Smart materials and structures*, vol. 19, no. 9, p. 094008, 2010.

[62] A. Erturk and D. J. Inman, "An experimentally validated bimorph cantilever model for piezoelectric energy harvesting from base excitations," *Smart materials and structures*, vol. 18, no. 2, p. 025009, 2009.

[63] W. Choi, Y. Jeon, J.-H. Jeong, R. Sood, and S.-G. Kim, "Energy harvesting MEMS device based on thin film piezoelectric cantilevers," *Journal of Electroceramics*, vol. 17, no. 2-4, pp. 543-548, 2006.

[64] S. Priya and D. J. Inman, *Energy harvesting technologies*. Springer, 2009.

[65] A. Erturk and D. Inman, "Broadband piezoelectric power generation on high-energy orbits of the bistable Duffing oscillator with electromechanical coupling," *Journal of Sound and Vibration*, vol. 330, no. 10, pp. 2339-2353, 2011.

[66] S. Zhou, J. Cao, D. J. Inman, J. Lin, S. Liu, and Z. Wang, "Broadband tristable energy harvester: modeling and experiment verification," *Applied Energy*, vol. 133, pp. 33-39, 2014.

[67] S. C. Stanton, C. C. McGehee, and B. P. Mann, "Nonlinear dynamics for broadband energy harvesting: Investigation of a bistable piezoelectric inertial generator," *Physica D: Nonlinear Phenomena*, vol. 239, no. 10, pp. 640-653, 2010.

[68] S. Zhou, J. Cao, A. Erturk, and J. Lin, "Enhanced broadband piezoelectric energy harvesting using rotatable magnets," *Applied Physics Letters*, vol. 102, no. 17, p. 173901, 2013.

[69] J. Cao, W. Wang, S. Zhou, D. J. Inman, and J. Lin, "Nonlinear time-varying potential bistable energy harvesting from human motion," *Applied Physics Letters*, vol. 107, no. 14, p. 143904, 2015.

[70] H. Lv, X. Tian, M. Y. Wang, and D. Li, "Vibration energy harvesting using a phononic crystal with point defect states," *Applied Physics Letters*, vol. 102, no. 3, p. 034103, 2013.

[71] Y. Tianchen, Y. Jian, S. Ruigang, and L. Xiaowei, "Vibration energy harvesting system for railroad safety based on running vehicles," *Smart Materials and Structures*, vol. 23, no. 12, p. 125046, 2014.

[72] M. Bahrekazemi, "Train-induced ground vibration and its prediction," Byggvetenskap, 2004.

[73] G. Gatti, M. Brennan, M. Tehrani, and D. Thompson, "Harvesting energy from the vibration of a passing train using a single-degree-of-freedom oscillator," *Mechanical Systems and Signal Processing*, vol. 66, pp. 785-792, 2016.

[74] M. Bryant and E. Garcia, "Modeling and testing of a novel aeroelastic flutter energy harvester," *Journal of vibration and acoustics*, vol. 133, no. 1, p. 011010, 2011.

[75] S. R. Anton and D. J. Inman, "Vibration energy harvesting for unmanned aerial vehicles," in *Active and Passive Smart Structures and Integrated Systems 2008*, 2008, vol. 6928, p. 692824: International Society for Optics and Photonics.

[76] S. Guenneau, A. Movchan, G. Pétursson, and S. A. Ramakrishna, "Acoustic metamaterials for sound focusing and confinement," *New Journal of physics*, vol. 9, no. 11, p. 399, 2007.

[77] C. M. Krowne and Y. Zhang, *Physics of negative refraction and negative index materials*. Springer, 2007.

[78] L. G. Carrascosa, M. Moreno, M. Alvarez, and L. M. Lechuga, "Nanomechanical biosensors: a new sensing tool," *TrAC Trends in Analytical Chemistry*, vol. 25, no. 3, pp. 196-206, 2006.

[79] Q. Zhu, W. Y. Shih, and W.-H. Shih, "Mechanism of flexural resonance frequency shift of a piezoelectric microcantilever sensor during humidity detection," *Applied physics letters*, vol. 92, no. 18, p. 183505, 2008.

[80] M. Hodnett, R. Chow, and B. Zeqiri, "High-frequency acoustic emissions generated by a 20 kHz sonochemical horn processor detected using a novel broadband acoustic sensor: a preliminary study," *Ultrasonics sonochemistry*, vol. 11, no. 6, pp. 441-454, 2004.

[81] L. Watts, D. A. Kerns, R. F. Lyon, and C. A. Mead, "Improved implementation of the silicon cochlea," *IEEE Journal of Solid-state circuits*, vol. 27, no. 5, pp. 692-700, 1992.

[82] R. J. Diependaal and M. A. Viergever, "Nonlinear and active two-dimensional cochlear models: Time-domain solution," *The Journal of the Acoustical Society of America*, vol. 85, no. 2, pp. 803-812, 1989.

[83] P. J. Kolston, M. A. Viergever, E. de Boer, and R. J. Diependaal, "Realistic mechanical tuning in a micromechanical cochlear model," *The Journal of the Acoustical Society of America*, vol. 86, no. 1, pp. 133-140, 1989.

[84] M. M. Sondhi, "Method for computing motion in a two-dimensional cochlear model," *The Journal of the Acoustical Society of America*, vol. 63, no. 5, pp. 1468-1477, 1978.

[85] L.-Y. Wu, L.-W. Chen, and C.-M. Liu, "Experimental investigation of the acoustic pressure in cavity of a two-dimensional sonic crystal," *Physica B: Condensed Matter*, vol. 404, no. 12, pp. 1766-1770, 2009.

[86] L.-Y. Wu, L.-W. Chen, and C.-M. Liu, "Acoustic pressure in cavity of variously sized two-dimensional sonic crystals with various filling fractions," *Physics Letters A*, vol. 373, no. 12, pp. 1189-1195, 2009.

[87] M. Saadatzi, F. Mir, M. N. Saadatzi, and S. Banerjee, "Modeling and Fabrication of a Multi-axial Piezoelectric Energy Harvester based on a Metamaterial-inspired Structure," *IEEE Sensors Journal*, vol. 18, no. 22, pp. 9410-9419, 2018.

[88] M. Saadatzi, M. N. Saadatzi, R. Ahmed, and S. Banerjee, "An electro-dynamic 3-dimensional vibration test bed for engineering testing," in *Industrial and Commercial Applications of Smart Structures Technologies 2017*, 2017, vol. 10166, p. 101660D: International Society for Optics and Photonics.

[89] M. Saadatzi, M. N. Saadatzi, V. Tavaf, and S. Banerjee, "AEVE 3D: Acousto electrodynamic three-dimensional vibration exciter for engineering testing," *IEEE/ASME Transactions on Mechatronics*, vol. 23, no. 4, pp. 1897-1906, 2018.

[90] M. Saadatzi, M. N. Saadatzi, V. Tavaf, and S. Banerjee, "Development of a PVDF Based Artificial Basilar Membrane," in *Bioinspiration, Biomimetics, and Bioreplication VIII*, 2018, vol. 10593, p. 1059318: International Society for Optics and Photonics.

[91] J. Park, B. Park, D. Kim, and J. Park, "Determination of effective mass density and modulus for resonant metamaterials," *The Journal of the Acoustical Society of America*, vol. 132, no. 4, pp. 2793-2799, 2012.

[92] Z. Liu *et al.*, "Locally resonant sonic materials," *Science*, vol. 289, no. 5485, pp. 1734-1736, 2000.

[93] H. Huang, C. Sun, and G. Huang, "On the negative effective mass density in acoustic metamaterials," *International Journal of Engineering Science,* vol. 47, no. 4, pp. 610-617, 2009.

[94] G. Huang and C. Sun, "Band gaps in a multiresonator acoustic metamaterial," *Journal of Vibration and Acoustics,* vol. 132, no. 3, p. 031003, 2010.

[95] M. I. Hussein, "Reduced Bloch mode expansion for periodic media band structure calculations," in *Proceedings of the Royal Society of London A: Mathematical, Physical and Engineering Sciences,* 2009, vol. 465, no. 2109, pp. 2825-2848: The Royal Society.

[96] M. M. Indaleeb, H. Ahmed, M. Saadatzi, and S. Banerjee, "Deaf band-based prediction of Dirac cone in acoustic metamaterials," *Journal of Applied Physics,* vol. 127, no. 6, p. 064903, 2020.

[97] M. SAADATZI, "MEMORY COMPILER FOR VARIABILITY TOLERANCE," 2015.

[98] M. Saadatzi, "Design of Power Efficient 32-Kilobit Memory Compiler for Variability Tolerance," Multimedia University (Malaysia), 2015.

[99] M. N. Saadatzi, J. Poshtan, and M. S. Saadatzi, "Application of MIMO disturbance observer to control of an electric wheelchair using NSGA-II," *Journal of medical signals and sensors,* vol. 1, no. 2, p. 122, 2011.

[100] M. N. Saadatzi, J. Poshtan, M. S. Saadatzi, and F. Tafazzoli, "Novel system identification method and multi-objective-optimal multivariable disturbance observer for electric wheelchair," *ISA transactions,* vol. 52, no. 1, pp. 129-139, 2013.

[101] A. K. Singh, M. Saadatzi, and C. Venkataseshaiah, "Monte–Carlo simulation for 9T SRAM cell in 45 nm CMOS," *Int. J. Adv. Res. Sci. Eng.,* vol. 4, no. 1, 2015.

[102] A. K. Singh, M. Saadatzi, and C. Venkataseshaiah, "Design of a single-ended energy efficient data-dependent-write-assist dynamic (DDWAD) SRAM cell for improved stability and reliability," *Analog Integrated Circuits and Signal Processing,* vol. 90, no. 2, pp. 411-426, 2017.

[103] A. K. Singh, M.-S. Saadatzi, and C. Venkataseshaiah, "Design of Peripheral Circuits for the Implementation of Memory Array Using Data-Aware (DA) SRAM Cell in 65 nm CMOS Technology for Low Power Consumption," *Journal of Low Power Electronics,* vol. 12, no. 1, pp. 9-20, 2016.

[104] H. A. Sodano, D. J. Inman, and G. Park, "Comparison of piezoelectric energy harvesting devices for recharging batteries," *Journal of intelligent material systems and structures,* vol. 16, no. 10, pp. 799-807, 2005.

[105] S. Gonella, A. C. To, and W. K. Liu, "Interplay between phononic bandgaps and piezoelectric microstructures for energy harvesting," *Journal of the Mechanics and Physics of Solids,* vol. 57, no. 3, pp. 621-633, 3// 2009.

[106] M. Saadatzi, M. N. Saadatzi, V. Tavaf, and S. Banerjee, "Finite element analysis of smart structural implications of a beam-type artificial basilar membrane inspired

sensor," in *Bioinspiration, Biomimetics, and Bioreplication IX*, 2019, vol. 10965, p. 109650S: International Society for Optics and Photonics.

[107] M. Saadatzi, M. N. Saadatzi, R. Ahmed, and S. Banerjee, *An electro-dynamic 3-dimensional vibration test bed for engineering testing* (SPIE Smart Structures and Materials + Nondestructive Evaluation and Health Monitoring). SPIE, 2017.

[108] P. DALLOS, "Biophysics of the cochlea," *Handbook of perception,* vol. 4, pp. 125-162, 1978.

[109] E. Evans, "Functional anatomy of the auditory system," *The senses,* pp. 251-306, 1982.

[110] R. G. Kessel and R. H. Kardon, *Tissues and organs: a text-atlas of scanning electron microscopy* (no. C/611.018102 K4). WH Freeman San Francisco, 1979.

[111] R. H. Fitch, S. Miller, and P. Tallal, "Neurobiology of speech perception," *Annual review of neuroscience,* vol. 20, no. 1, pp. 331-353, 1997.

[112] M. Jibu, K. H. Pribram, and K. Yasue, "From conscious experience to memory storage and retrieval: the role of quantum brain dynamics and boson condensation of evanescent photons," *International Journal of Modern Physics B,* vol. 10, no. 13n14, pp. 1735-1754, 1996.

[113] E. Murugasu and I. J. Russell, "The effect of efferent stimulation on basilar membrane displacement in the basal turn of the guinea pig cochlea," *Journal of Neuroscience,* vol. 16, no. 1, pp. 325-332, 1996.

[114] J. D. Cole and R. S. Chadwick, "An approach to mechanics of the cochlea," *Zeitschrift für angewandte Mathematik und Physik ZAMP,* vol. 28, no. 5, pp. 785-804, 1977.

[115] N. P. Cooper and W. S. Rhode, "Basilar membrane mechanics in the hook region of cat and guinea-pig cochleae: sharp tuning and nonlinearity in the absence of baseline position shifts," *Hearing research,* vol. 63, no. 1-2, pp. 163-190, 1992.

[116] A. Recio-Spinoso, Y.-H. Fan, and M. A. Ruggero, "Basilar-membrane responses to broadband noise modeled using linear filters with rational transfer functions," *IEEE Transactions on Biomedical Engineering,* vol. 58, no. 5, pp. 1456-1465, 2011.

[117] J. L. Flanagan, "Models for Approximating Basilar Membrane Displacement—Part II. Effects of Middle-Ear Transmission and Some Relations between Subjective and Physiological Behavior," *Bell System Technical Journal,* vol. 41, no. 3, pp. 959-1009, 1962.

[118] J. L. Flanagan, "Models for approximating basilar membrane displacement," *Bell System Technical Journal,* vol. 39, no. 5, pp. 1163-1191, 1960.

[119] E. D. Schubert, "History of research on hearing," *Handbook of perception,* vol. 4, pp. 41-80, 1978.

[120] T. J. Hamilton, C. Jin, and A. van Schaik, "A basilar membrane resonator for an active 2-D cochlea," in *Circuits and Systems, 2007. ISCAS 2007. IEEE International Symposium on*, 2007, pp. 2387-2390: IEEE.

[121] S. Iurato, "Functional implications of the nature and submicroscopic structure of the tectorial and basilar membranes," *The Journal of the Acoustical Society of America*, vol. 34, no. 9B, pp. 1386-1395, 1962.

[122] G. Von Békésy, "Hearing theories and complex sounds," *The Journal of the Acoustical Society of America*, vol. 35, no. 4, pp. 588-601, 1963.

[123] J. Jang, J. H. Jang, and H. Choi, "MEMS flexible artificial basilar membrane fabricated from piezoelectric aluminum nitride on an SU-8 substrate," *Journal of Micromechanics and Microengineering*, vol. 27, no. 7, p. 075006, 2017.

[124] S. Kim, W. J. Song, J. Jang, J. H. Jang, and H. Choi, "Mechanical frequency selectivity of an artificial basilar membrane using a beam array with narrow supports," *Journal of Micromechanics and Microengineering*, vol. 23, no. 9, p. 095018, 2013.

[125] S. S. Narayan, A. N. Temchin, A. Recio, and M. A. Ruggero, "Frequency tuning of basilar membrane and auditory nerve fibers in the same cochleae," *Science*, vol. 282, no. 5395, pp. 1882-1884, 1998.

[126] A. L. Nuttall and D. F. Dolan, "Steady-state sinusoidal velocity responses of the basilar membrane in guinea pig," *The Journal of the Acoustical Society of America*, vol. 99, no. 3, pp. 1556-1565, 1996.

[127] A. L. Nuttall, D. F. Dolan, and G. Avinash, "Laser Doppler velocimetry of basilar membrane vibration," *Hearing research*, vol. 51, no. 2, pp. 203-213, 1991.

[128] M. A. Ruggero, "Responses to sound of the basilar membrane of the mammalian cochlea," *Current opinion in neurobiology*, vol. 2, no. 4, pp. 449-456, 1992.

[129] M. A. Ruggero and N. C. Rich, "Application of a commercially-manufactured Doppler-shift laser velocimeter to the measurement of basilar-membrane vibration," *Hearing research*, vol. 51, no. 2, pp. 215-230, 1991.

[130] M. A. Ruggero, N. C. Rich, A. Recio, S. S. Narayan, and L. Robles, "Basilar-membrane responses to tones at the base of the chinchilla cochlea," *The Journal of the Acoustical Society of America*, vol. 101, no. 4, pp. 2151-2163, 1997.

[131] M. A. Ruggero, L. Robles, and N. C. Rich, "Two-tone suppression in the basilar membrane of the cochlea: mechanical basis of auditory-nerve rate suppression," *Journal of neurophysiology*, vol. 68, no. 4, pp. 1087-1099, 1992.

[132] M. J. Wittbrodt, C. R. Steele, and S. Puria, "Developing a physical model of the human cochlea using microfabrication methods," *Audiology and Neurotology*, vol. 11, no. 2, pp. 104-112, 2006.

[133] H. Shintaku, T. Kobayashi, K. Zusho, H. Kotera, and S. Kawano, "Wide-range frequency selectivity in an acoustic sensor fabricated using a microbeam array with non-uniform thickness," *Journal of Micromechanics and Microengineering*, vol. 23, no. 11, p. 115014, 2013.

[134] H. Tanujaya, H. Shintaku, D. Kitagawa, A. Adianto, S. Susilodinata, and S. Kawano, "Experimental and analytical study approach of Artificial basilar

membrane prototype (ABMP)," *Journal of Engineering and Technological Sciences*, vol. 45, no. 1, pp. 61-72, 2014.

[135] R. D. White and K. Grosh, "Microengineered hydromechanical cochlear model," *Proceedings of the National Academy of Sciences*, vol. 102, no. 5, pp. 1296-1301, 2005.

[136] J. Jang, S. Kim, D. J. Sly, S. J. O'leary, and H. Choi, "MEMS piezoelectric artificial basilar membrane with passive frequency selectivity for short pulse width signal modulation," *Sensors and Actuators A: Physical*, vol. 203, pp. 6-10, 2013.

[137] E. Ghafoori, M. H. Kargarnovin, and A. R. Ghahremani, "Dynamic responses of a rectangular plate under motion of an oscillator using a semi-analytical method," *Journal of Vibration and Control*, vol. 17, no. 9, pp. 1310-1324, 2011.

[138] K. Mauritsson, P. D. Folkow, and A. Boström, "Dynamic equations for a fully anisotropic elastic plate," *Journal of Sound and Vibration*, vol. 330, no. 11, pp. 2640-2654, 2011.

[139] K. Mauritsson and P. Folkow, "Dynamic equations for a fully anisotropic piezoelectric rectangular plate," *Computers & Structures*, vol. 153, pp. 112-125, 2015.

[140] L. Dovgilovich and I. Sofronov, "High-accuracy finite-difference schemes for solving elastodynamic problems in curvilinear coordinates within multiblock approach," *Applied Numerical Mathematics*, vol. 93, pp. 176-194, 2015.

[141] R. U. Ahmed and S. Banerjee, "A predictive model for biomimetic plate type broadband frequency sensor," in *Bioinspiration, Biomimetics, and Bioreplication 2016*, 2016, vol. 9797, p. 97970T: International Society for Optics and Photonics.

[142] M. R. U. Ahmed, "Bio-Inspired Design of Mechanical Band Pass Sensor with the Ability to Scavenge Energy," 2015.

[143] R. Ahmed and S. Banerjee, "An articulated predictive model for fluid-free artificial basilar membrane as broadband frequency sensor," *Mechanical Systems and Signal Processing*, vol. 100, pp. 766-781, 2018.

[144] I. Szendiuch, B. Psota, A. Otahal, and M. Klapka, "Importance of vibration testing for new technological configurations in electronics," in *Microelectronics Packaging Conference (EMPC), 2013 European*, 2013, pp. 1-5: IEEE.

[145] A. Rastegari, A. Archenti, and M. Mobin, "Condition based maintenance of machine tools: Vibration monitoring of spindle units," in *Reliability and Maintainability Symposium (RAMS), 2017 Annual*, 2017, pp. 1-6: IEEE.

[146] C. H. Yang, D. Song, M. S. Woo, S. K. Hong, K. H. Baek, and T. H. Sung, "Design of vibration exciter by using permanent magnets for application to piezoelectric energy harvesting," in *Applications of Ferroelectrics held jointly with 2012 European Conference on the Applications of Polar Dielectrics and 2012 International Symp Piezoresponse Force Microscopy and Nanoscale Phenomena in Polar Materials (ISAF/ECAPD/PFM), 2012 Intl Symp*, 2012, pp. 1-4: IEEE.

[147] Z. Faming, L. Sheng, and R. Jian, "A new approach to high-frequency electrohydraulic vibration exciter," in *Mechanic Automation and Control Engineering (MACE), 2010 International Conference on*, 2010, pp. 3594-3597: IEEE.

[148] W. Guan, X. Meng, and X. Dong, "Calibration of accelerometer with multicomponent inputs," in *Instrumentation and Measurement Technology Conference (I2MTC) Proceedings, 2014 IEEE International*, 2014, pp. 16-19: IEEE.

[149] J. Bai, J. Ruan, and G. Pan, "Simulation research on the dynamic characteristics of a novel electrohydraulic vibration exciter," in *Mechatronics and Automation, 2009. ICMA 2009. International Conference on*, 2009, pp. 3650-3655: IEEE.

[150] X. Zibin, M. Jianqing, F. Yingguo, B. Jiping, and R. Jian, "Height frequency electro-hydraulic vibration exciter with 2D valve," in *Systems and Control in Aerospace and Astronautics, 2008. ISSCAA 2008. 2nd International Symposium on*, 2008, pp. 1-4: IEEE.

[151] J. Pluta and P. Orkisz, "Bi-axial exciter of mechanical vibrations," in *Carpathian Control Conference (ICCC), 2012 13th International*, 2012, pp. 568-572: IEEE.

[152] Z.-q. Li, X.-p. Mo, Y.-z. Pan, and Y.-p. Liu, "Design and analysis of a longitudinal piezoelectric vibration exciter," in *Piezoelectricity, Acoustic Waves and Device Applications (SPAWDA), 2012 Symposium on*, 2012, pp. 155-158: IEEE.

[153] J. Bai, J. Ruan, and G. Pan, "Simulation research on the dynamic characteristics of a novel electrohydraulic vibration exciter," in *2009 International Conference on Mechatronics and Automation*, 2009, pp. 3650-3655: IEEE.

[154] W. He, C. Wang, M. Yu, R. Shen, and S. Jia, "Closed-double-magnetic circuit for a long-stroke horizontal electromagnetic vibration exciter," *IEEE Transactions on Magnetics*, vol. 49, no. 8, pp. 4865-4872, 2013.

[155] G. Carta, A. B. Movchan, L. P. Argani, and O. S. Bursi, "Quasi-periodicity and multi-scale resonators for the reduction of seismic vibrations in fluid-solid systems," *International Journal of Engineering Science*, vol. 109, pp. 216-239, 2016.

[156] T. Kai and K. Tamaki, "A near-optimal control approach to 3D ball-in-socket joint space robot models with initial angular momenta," *Acta Astronautica*, vol. 68, no. 11, pp. 1702-1711, 2011.

[157] A. Crut, P. Maioli, N. Del Fatti, and F. Vallée, "Time-domain investigation of the acoustic vibrations of metal nanoparticles: size and encapsulation effects," *Ultrasonics*, vol. 56, pp. 98-108, 2015.

[158] D. G. Albert, S. Taherzadeh, K. Attenborough, P. Boulanger, and S. N. Decato, "Ground vibrations produced by surface and near-surface explosions," *Applied Acoustics*, vol. 74, no. 11, pp. 1279-1296, 2013.

[159] J.-H. Kim, J.-H. Kim, S.-H. Jeong, and B.-W. Han, "Design and Experiment of an Electromagnetic Vibration Exciter for the Rapping of an Electrostatic Precipitator," *Journal of Magnetics*, vol. 17, no. 1, pp. 61-67, 2012.

[160] M. Saadatzi, M. N. Saadatzi, and S. Banerjee, "High Voltage Energy Harvesting From Embedded PVDF Harvester Inspired From Metamaterial Design," in *ASME International Mechanical Engineering Congress and Exposition*, 2019, vol. 59438, p. V006T06A015: American Society of Mechanical Engineers.

[161] M. S. Saadatzi, H. Ahmed, M. M. Indaleeb, and S. Banerjee, "RUSH: Realtime ultrasonic scanning using submergible hydraulic robotic arms for mechanical properties testing," in *Smart Structures and NDE for Energy Systems and Industry 4.0*, 2019, vol. 10973, p. 109730X: International Society for Optics and Photonics.

[162] K. Ziming, W. Xiuye, W. Juan, and Z. Huixian, "Analysis of fluid-structure interaction vibration response for vibration system excited by wave exciter," in *Signal Processing Systems (ICSPS), 2010 2nd International Conference on*, 2010, vol. 1, pp. V1-624-V1-628: IEEE.

[163] W. Jia and J. Ruan, "Four-axis high-frequcncy structural strength fatigue test system," in *Control, Automation, Robotics and Vision, 2008. ICARCV 2008. 10th International Conference on*, 2008, pp. 1577-1582: IEEE.

[164] S. Li, Z. Peng, A. Zhang, D. Luo, and F. Wang, "Dual resonant structure for energy harvesting from random vibration sources," in *Nano/Micro Engineered and Molecular Systems (NEMS), 2016 IEEE 11th Annual International Conference on*, 2016, pp. 255-259: IEEE.

[165] S. Ju, S. H. Chae, Y. Choi, S. Lee, H. W. Lee, and C.-H. Ji, "A low frequency vibration energy harvester using magnetoelectric laminate composite," *Smart Materials and Structures*, vol. 22, no. 11, p. 115037, 2013.

[166] V. Tavaf, M. Saadatzi, and S. Banerjee, "Effect of void sizes on effective material properties of unidirectional composite materials," in *Health Monitoring of Structural and Biological Systems XIII*, 2019, vol. 10972, p. 109722K: International Society for Optics and Photonics.

[167] V. Tavaf, M. Saadatzi, and S. Banerjee, "Quantification of degraded constitutive coefficients of composites in the presence of distributed defects," *Journal of Composite Materials*, vol. 53, no. 18, pp. 2517-2529, 2019.

[168] B. Koohbor, M. Rohanifar, and A. Kidane, "Characterizing fracture response of cracked transversely graded materials," *Composite Structures*, vol. 229, p. 111439, 2019.

[169] G. C. McLaskey and S. D. Glaser, "Acoustic emission sensor calibration for absolute source measurements," *Journal of Nondestructive Evaluation*, vol. 31, no. 2, pp. 157-168, 2012.

[170] Q. Li, Q. Zhang, M. Zhao, and L. Shi, "Study on Calibration of Transfer Character of Ultrasonic Transducer," in *Communication Systems and Information Technology*: Springer, 2011, pp. 251-258.

[171] R. Yan, X. Li, Z. Chen, Q. Xu, and X. Chen, "Improving calibration accuracy of a vibration sensor through a closed loop measurement system," *IEEE Instrumentation & Measurement Magazine,* vol. 19, no. 1, pp. 42-46, 2016.

[172] E. Coffey, "Acoustic resonance testing," in *Future of Instrumentation International Workshop (FIIW), 2012*, 2012, pp. 1-2: IEEE.

[173] J.-J. Zhou, Y.-s. Wang, X. Wang, A.-h. Meng, and Y.-l. Pan, "Design of a flat-panel loudspeaker with giant magnetostrictive exciters," in *Piezoelectricity, Acoustic Waves, and Device Applications, 2008. SPAWDA 2008. Symposium on*, 2008, pp. 528-532: IEEE.

[174] S. Mohanty, K. K. Gupta, and K. S. Raju, "Multi-channel vibro-acoustic fault analysis of ball bearing using wavelet based multi-scale principal component analysis," in *Communications (NCC), 2015 Twenty First National Conference on*, 2015, pp. 1-6: IEEE.

[175] Z. Jun, L. Xin-cheng, T. Jian-hua, Z. Rui-jia, and J. Jing-mei, "Study on vibration energy regeneration of electric vehicle shock absorber," in *Transportation Electrification Asia-Pacific (ITEC Asia-Pacific), 2014 IEEE Conference and Expo*, 2014, pp. 1-5: IEEE.

[176] Y. Chen, Y.-S. Lee, and Y.-C. Lin, "Comparison among individual thermal cycling, vibration test and the combined test for the life estimation of electronic components," in *Microsystems, Packaging, Assembly and Circuits Technology Conference (IMPACT), 2011 6th International*, 2011, pp. 385-388: IEEE.

[177] M. A. Halim, S. Khym, and J. Park, "Frequency up-converted wide bandwidth piezoelectric energy harvester using mechanical impact," *Journal of Applied Physics,* vol. 114, no. 4, p. 044902, 2013.

[178] M. N. Uddin, M. S. Islam, J. Sampe, S. H. M. Ali, and M. Bhuyan, "Design and simulation of piezoelectric cantilever beam based on mechanical vibration for energy harvesting application," in *Innovations in Science, Engineering and Technology (ICISET), International Conference on*, 2016, pp. 1-4: IEEE.

[179] J. Metrology, "Evaluation of measurement data—Guide to the ex pression of uncertainty in measurement," *Bureau International des Poids et Mesures,* 2008.

[180] T. M. Adams, "G104-A2LA Guide for estimation of measurement uncertainty in testing," *American Association of Laboratory Accreditation Manual,* pp. 10-18, 2002.